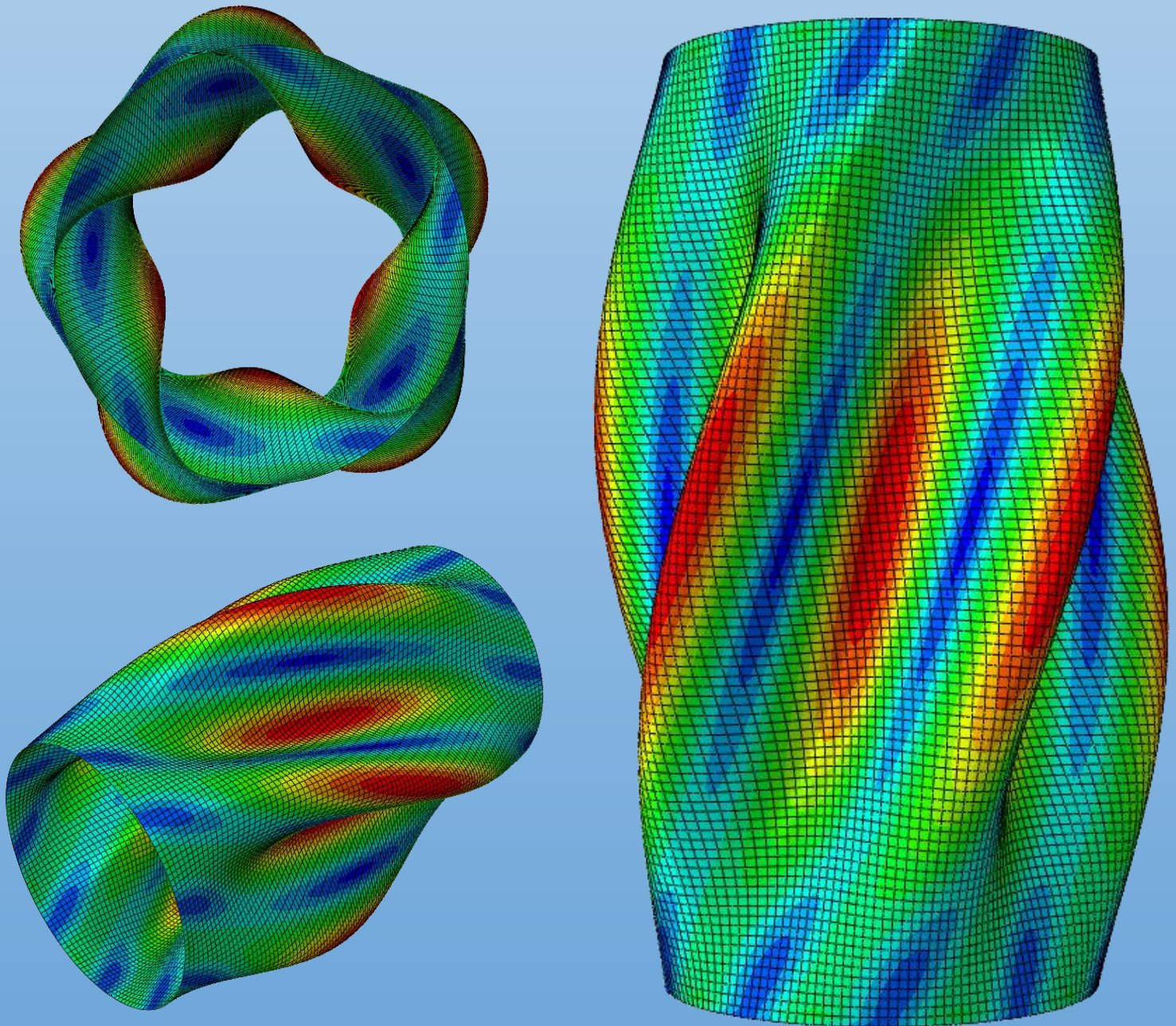


Buckling of Steel Shell Structures

Master Thesis



4th Semester M.Sc. - Structural and Civil Engineering

Kasper Knudsen & Mads Thorup

Aalborg University

08/06-2016



AALBORG UNIVERSITY
STUDENT REPORT

School of Engineering and Science
Department of Civil Engineering

Fibigerstræde 10

9000, Aalborg

Telephone: 99 40 84 84

Fax: 99 40 85 52

<http://www.byggeri.aau.dk>

Title: Buckling of Steel Shell Structures

Projectperiod: M.Sc., 4th semester Spring 2016

Participants:

Mads Thorup

Kasper Knudsen

Supervisor:

Lars Vabbersgaard Andersen

Circulation: 4

Number of pages: 89

Number of pages in appendices: 30

Closed the: 08/06-2016

Synopsis:

This thesis deals with shell structures in shape of a cylinder and an arch. First a cylindrical shell is examined analytically and numerically to see how the shell behaves under meridional- and circumferential compression and torsion. Afterwards imperfections are implemented by using an eigenmode as initial geometry to see how this affects the buckling stress. It is seen that the imperfection reduces the buckling stress as expected and the larger the scaling factor of the eigenmode is the lower is the buckling stress.

Afterwards, a study of shells in the shape of an arch is analysed in order to determine the optimal geometry when considering buckling and yielding. Here a circular, parabolic and catenary cross sectional geometry is analysed when exposed to an inside suction, self weight and line load on top of the arc. The results shows that the different shapes have a large influence on the buckling stress. It is also concluded that the support type is of importance since they might increase or decrease the stresses. Finally, imperfections are implemented in the arch and the results show that the different types of imperfection have different influence on the buckling stress.



Preface

The present master thesis is composed by Kasper Knudsen and Mads Thorup who are students from the fourth semester of the Masters Program in Structural and Civil Engineering at Aalborg University. The thesis is framed in the spring of 2016 with the title "Buckling of Steel Shell Structures".

Reading Guide

The thesis consist of an analysis of a cylindrical shell and a shell in shape of an arch. All appendices are enclosed in a separate appendix report with a matching appendix CD. The thesis is likewise enclosed as a pdf file on the Appendix CD.

All the source references in the thesis are listed as the Harvard-method whereby the text refers to [Surname, Year]. Books are stated with author, title, edition, and publisher whereas web addresses are stated with author, title and date.

Figures and tables are numbered with reference to the chapter and explanatory text is shown below the figures or above the tables. The thesis uses numbered equations and the numbering appears in parenthesis and is placed in the right side of the document. The numbering of the equations is likewise by chapter. Calculations enclosed electronically on the appendix CD are referred to as "Appendix CD" followed by the name of the file, e.g. Appendix CD *file name*. If the file is enclosed in a folder on the Appendix CD it is referred to as Appendix CD *Folder/file name*.



Contents

1	Introduction	1
1.1	Circular Cylindrical Shells	2
1.2	Shell in Arches and Domes	3
1.3	Buckling	6
1.4	Thesis Statement	13
2	Finite Element Method	15
2.1	Finite Element Formulation	16
2.2	Abaqus Model	19
3	Circular Cylinder	25
3.1	Properties of the Cylindrical Shell	25
3.2	Circular Cylinder with Meridional Compression	26
3.3	Circular Cylinder with Circumferential Compression	28
3.4	Circular Cylinder with Shear Stress	28
3.5	Circular Cylinder with Combined Loads	29
3.6	Parameter Study	31
3.7	Numerical Results	38
3.8	Combination of Loads	39
4	Imperfection in Cylindrical Shells	43
4.1	LBA	43
4.2	GNA and GNIA	45
5	Arch Structure	53
5.1	Models	53
5.2	Finite Element Model	55
5.3	Results for Linear Static Analysis	59
5.4	Results for Buckling Analysis	63
6	Imperfections in the Arch	75
6.1	Imperfections in the Loads	75
6.2	Changed Thickness	77
6.3	Dimple and Perturbation Loads	78
7	Conclusion	85
8	Discussion	87

A	Appendix Overview	3
B	Circular Cylinder	5
B.1	Circular Cylinder with Meridional Compression	6
B.2	Circular Cylinder with Circumferential Compression	9
B.3	Circular Cylinder with Shear Stress	11
B.4	Circular Cylinder with Combined Loads	12
C	Euler Load	13
C.1	Analytical	13
C.2	Finite Element Method	15
D	Buckling Modes for LBA	17
D.1	Buckling Modes for Meridional Compression.	17
D.2	Buckling Modes for Circumferential Compression.	19
D.3	Buckling Modes for Shear Stress.	20
E	Arch Structure	23
E.1	Convergence Analysis - Buckling	23
E.2	Convergence Analysis - Linear Static Analysis	24
F	Moment Distribution for all Geometries and Loads	27
G	Arc Length of Parabolic	29

Introduction

For many different civil engineering structures shells are used. Silos, oil pipelines, roofs, wind turbine towers and offshore foundations etc. are all examples of shell structures. A shell is characterized by its geometry and is a three-dimensional structure, whereas one dimension i.e. the thickness is very small compared to its length and width. Some of the advantages of using shell structures are that material consumption is less than other alternatives, and larger areas can be covered without the use of columns if the shell is used as a roof. Although, a disadvantage is that the formwork is costly and analysis can be complicated. Examples in the use of shell structures are seen in Figure 1.1 where silos are constructed of cylindrical shells and Figure 1.2 where the opera house in Sydney is constructed of several shells to give its characteristic design.



Figure 1.1: Silos made by shells [Thebimhub, 2016].



Figure 1.2: Opera house in Sydney made by shells [Digipraim, 2015].

One of the advantages of shell structures is that the thickness is small compared to the other dimensions. The reason that this thickness is sufficient in shell structures when regarding the capacity of the structure is when the geometry is optimal compared to the applied load. If the geometry is not optimal compared to the applied load then thicker shells have to be used.

In a plate only shear and bending forces are present and in a disc only membrane forces are present. A shell is simply a plate that is bended by some curvature and for a shell element bending and membrane forces are both present and the forces are both in and out of plane. For thin plates the stress distribution across the thickness of the plate is assumed

constant and is considered as a plane stress scenario. Furthermore, the transverse shear deformation is neglected in thin plates. Contrary to this the transverse shear deformation should be accounted for in a thick plate since it affects the bending behaviour, but not the in-plane behaviour.

Dependent on what the silo is used for it is exposed to different loads which influence the buckling and therefore the applied load is essential for a cylindrical shell. Throughout history this phenomenon has been well known and by taking advantage of that many types of structures can be build to effectively withstand certain types of loading some of these are described in the following section.

1.1 Circular Cylindrical Shells

Structures with a circular cross section is the optimal cross section to enclose the largest area and thus many structures are designed with this cross section to make the best use of the material. Therefore, spherical structures are the optimal design of a structure to contain the most volume by using the least amount of material but spherical structures are in many cases an unpractical design. A structure which is more frequently used in designs is a cylindrical shell structure. This has the advantage of being a practical design and having a circular cross section. Examples of these types of shell structures are illustrated in Figures 1.3 and 1.4. The tower of the wind turbines and the three cans are similar when considering how they are distributing the stresses when exposed to different loads. If it is assumed that the three cans are empty then the main difference between the structures is the material used to design these types of structures because it is expected they are deforming the same way when exposed to certain types of loads. The cylindrical shell structures are very interesting to study because they are so widely used and both the windturbine and the can needs to be designed as efficiently as possible i.e. they need to have the greatest amount of volume with the least amount of material used and still be a practical design. The purpose for the tower of the wind turbine is to get the highest altitude of the rotor blades since the wind speed increases with height above the surface, thus a small cross section compared to its length is the optimal design. Instead of the cylindrical can the cans could be designed as spheres and thus they would be more efficiently designed to get a larger volume with the least amount of material used but when the spherical cans standing next to each other they are wasting a lot of space and they would become unpractical when drinking from the can, thus it is a worse solution than the cylindrical cans. The cans could also be designed to be squares in order to minimize the loss of space completely when standing next to each other but this design is not the best use of material.



Figure 1.3: Wind turbines [Positronic, 2016].



Figure 1.4: Aluminium cans with different dimensions [Beverage, 2016].

Cylindrical shell structures can be exposed to many different load types. One very typical load case for a shell structure is the inside suction and this load case can be caused in several ways. One way is if a pressure canister, which is illustrated in Figure 1.5, is being emptied all at once in a very short period of time. This will create a vacuum because the pressure inside the canister is lower than the pressure outside. This phenomenon can happen in all kinds of shell structures which are used as a storage facility.



Figure 1.5: Pressure canister [Frederiksen Scientific, 2016].

1.2 Shell in Arches and Domes

A geometry different from the circular cylinder where shells are commonly used is in arches and domes. Even though the circular geometry is the shape which enclose the largest area by the use of the least perimeter it has not been used exclusively in constructions. For

a circular arch the construction needs to be made with the points towards the center as shown in Figure 1.7.

When constructing an arch it is only stable as a whole but under the construction phase it can not support itself. Therefore, it needs support during construction cf. Figure 1.6 [Schillerinstitute, 2013].



Figure 1.6: Circular arch with support during construction [Schillerinstitute, 2013].

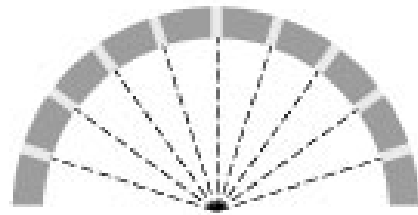


Figure 1.7: Circular arch with points towards the center [Schillerinstitute, 2003].

The reason for not using the circular geometry exclusively is due to the fact that the optimal geometry depends on the applied load as mentioned earlier and therefore, different geometries are to be considered. These different shapes are used in many structures dependent on the load conditions and therefore the load on the shell is essential for choosing one geometry over another. If a chain is hanging between two points the chain will due to gravitation make a shape which is defined as a catenary cf. Figure 1.8 [Schillerinstitute, 2013]. By inverting the shape of the catenary it can be used to create an arc shape that is created by physics and which can support itself [Schillerinstitute, 2013].



Figure 1.8: Chain hanging between two points creating the shape of a catenary [Schillerinstitute, 2003].

This inverse catenary shape is used in many arch shaped constructions throughout history. A few examples are the Florentine Dome in Italy from 1436 and the Taq-i Kisra Palace in

Iraq from 531 A.D. cf. Figures 1.9 and 1.10, respectively.



Figure 1.9: Florentine Dome, Italy [Jaime Alonso, 2014].



Figure 1.10: Taq-i Kisra Palace, Iraq [Schillerinstitute, 2013].

Therefore, the catenary arch is expected to be the optimal geometry when the arch is only exposed to its self weight. If the arch instead is exposed to an inside suction a circular arch is expected to be better than other geometries since it has the same tangential slope everywhere. Furthermore, the circular geometry is able to compress or expand and still have the same tangential slope everywhere on the arch. Another possible load scenario is when a load is acting on top of the arch along its length. For this load scenario two straight elements which are free to rotate in the top joint is expected to be the optimal geometry since it transfers the applied load directly into the two elements cf. Figure 1.11. Since these are straight elements this geometry is not considered. Instead a parabolic geometry is analysed since it has a curved geometry that is steeper than both the circular and catenary geometries cf. Figure 1.12.

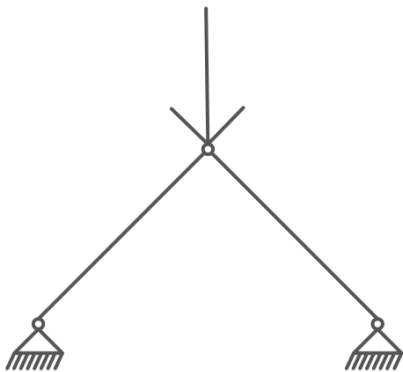


Figure 1.11: Straight elements free to rotate in the joint and with line load on top.

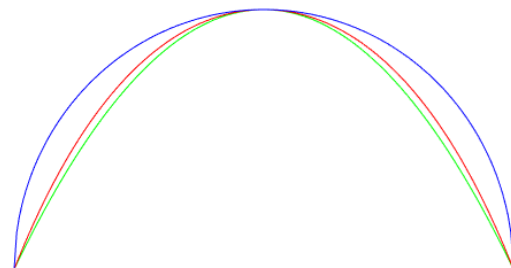


Figure 1.12: Different cross sections for the shell. Blue: circular, red: catenary, green: parabolic.

1.3 Buckling

For structures built with columns and beams the yielding stress is often the controlling failure criteria but the critical buckling stress has to be investigated as well since buckling for a simple supported beam can occur cf. Figure 1.13. For structures made with shells buckling is often critical as seen in Figure 1.14 since buckling creates large deformations without a large increase in the applied load. In the figure some of the shells in the silo have buckled which is critical for the overall structure. A possible explanation for the buckling seen in the figure can be when the silo is emptied too fast which creates a vacuum inside which can lead to buckling. There is multiply ways a shell structure can buckle thus it can undergo different buckling modes as seen in Figure 1.15. The buckling modes are among other things dependent on the applied load and the imperfections in the structure. Similar modes are analysed further later in the report.

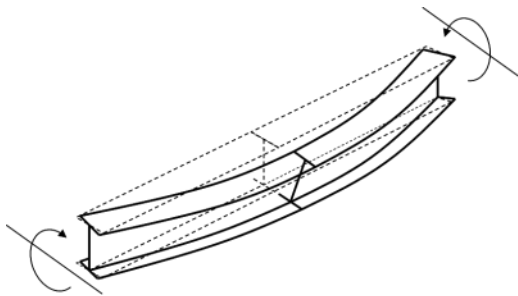


Figure 1.13: Buckling of a simple supported beam [SteelConstruction, 2010].



Figure 1.14: Buckling of shell structure [UCC, 2010].



Figure 1.15: Buckling modes of a cylindrical shell [K. A. Seffen, 2010].

Since buckling often is the critical failure criteria for shell structures the focus in this thesis is on the buckling limit state. The membrane stiffness is much greater than the bending stiffness, and a shell structure can absorb a lot of membrane strain without deforming too much. If the membrane strain energy is equivalent to the amount of bending strain energy, it deforms much more, and in most cases it will buckle before that. The buckling phenomenon is when the shell structure is suddenly failing dramatically in order to exchange the membrane energy into the bending energy. The way the shell structure is buckling and how dramatically it is buckling is dependent on the geometry, material properties and type of loading. Each shell structure is built to withstand the loads acting on it and like any other structure every shell structure is unique. [Bushnell, 1981]

There are two types of buckling which are limit load buckling and bifurcation buckling. Limit load buckling which consist of snap-through buckling and finite disturbance buckling which is illustrated on Figure 1.16.

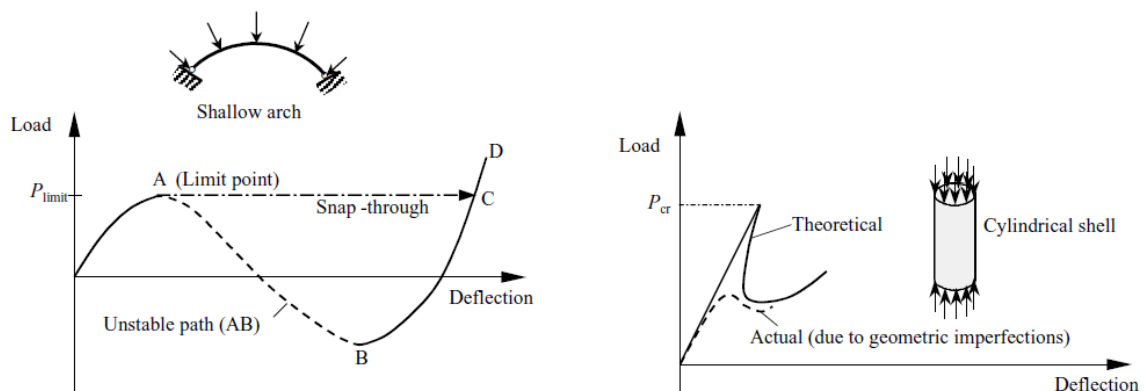


Figure 1.16: Snap-through buckling to the left. Finite disturbance buckling to the right [C. M. Wang, 2005].

The snap-through can be observed for structures as arches and spherical caps. If it is stable the structure will follow the equilibrium path for further loading, but if it is unstable it will undergo a snap-through buckling where it jumps from one equilibrium state to another. For cylindrical shells a finite disturbance buckling can be observed. Limit load buckling occurs at the limit load for the structure with only a single mode of deflection.

In the bifurcation buckling the deflection of the structure will change from one direction to another, that could be going from axial shortening to lateral deflection. The point where the bifurcation occurs is called the critical buckling load, which is illustrated on Figure 1.17.

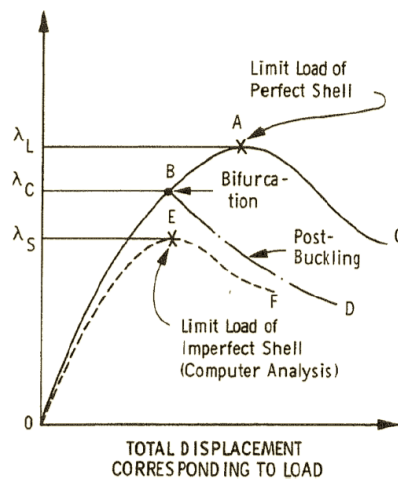


Figure 1.17: Bifurcation buckling on shell structure [C. M. Wang, 2005].

Prior to this point the deflection path is called the primary path and after the bifurcation the path is called post buckling path. The difference between a perfect and an imperfect shell is also observed. For the perfect shell the collapse load is greater, but it also has a dramatical buckling if the collapse load is exceeded whereas the imperfect structure has a lower collapse load, but the buckling is not as dramatical [C. M. Wang, 2005]. There are three main factors regarding imperfections on a shell structure which buckling depends on. The three factors are:

- Loads
- Material properties
- Geometry

1.3.1 Loads

The load scenarios which are later analysed for the shell structures are meridional compression, circumferential compression, shear stress, line load and self weight but they may also be exposed to other types of loads. This may be bending, eccentric loading, a non-uniform load combination or dynamic loading. The loads the cylindrical shell structure is exposed to are illustrated in Figure 1.18 and the loads the arch is exposed to are shown in Figure 1.19 for a circular arch. The loads acting on the cylindrical cylinder only give membrane forces in the structure whereas the loads acting on the arch gives bending forces as well.

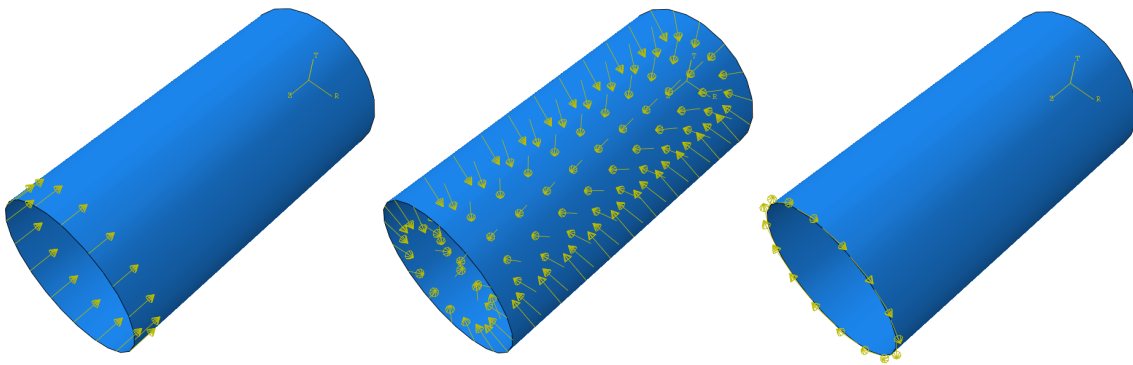


Figure 1.18: Cylindrical shell structure exposed by meridional compression, circumferential compression and shear stress, respectively.

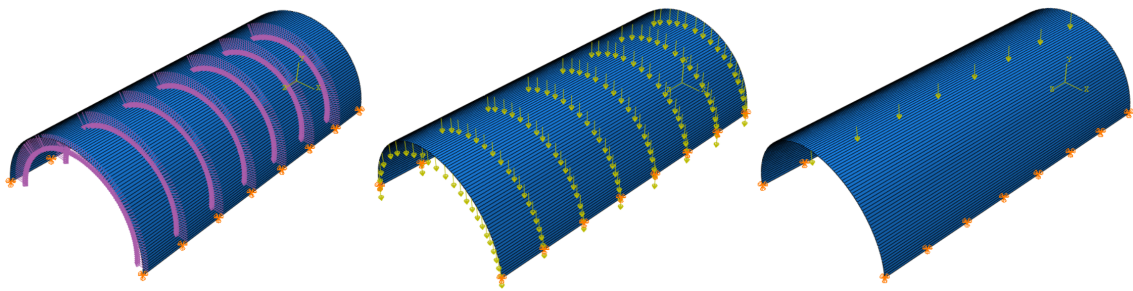


Figure 1.19: Arch structure with inside suction, self weight and line load, respectively.

1.3.2 Material Properties

In modern time many shell structures are not only made of homogeneous materials but can also be made of inhomogeneous composite materials. The composite materials may behave different from a homogeneous material such as steel or aluminium. It has been analysed how a glass-fiber-reinforced plastic cylinder can be modelled for buckling and the conclusion is that it is possible to model composite material which almost fits with the experimental tests [Holst, 2005]. The loading of the cylinder is important for the buckling pattern for

both homogeneous materials and composite material thus the effects of different loads have been analysed [Holst, 2005]. In this thesis only homogeneous materials are considered.

If the shell structure is very resistant towards buckling it yields before buckling occurs. If non-linear material properties are included in the analysis the material is yielding when the yield strength is reached and thus the structure deforms. Consequently, the deformed structure could now be less resistant towards buckling.

1.3.3 Geometry

From recent work on how geometric imperfections are modelled there are four different methods to analyse the models [Castro, 2013]. These are used to model geometric imperfections and determine knockdown factors. The knockdown factor is the ratio of experimentally determined buckling loads to theoretical buckling loads of the geometrically perfect shell structure. The four methods are:

- Linear buckling mode-shaped imperfection (LBMI)
- Single perturbation load imperfection (SPLI)
- Multiple perturbation loads imperfection (MPLI)
- Geometrical dimple imperfection (GDI)

The idea of implementing LBMI is to calculate the eigenmodes in a linear buckling analysis (LBA) when using a eigenmode as initial geometry. The scaling factor in this method is the amplitude of the imperfection. SPLI leads to a local displacement at a given position of the cylinder. It could also be more than one perturbation load in that case it is called multiple perturbation loads imperfection (MPLI). A case of MPLI on a parabolic shell structure is illustrated in Figures 1.20 and 1.21. These figures only shows the initial state but by calculating a model with MPLI as the initial state the effect of the imperfections is obtained.

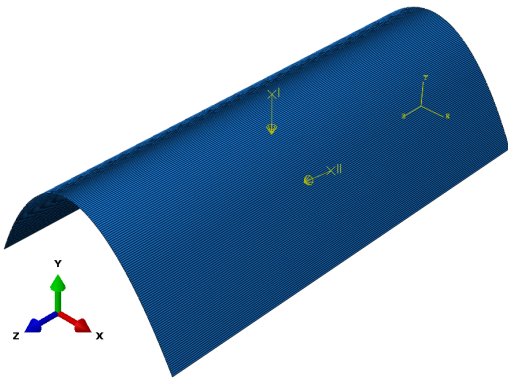


Figure 1.20: Parabolic shell structure exposed by two perturbation loads.

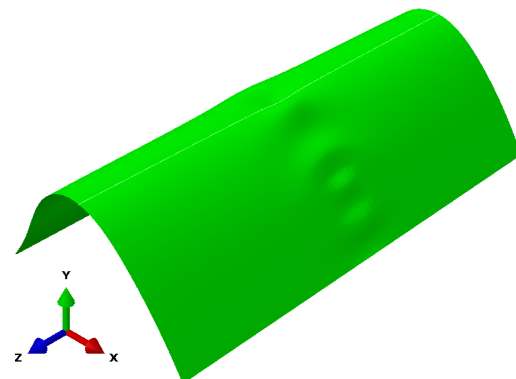


Figure 1.21: Initial state for parabolic shell structure.

Castro [2013] states that the simple SPLI method gives the lowest knockdown factors i.e. the largest buckling stress and is preferred by the authors. Geometrical dimple imperfection (GDI) is similar to the perturbation loads but instead of an implemented load which cause the imperfection, an already geometrical imperfection i.e. a dimple is implemented. A GDI is illustrated in Figure 1.22.

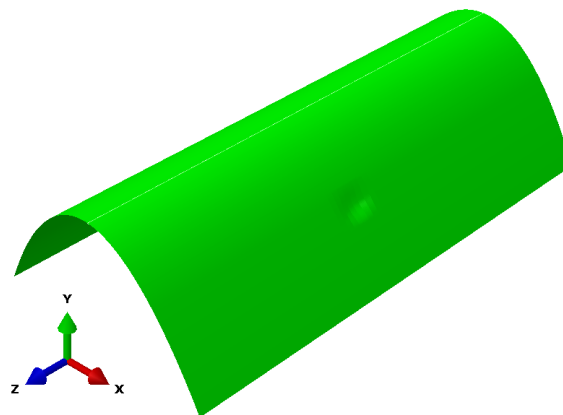


Figure 1.22: Parabolic shell structure with inward dimple.

According to Castro [2013] a dimple imperfection is more realistic compared to any other type of imperfections. There are three methods to analyse the behaviour of the imperfections in the shell structure which are:

- Realistic geometric imperfections
- Stimulating geometric imperfections
- Worst geometric imperfections

Realistic Geometric Imperfections

To model realistic geometric imperfections the geometry is scanned for each model and thus implemented in a FE model. This is the most realistic thinkable approach i.e. to simulate the real imperfect shell structure. This proves to have significant similarities between the buckling modes and the real buckling deformation. Unfortunately, it is not feasible for a civil engineering shell structure because in most cases the actual imperfect shape is not known at the design stage.

Stimulating Geometric Imperfections

Stimulating geometric imperfections requires extensive parametric studies where a great number of fully non-linear shell analyses have to be performed. It is wise to choose as simple equivalent geometric imperfection pattern as possible. The geometric imperfections are simulated by starting from the failure mode of the perfect shell. The pattern of this analysis reveals the weak points of the structure and the idea is to create an initial deformation at these points. Existing experimental data bases can be used to calibrate the amplitudes of the stimulating imperfections before simulating new load scenarios.

Worst Geometric Imperfections.

The worst possible geometric imperfection pattern for a given shell structure is implemented into the non-linear analysis. The eigenmodes from the linear analyses of the shell structure is used to implement the initial state of the analyses with imperfection included where new eigenmodes are obtained. The basic idea of the worst geometric imperfections is to implement a geometric imperfection that gives the lowest critical buckling stress.

The worst geometric imperfection method is often used to analyse the behaviour of the imperfections on the shell structure because the realistic method is in most cases unavailable and the stimulating method requires experimental data for the specific shell structure with the specific load scenario which may not even exist and therefore this method is used in this thesis as well.

1.4 Thesis Statement

The main thesis statement is:

How does the buckling stress of a circular cylindrical shell and a shell in shape of an arch depend on the geometry, material properties, cross section, load and support type with and without imperfections taken into account?

In order to study the above thesis statement the following objects are studied. First, a study of cylindrical shells undergoing meridional compression, circumferential compression and shear stress is analysed using EN-3 [2004]. Afterwards, the buckling stress for the same cylindrical shells are calculated using the finite element method in the software Abaqus. This way the results from Abaqus are verified with the results from EN-3 [2004]. Hereafter, the influence of imperfections in the cylindrical shell is studied by introducing an imperfect cylindrical geometry.

Secondly, shell structures in shape of an arch are examined numerically by varying it between a circular, parabolic and catenary shape with an inside suction, a self weight of the shell and a point load acting on top of the cross section. Afterwards, the influence of imperfections in the shell is examined numerically by implementing a varying load orientation and a geometrical imperfection.

Finite Element Method

The finite element method (FEM) is a computational technique which is used to obtain an approximate solution of boundary value problems. The boundary value problems are also called field problems. The point of interest is the field problems, and these often represent a physical structure. The field problems are described by a discretization of the differential equations which is in the element method. The individual finite elements are small elements of a structure and the elements can vary in size but are not infinitesimal elements. The elements give an estimate of the stresses and strains that the complete structure is experiencing. Dependent on the complexity of the structure, and the amount of finite elements and type of each element, the approximate solutions from FEM varies. For a structure with a simple geometry and a sufficient amount of elements the results can be very close to the exact solution. The mesh elements are connected at points called nodes. All of the connected elements in a structure are called the mesh and it can either be a fine mesh or a crude mesh which depend on the size of the finite elements. The system of equations are solved for the unknowns which is either stresses or displacements. FEM has the advantages that it has no geometric restrictions and the structure or region may have any shape. There are no restrictions of the boundaries and loading conditions. The material properties can change from one region to another or even from one element to another. If the results seem too unreliable or they deviate too much from what they should be, the mesh grading can be upgraded to a finer mesh and thus coming closer to the exact solution. By creating a mesh-grading field that is too fine may result in unnecessary computational power and therefore a convergence analysis is made. To construct the 3D models, the commercial software Abaqus is chosen, which creates the 3D model with FE modelling. In order to understand how the finite element calculations are performed the general formulations are described in the following section.

2.1 Finite Element Formulation

In this section the finite element formulations are given. The general finite element formulation is given by: [Robert D. Cook, 2002]

$$[K]\{D\} = \{R\} \quad (2.1)$$

$[K]$		Global stiffness matrix
$\{D\}$		Displacement
$\{R\}$		External load

In a finite element analysis of linear bifurcation buckling the structure is loaded by an external load of arbitrarily reference level, $\{R\}_{\text{ref}}$, in which a standard linear analysis is performed. From the standard linear analysis the membrane stresses in the shell are determined. From the stresses which are associated with the reference level of external load the corresponding stiffness matrix is $[K_{\sigma}]_{\text{ref}}$. For some other arbitrarily load level which is a scalar, λ , of the reference load then the stiffness matrix is given by: [Robert D. Cook, 2002]

$$[K_{\sigma}] = \lambda[K_{\sigma}]_{\text{ref}} \quad \text{when} \quad \{R\} = \lambda\{R\}_{\text{ref}} \quad (2.2)$$

$[K_{\sigma}]$		Stress stiffness matrix
λ		Scalar multiplier
$[K_{\sigma}]_{\text{ref}}$		Reference stress stiffness matrix
$\{R\}$		External load
$\{R\}_{\text{ref}}$		Reference external load

It is noticed that K_{σ} is a matrix that is a function of an elements geometry, state of membrane stress and displacement field. Furthermore, it is independent of material properties and makes it applicable for anisotropic materials and yielding. Equation (2.2) imply that the stress distribution does not alter for different load levels which means that the conventional stiffness matrix $[K]$ is unchanged when loaded. At the bifurcation point buckling occurs without a change in the external load and therefore: [Robert D. Cook, 2002]

$$([K] + \lambda_{\text{cr}}[K_{\sigma}]_{\text{ref}})\{D\}_{\text{ref}} = \lambda_{\text{cr}}\{R\}_{\text{ref}} \quad (2.3)$$

λ_{cr}		Critical multiplier
$\{D\}_{\text{ref}}$		Reference displacement

If buckling displacement takes place relative to the reference displacement then Equation (2.3) yields:

$$([K] + \lambda_{cr}[K_{\sigma}]_{\text{ref}}) \{D_{\text{ref}} + \delta D\} = \lambda_{cr} \{R\}_{\text{ref}} \quad (2.4)$$

Substituting Equation (2.3) from Equation (2.4) yields:

$$([K] + \lambda_{cr}[K_{\sigma}]_{\text{ref}}) \{\delta D\} = 0 \quad (2.5)$$

Equation (2.5) is an eigenvalueproblem where λ_{cr} is the roots and the smallest root defines the smallest level of external load at which bifurcation occurs. This can be written by: [Robert D. Cook, 2002]

$$\{R\}_{\text{cr}} = \lambda_{cr} \{R\}_{\text{ref}} \quad (2.6)$$

The eigenvector is given by $\{\delta D\}$ and defines the buckling mode associated with the corresponding root, λ_{cr} .

A shell element has similarities to the plate element and the disc element since membrane forces as well as bending and shear can be present. The stress stiffness matrix for a plate is given by: [Robert D. Cook, 2002]

$$[K_{\sigma}] = \int_{-1}^1 \int_{-1}^1 [G_I]^T [J]^{-T} \begin{bmatrix} N_x & N_{xy} \\ N_{xy} & N_y \end{bmatrix} [J]^{-1} [G_I] J d\xi d\eta \quad (2.7)$$

$[G_I]$	Derivatives of shape functions with respect to ξ and η
$[J]$	Jacobian matrix
J	Determinant of the Jacobian matrix
N_x, N_y, N_{xy}	Membrane forces, cf. Figure 2.1

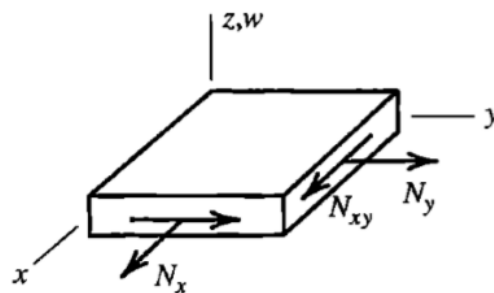


Figure 2.1: Membrane forces on a flat plate [Robert D. Cook, 2002].

The $[G_I]$ matrix relates the derivatives of the lateral displacement, w , and the nodal d.o.f., $\{d\}$: [Robert D. Cook, 2002]

$$\begin{Bmatrix} w,\xi \\ w,\eta \end{Bmatrix} = [G_I]\{d\} \quad (2.8)$$

The inverse Jacobian matrix relates the derivatives in the (x,y)-coordinate system and the derivatives in the (ξ,η) -coordinate system: [Robert D. Cook, 2002]

$$\begin{Bmatrix} w,x \\ w,y \end{Bmatrix} = [J]^{-1} \begin{Bmatrix} w,\xi \\ w,\eta \end{Bmatrix} \quad (2.9)$$

The determinant of the Jacobian matrix relates the small element in the (x,y)-coordinate system and the element in the (ξ,η) -coordinate system: [Robert D. Cook, 2002]

$$dx dy = J d\xi d\eta \quad (2.10)$$

The general formulation of the stress stiffness matrix is: [Robert D. Cook, 2002]

$$[K_\sigma] = \int [G]^T \begin{bmatrix} s & 0 & 0 \\ 0 & s & 0 \\ 0 & 0 & s \end{bmatrix} [G] dV \quad (2.11)$$

where

$$s = \begin{bmatrix} \sigma_{x0} & \tau_{xy0} & \tau_{xz0} \\ \tau_{xy0} & \sigma_{y0} & \tau_{yz0} \\ \tau_{xz0} & \tau_{yz0} & \sigma_{z0} \end{bmatrix} \quad (2.12)$$

$[G]$ is obtained by an appropriate differentiation of the shape functions. The element displacement field, $\{u\}$, is given by: [Robert D. Cook, 2002]

$$\{u\} = [N]\{d\} \quad \text{where} \quad \{u\} = [u \ v \ w]^T \quad (2.13)$$

$[N]$	Shape function matrix
u	Displacement in u -direction
v	Displacement in v -direction
w	Displacement in w -direction

Now that the finite element formulations are formulated the procedure for setting up a model in Abaqus is described.

2.2 Abaqus Model

In this section the model in Abaqus and the procedure of setting up a model are described. Setting up the model in Abaqus is a procedure of some steps that are required for the model to run.

2.2.1 Shell Element

The first step of modelling the shell structure is defining the parts which define the entire structure, in this case only one element is required. The element is created as a shell element which can be thought of as a combination of a plate and a disc element. Disc elements can be used to analyse structures subjected to in-plane forces and it has two in-plane translation degrees of freedom (d.o.f.). A plate element has one out of plane translation d.o.f. and two out of plane rotational d.o.f. In addition to the five d.o.f. that are provided by the plate and disc a sixth d.o.f is added which is a rotational d.o.f. known as a drilling d.o.f. The geometry, dimensions and material properties of the shell element are determined later. The shell structure created in Abaqus is illustrated in Figure 2.2.

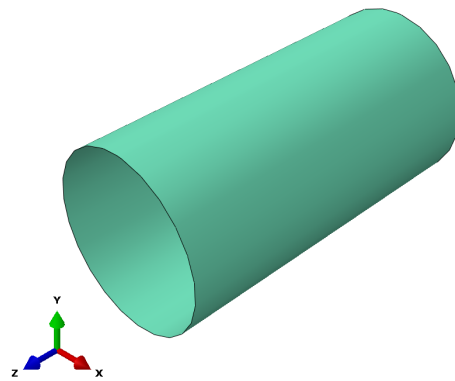


Figure 2.2: Shell structure with assigned material properties.

The shell thickness has an offset that starts from the middle surface and half of the thickness goes inwards and the other half goes outwards from the offset. The value of the radius is taken from the middle of the thickness which is used in the calculations.

2.2.2 Defining Sets and Surfaces

Before the boundary conditions are applied the sets and surfaces are defined. The set represents the edges of the cylinder where the supports, loads or both are applied. As a

default the cylinder is created in a 3D-space using a cartesian coordinate system. For the load scenario with shear on the shell edge it is more feasible if it is changed to a cylindrical coordinate system using (r,θ,z) -coordinates when the loads are applied.

2.2.3 Boundary Conditions

The boundary conditions for the model consists of the supports which defines the constraints and the loads which are applied to the structure.

Supports

For the shell structure it is assumed that the bottom part is clamped i.e. all directions and rotations are fixed and the top part is pinned so it can move and rotate along the axial length which is the z -axis while all the other directions are fixed. These boundary conditions are used in all load scenarios. The bottom boundary condition is illustrated in Figure 2.3. The type of boundary condition of the shell structure is related to the silo structure shown in Figure 1.1 (p. 1).

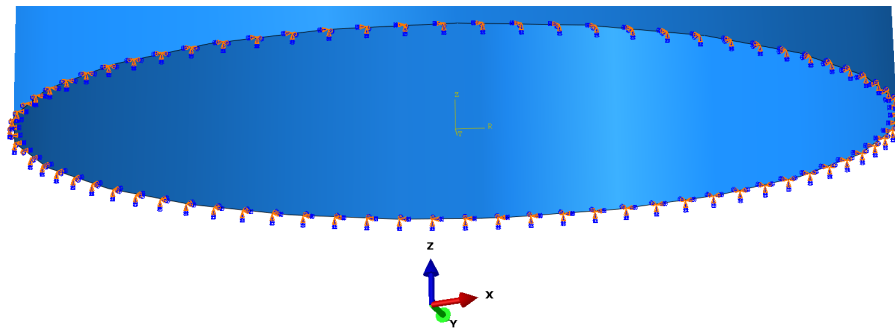


Figure 2.3: Bottom boundary condition of the shell structure.

Loads

The shell structure is exposed to four different load scenarios which are a meridional compression, a circumferential compression, a shear stress and a combination of them all. These load scenarios are all different from each other. Abaqus does not use units and therefore, the user has to be aware of this when a combination of loads is created. The input of all the loads are a reference value of 1.0 and thus the output which is an eigenvalue, λ , is used to create the combination of loads. For the meridional compression the load is applied in the axial direction which in this case is the z -axis thus it does not matter whether the load is applied in the cartesian or the cylindrical coordinate system. For the shear stress it is highly relevant to use the cylindrical coordinate system compared to the cartesian because in this case the load for the shear is applied in the θ -direction which is the circumference of the cylinder. It is equally relevant for the circumferential compression, but in this case

the load is applied in the radial-direction. The load scenarios are illustrated in Figure 2.4.

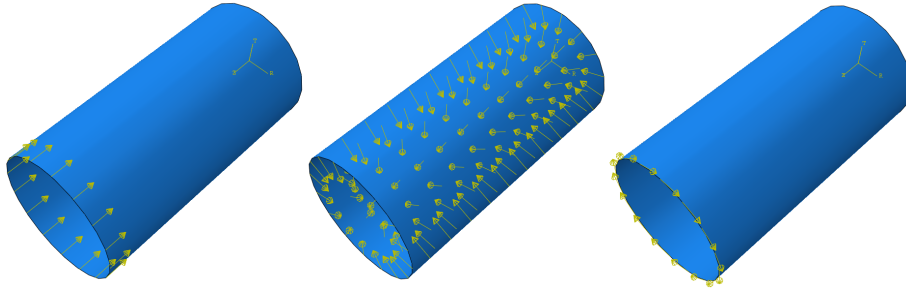


Figure 2.4: Shell structure with meridional compression, circumferential compression and shear stress, respectively.

2.2.4 Mesh

The shell element is created with either triangular or quadrilateral elements. In order to choose the best type of elements a convergence analysis is performed. Each node has a certain amount of d.o.f. which are the ones determining the displacement in different directions or rotations. The triangular element is lacking the drilling d.o.f., θ_w , thus it only has five d.o.f. per node., whereas the quadrilateral element has a maximum of six d.o.f per node: Three displacements and three rotational d.o.f. This makes it perfectly suitable for solving three dimensional problems. A shell element with a quadrilateral shape is presented in Figure 2.5.

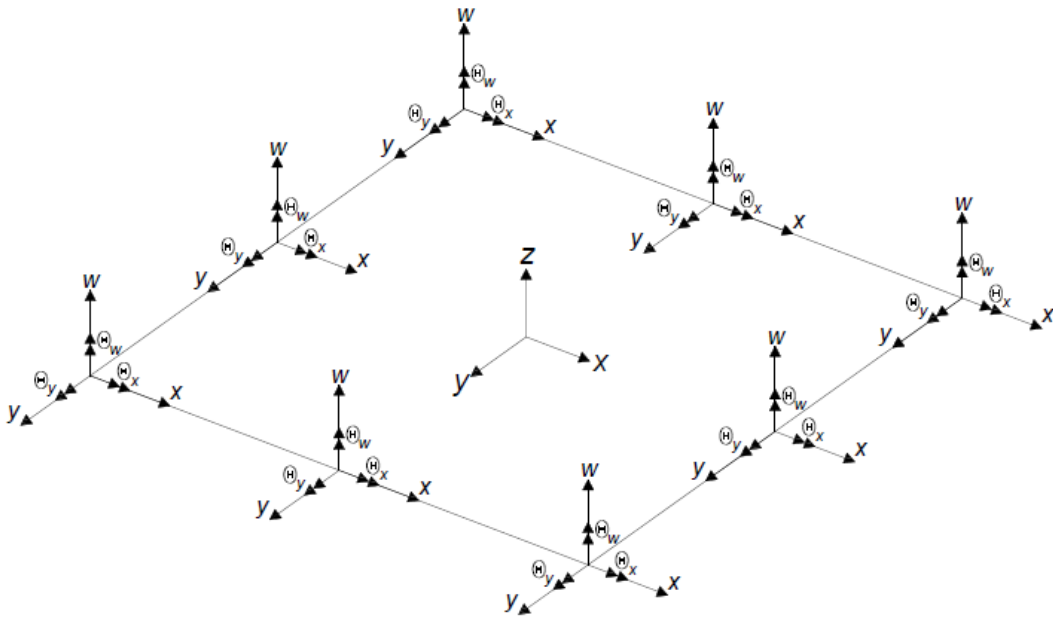


Figure 2.5: Quadrilateral shell element [Robert D. Cook, 2002].

The quadrilateral element can either be a linear element with four nodes or a quadratic element with eight nodes. The linear elements are not very accurate to use to model a curving structure like the cylinder because every side of the element has to be linear, whereas the sides of the quadratic elements can curve due to the extra amount of nodes per element. Thus in order to get the most accurate results with the least amount of computational power the quadratic quadrilateral elements, S8R, are chosen as the meshing elements. A convergence analysis is done in order to provide the most optimal mesh size for the models. Too fine a mesh results in too much computational power and too coarse a mesh results in too unreliable results. The convergence analysis is performed for each of the load scenarios which provides the amount of d.o.f. which is required before the model is converged for the critical buckling stress. In order to convert the loads into stresses the following equations are used: [EN-3, 2004]

$$\sigma_{z_{cr}} = \frac{P_z}{t} \quad (2.14)$$

$$\sigma_{\theta_{cr}} = P_n \cdot \frac{r}{t} \quad (2.15)$$

$$\tau_{\theta_{cr}} = \frac{P_{\theta}}{t} \quad (2.16)$$

These equations are comparable with Equation (2.2) where a reference load input is inserted. Thereafter, an eigenvalue, λ , is obtained which then is multiplied on the reference load in order to obtain the critical load which is used to calculate the critical stresses in equations (2.14)-(2.16). The convergence analysis is illustrated in Figure 2.6.

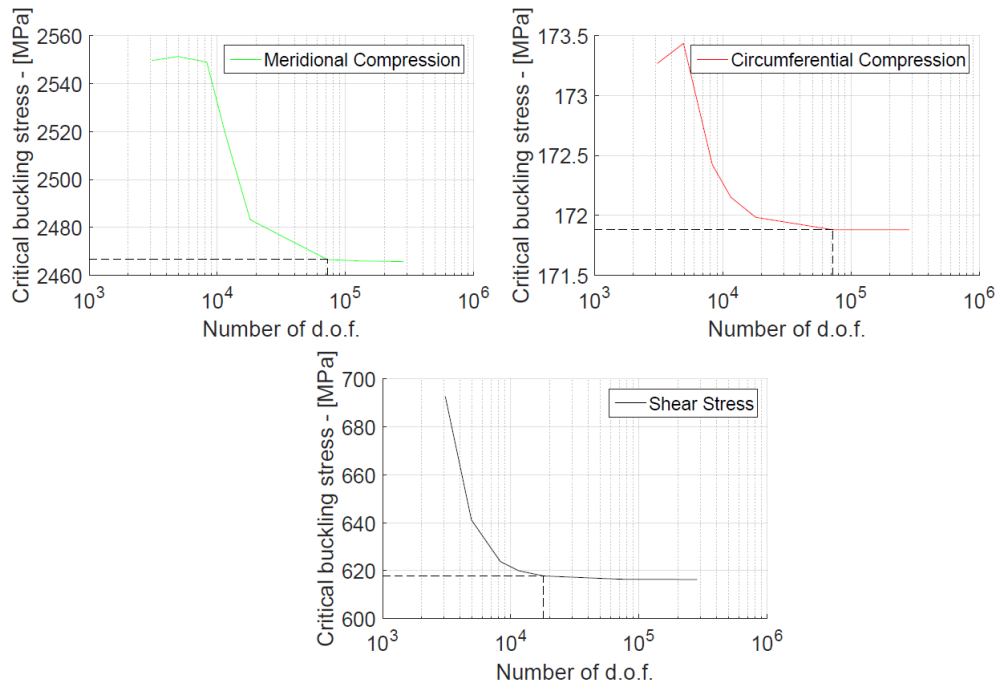


Figure 2.6: Convergence analysis for the different load scenarios.

The model exposed by shear stress is converging at 18030 d.o.f. and the models exposed by a meridional compression and a circumferential compression both converges at 72060 d.o.f. Therefore, these two different meshes are used in the calculations. All results are enclosed on Appendix CD *Circular Cylinder/Convergence analysis*.

The 18030 d.o.f. are represented by 3005 nodes and 975 elements whereas the 72060 d.o.f. are represented by 12010 nodes and 3950 elements. The mesh of the structure with 975 elements is illustrated in Figure 2.7.

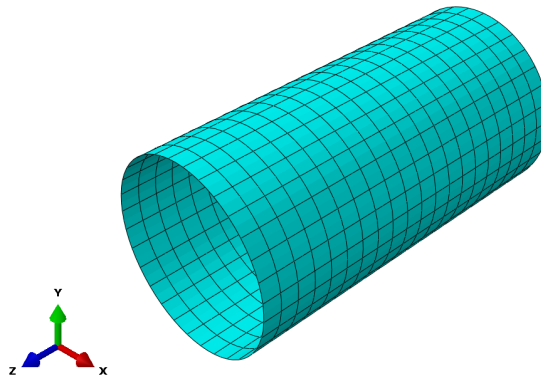


Figure 2.7: Mesh of shell structure with 975 elements.

Now that the general formulation and the models for the finite element method is described for the software Abaqus the results for the circular cylinder are presented in the following chapter.

Circular Cylinder

In this chapter the buckling stress for a shell is determined analytically by using EN-3 [2004] and numerically by using the software Abaqus. In EN-3 [2004] shell structures are only determined for cylindrical structures, by making the structure more complicated e.g. a more complex geometry it requires more advanced calculations or the use of finite element method.

For cylindrical shells the buckling stress depends among other things on the applied load. In EN-3 [2004] different load scenarios are given for a cylindrical shell. In these load scenarios the critical buckling stress is calculated individually to determine when a cylindrical shell buckles with these loads. Afterwards, the buckling stress of the shell is determined when the loads are combined. In EN-3 [2004] it is seen that the calculations for shells are primarily those used for silos or containers which has circular cross sections with the previously mentioned load scenarios.

3.1 Properties of the Cylindrical Shell

In order to have comparable results from the analytical approach from EN-3 [2004] and the numerical approach by using the FE software Abaqus the properties and geometries for the shell need to be the same. Otherwise, the results are not comparable since the models are not identical. The material for the cylinder is chosen to be steel. In this chapter the geometries and general properties, if nothing else is specified, are:

- Length of cylinder is two times the diameter; $l = 2D$
- Thickness of cylinder is 1% of the diameter; $t = 0.01D$

From the above mentioned properties the ratio between t/r and l/r is constant independent on the chosen diameter. This is an important observation since all the formulas from EN-3 [2004] which is used to calculate the critical buckling stress in Appendix B only depend on these ratios and not the actual chosen diameter of the cylindrical shell. Though, in order to calculate the results of the cylinder a Young's modulus of 210 000 MPa and a diameter of 100 mm are chosen. Furthermore, the cylinder is assumed clamped at the bottom and pinned in the top and the geometry of the shell is shown in Figure 3.1.

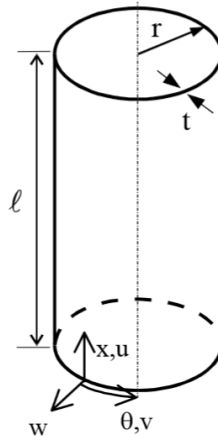


Figure 3.1: Geometry of the cylinder [EN-3, 2004].

3.2 Circular Cylinder with Meridional Compression

In this section the buckling stress for a circular cylinder exposed to a meridional compression as shown in Figure 3.2 is calculated. All formulas used to calculate the buckling stress are given in Appendix B.1.

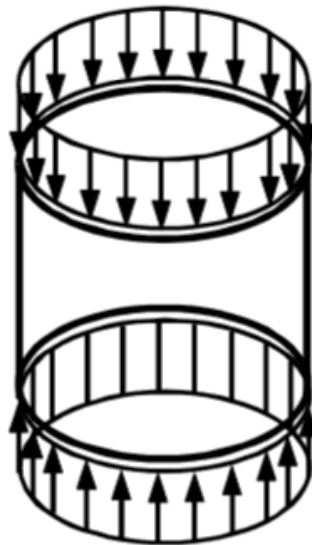


Figure 3.2: Shell with meridional compression [EN-3, 2004].

By looking at the formulas in Appendix B.1 it is seen that for a meridional compression the critical buckling stress is multiplied by a factor which takes into account the length of the cylinder and thereby the slenderness. For a long cylinder the factor is lower than for a short cylinder since a long cylinder needs to be exposed to a lower stress in order to buckle compared to a short cylinder. It is also noticed that for a certain length of the cylinder,

the factor becomes constant even though the length is increased. This concept is analysed further in a later section. The difference between long, medium-length and short cylinders for the given diameter and thickness in Section 3.1 is shown in Figure 3.3. Therefore, the chosen cylinder is defined as long for a meridional compression since the length is 200 mm.

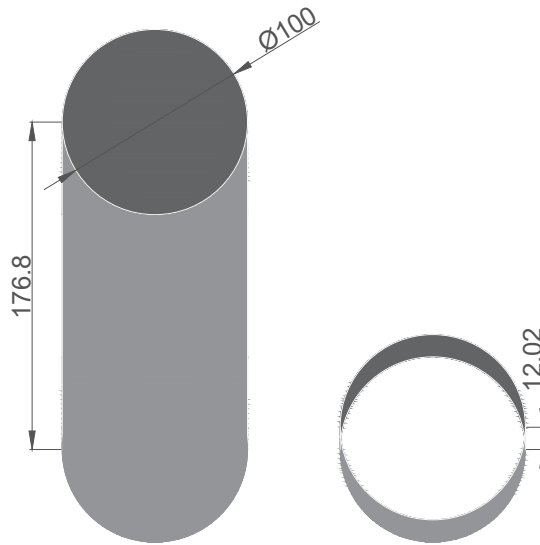


Figure 3.3: Circular shell with the critical length which defines short, medium-length and long cylinders for the given diameter and thickness. All units in mm. Left cylinder: Defines the length at the transition between long and medium-length cylinder, Right cylinder: Defines the length at the transition between medium-length and short cylinder

It is also noticed that the critical buckling stress is proportional to the elasticity modulus cf. Appendix B.1. Thereby, if the strains are plotted instead of the stresses, by dividing the stresses with the elasticity modulus, the buckling criterion is independent of the elasticity modulus.

When calculating the design buckling stress for all the load scenarios the formulas from EN-3 [2004] in Appendix B.1 are using an imperfection reduction factor when calculating the buckling stress which takes into account the influence of imperfection which depends on the fabrication quality of the shell structure. It is also noticed, that the critical buckling stress for all the load scenarios depends on the ratio between the thickness and the radius and a dimensionless factor which is a relation between the length, radius and thickness. In other words, the chosen value of the diameter in Section 3.1 does not change the results as long as the relation between the geometries are the same.

The critical meridional buckling stress is calculated to 2518.7 MPa. All calculations are enclosed on Appendix CD *Circular Cylinder/Buckling stress*.

3.3 Circular Cylinder with Circumferential Compression

In this section the buckling stress for a circular cylinder loaded as shown in Figure 3.4 is calculated. All formulas used to calculate the buckling stress are given in Appendix B.2.

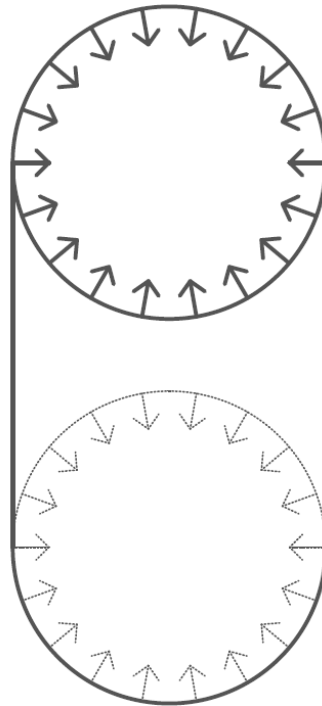


Figure 3.4: Shell with circumferential compression.

The same observations are seen in the formulas for the critical buckling stress for a cylinder exposed to a circumferential compression as for a cylinder exposed to a meridional compression. The critical circumferential buckling stress is calculated to 170.8 MPa. All calculations are enclosed on Appendix CD *Circular Cylinder/Buckling stress*.

3.4 Circular Cylinder with Shear Stress

In this section the buckling stress for a circular cylinder exposed to a load as shown in Figure 3.5 is calculated. All formulas used to calculate the buckling stress are given in Appendix B.3.

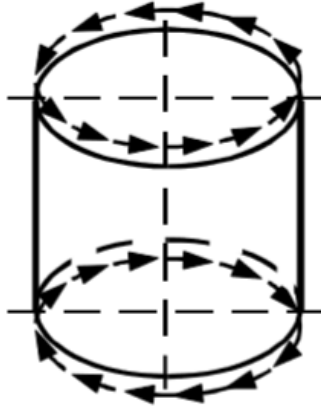


Figure 3.5: Shell with shear stresses [EN-3, 2004].

For a cylinder with shear stress the elasticity modulus is also proportional to the critical buckling stress. Furthermore, the critical buckling stress depends on a factor which depends on the length of the cylinder. For short cylinders the factor is higher than for long cylinders which implies that buckling occurs at a lower stress for a long cylinder than for a short cylinder.

The critical shear buckling stress is calculated to 592.3 MPa. All calculations are enclosed on Appendix CD *Circular Cylinder/Buckling stress*.

3.5 Circular Cylinder with Combined Loads

The buckling stress for a cylinder exposed to a combination of the different loads are calculated in this section and all the formulas used are given in Appendix B.4.

The significant values of the membrane stresses for the different loads are varied in the interval 0 to 1 times the corresponding critical buckling stress. This way the design criteria in Equation (B.33) is plotted in a coordinate system with a surface describing the amount of stresses that can be applied before buckling occurs. The plot is shown in Figure 3.6. A contour plot is shown in Figure 3.7 since these plots are easier to compare than the 3-dimensional plots. All calculations are enclosed on Appendix CD *Circular Cylinder/Buckling stress*.

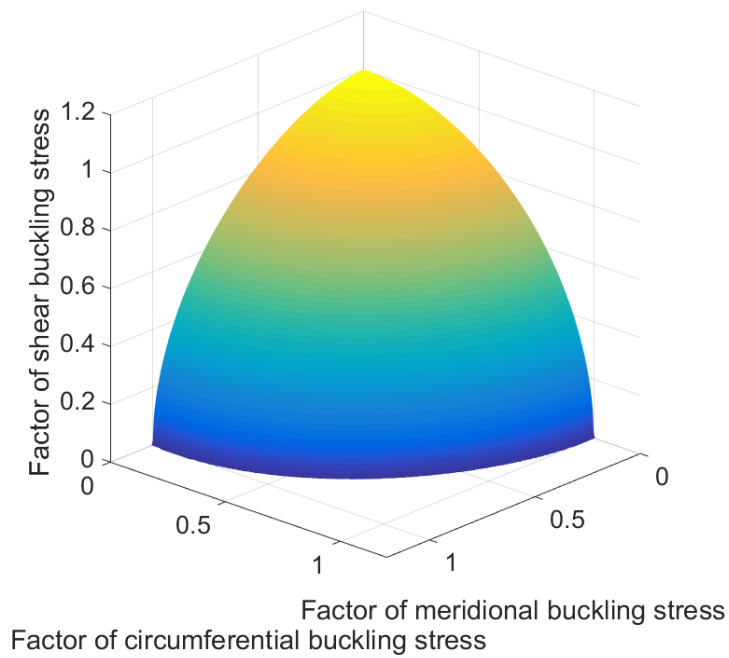


Figure 3.6: Factorized buckling criteria for load combination.

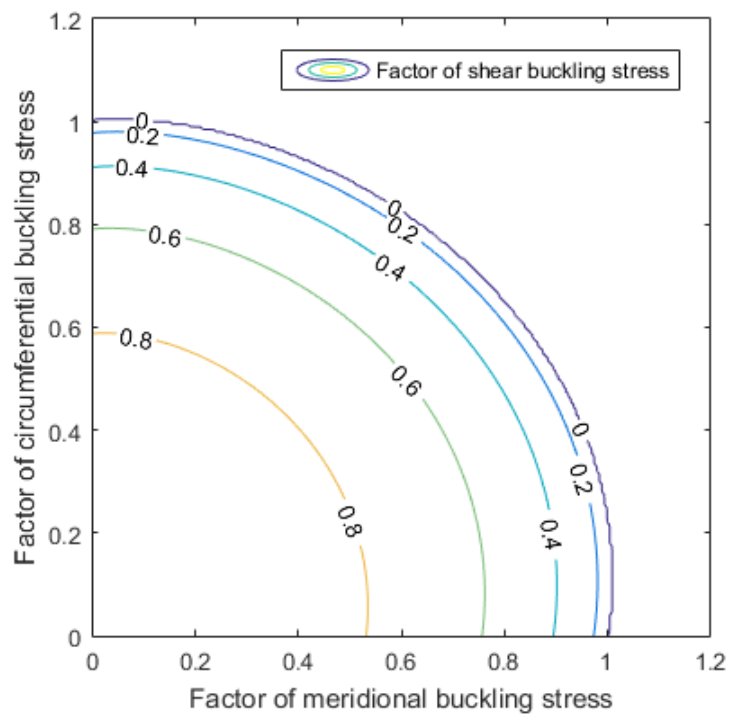


Figure 3.7: Contour plot of the factorized buckling criterion for load combination.

From Figures 3.6 and 3.7 it is seen that the cylinder with all load scenarios acting on it can resist a higher meridional compression in combination with a circumferential compression

and/or a shear stress acting on the same time compared to a meridional compression acting alone. The same principle applies for other combinations as seen in the figures. This is not unexpected since some of the loads might work in favour of the buckling stress whereas a higher stress is required before the cylinder starts buckling.

If the factor instead is multiplied with the corresponding buckling stress the buckling surface is as shown in Figure 3.8. Notice that the axes are different. Here it is easier to see that the magnitude of the meridional buckling stress is larger than the magnitude of the shear buckling stress. The magnitude of the meridional buckling stress is also larger than the magnitude of the circumferential buckling stress which is as expected since the circumferential buckling stress acts on a larger area.

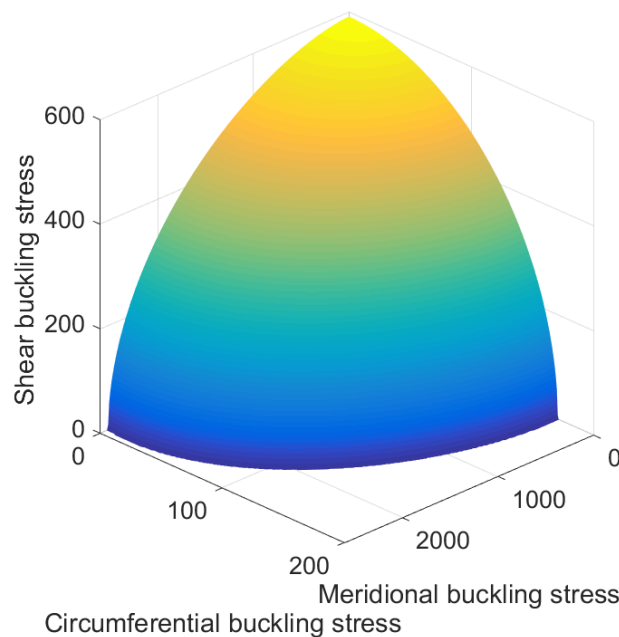


Figure 3.8: Buckling criteria with load combination. All values are in MPa.

3.6 Parameter Study

In this section a parameter study of the different input parameters are examined in order to determine how the buckling stress of the cylinder depends on the different parameters. The different influence of the parameters that are examined are:

- the length-diameter ratio
- the thickness
- Young's modulus

3.6.1 Changed Length-Diameter Ratio

The equations used in Sections 3.2 - 3.4 are now recalculated with a changed length-diameter ratio where the diameter is the same, but the length is varied. By doing this, the buckling stress is calculated for the three different load scenarios with a varying length. The results are given in Figures 3.9 - 3.10 where the critical buckling stress is normalized with respect to Young's modulus. All calculations are enclosed on Appendix CD *Circular Cylinder/Changed DL ratio*.

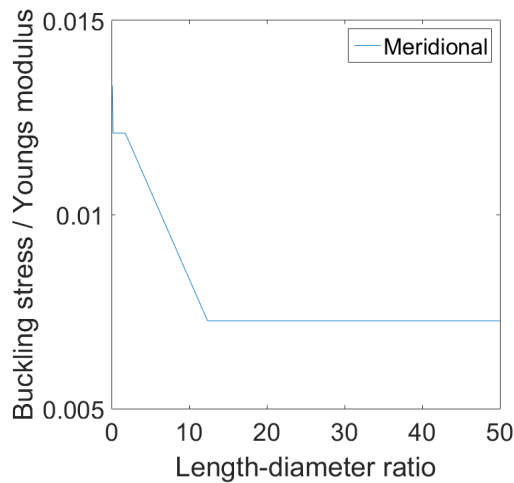


Figure 3.9: Buckling stress divided by Young's modulus as a function of the length-diameter ratio for cylinder with meridional compression.

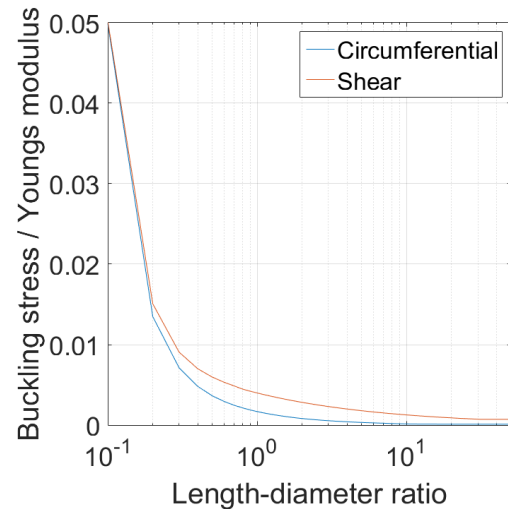


Figure 3.10: Buckling stress divided by Young's modulus as a function of the length-diameter ratio for cylinder with circumferential compression and shear stress.

In general for all the load scenarios the buckling stress decreases when the length-diameter ratio of the cylinder increases. Furthermore, the buckling stress decreases until it reaches a certain stress where after it remains constant for an increasing length-diameter ratio cf. Figures 3.9 - 3.10.

For the cylinder with meridional compression the curve has some significant points where the direction of the curve change drastic. This is due to the factor depending on the length of the cylinder which changes for a certain length of the cylinder. Therefore, the drastic changes on the curve corresponds to the cylinder going from short to medium-length to long. It is also noticed that the buckling stress divided by Young's modulus becomes constant for a certain length. This is as expected since the study of the equations from EN-3 [2004] revealed that the critical buckling stress depends on a factor which becomes constant for a certain length. The reason for this might be explained by the fact that a global buckling occurs for the cylinder if it is acting like a beam. The critical Euler load is

calculated in Appendix C.1. Here it is seen that the critical Euler load for a beam with a simple support in one end and a fixed support in the other end is 2268.1 MPa. The critical buckling stress from EN-3 [2004] is also calculated for the same Young's modulus and is 1524.6 MPa which is in the same order of magnitude but less than the Euler load. The fact that global buckling occurs for the cylinder is also obtained when modelling the cylinder with finite elements in Abaqus cf. Appendix C.2. From this it is concluded that EN-3 [2004] is taking into account the global buckling for a Euler load of the system and it takes into account some safety since it occurs for a shorter length of the cylinder than the actual calculated critical Euler buckling load. The safety corresponds approximately to a factor 1.5.

For the cylinder with circumferential compression or shear stress the critical buckling stress is high for very short cylinders and then decreases for increasing length. For long cylinders the critical buckling stress goes towards zero which corresponds to the fact that it does not take much stress to make a long cylinder buckle.

If instead all the parameters are the same as defined in Section 3.1 except the length is shortened with a factor ten then the factorized buckling surface looks as shown in Figure 3.11. In the figure the buckling surface is plotted as a contour plot. The calculations are enclosed on Appendix CD *Circular Cylinder/Changed DL ratio contour*.

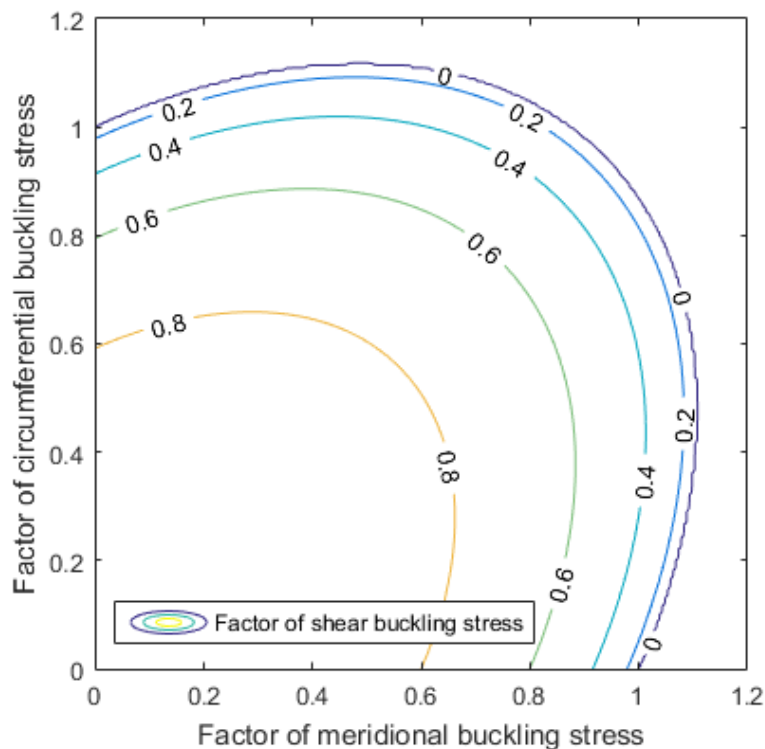


Figure 3.11: Factorized buckling criteria for load combination with reduced length.

From Figure 3.11 it is seen that the buckling surface is expanded compared to Figure 3.7. This indicates that in combination with other loads a larger stress can be applied before buckling occurs.

3.6.2 Changed Thickness

Again the equations used in Sections 3.2 - 3.4 are recalculated but with a changing thickness where the diameter and length of the cylinder are the same as the original conditions specified in Section 3.1. By doing this, the buckling stress is calculated for the three different load scenarios with a varying thickness. The results are given in Figure 3.12 where the critical buckling stress is normalized with respect to Young's modulus. All calculations are enclosed on Appendix CD *Circular Cylinder/Changed thickness*.

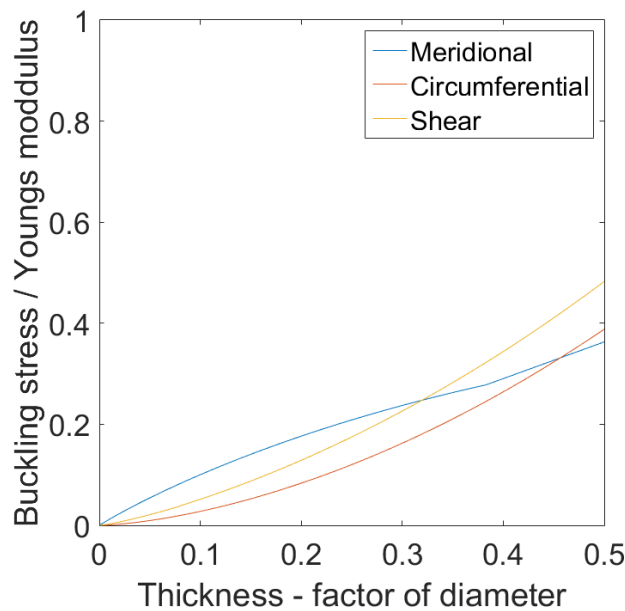


Figure 3.12: Buckling stress as a function of thickness.

In Figure 3.12 it is seen that the buckling stress increases for increasing thickness of the cylinder. This is as expected since a cylinder with higher thickness should be exposed to a larger stress before it starts to buckle. It is also seen, that the increase of the curves for increasing thickness is larger for circumferential and shear stress. This indicates that it is easier for a cylinder with circumferential compression or shear stress to buckle than a meridional compression for increasing thickness.

Again, if all the parameters are the same as defined in Section 3.1 except the thickness is changed to 0.1% of the diameter instead then the factorized buckling surface will look as shown in Figure 3.13. In the figure the buckling surface is plotted as a contour plot. The calculations are enclosed on Appendix CD *Circular Cylinder/Changed thickness contour*.

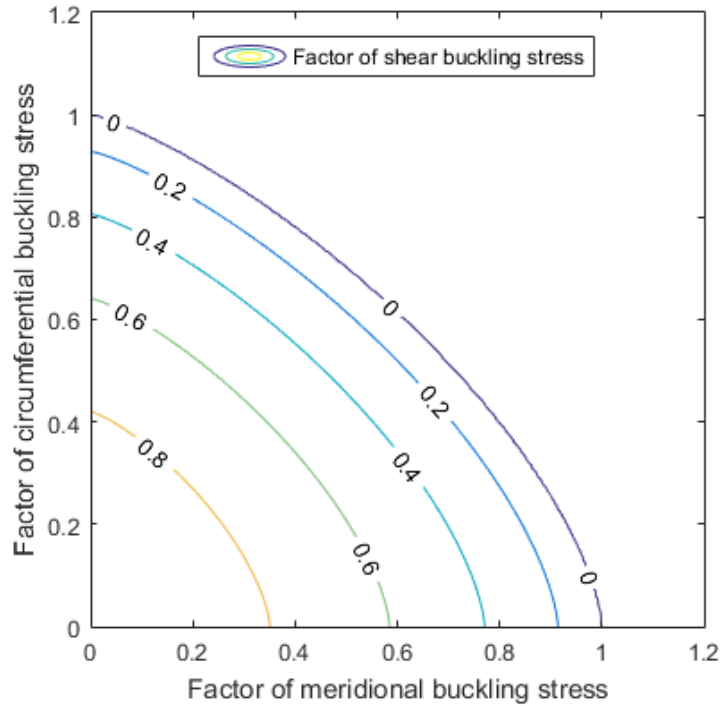


Figure 3.13: Factorized buckling criteria for load combination with reduced thickness.

From Figure 3.13 it is seen that the buckling surface is condensed compared to Figure 3.7. Since the buckling surface is condensed the buckling is more critical for the loads acting simultaneously compared to a thicker shell.

3.6.3 Changed Young's Modulus

It is concluded from the study of the formulas from EN-3 [2004] that Young's modulus is proportional to the critical buckling stress. If all the parameters are the same as defined in Section 3.1 except that Young's modulus is decreased with a factor 10 then the factorized buckling surface will look as shown in Figure 3.14. In the figure the buckling surface is plotted as a contour plot. The calculations are enclosed on Appendix CD *Circular Cylinder/Changed E contour*.

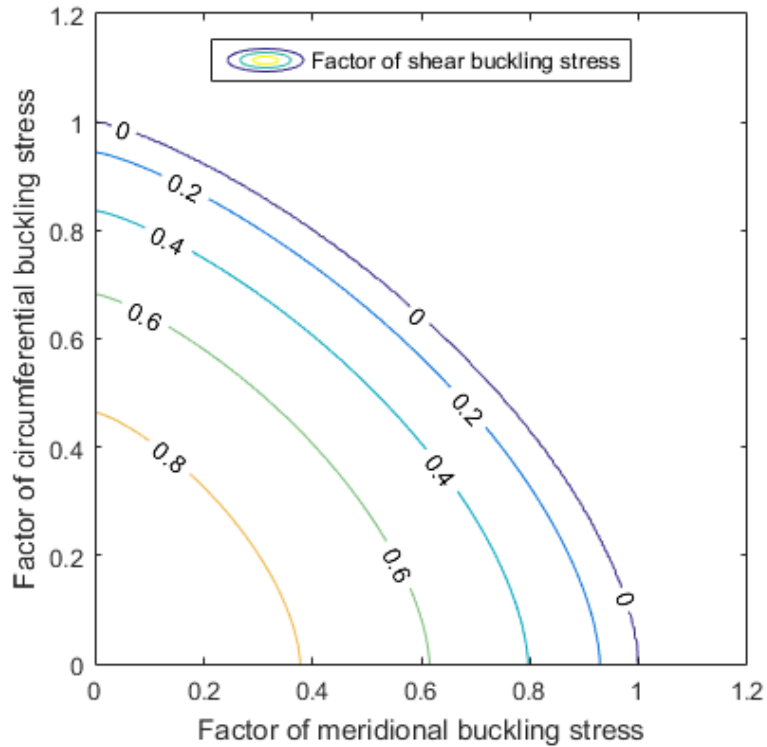


Figure 3.14: Factorized buckling criteria for load combination with reduced Young's modulus.

From Figure 3.14 it is seen that the buckling surface is condensed compared to Figure 3.7. It is also noticed that the difference between the buckling surface for the reduced elasticity modulus compared to the original buckling surface in Figure 3.7 is less than the influence of the length diameter ratio cf. Figure 3.11.

3.6.4 Changed Thickness and Length

If different contour plots are plotted for changing lengths and thickness's the results are as seen in Figure 3.15.

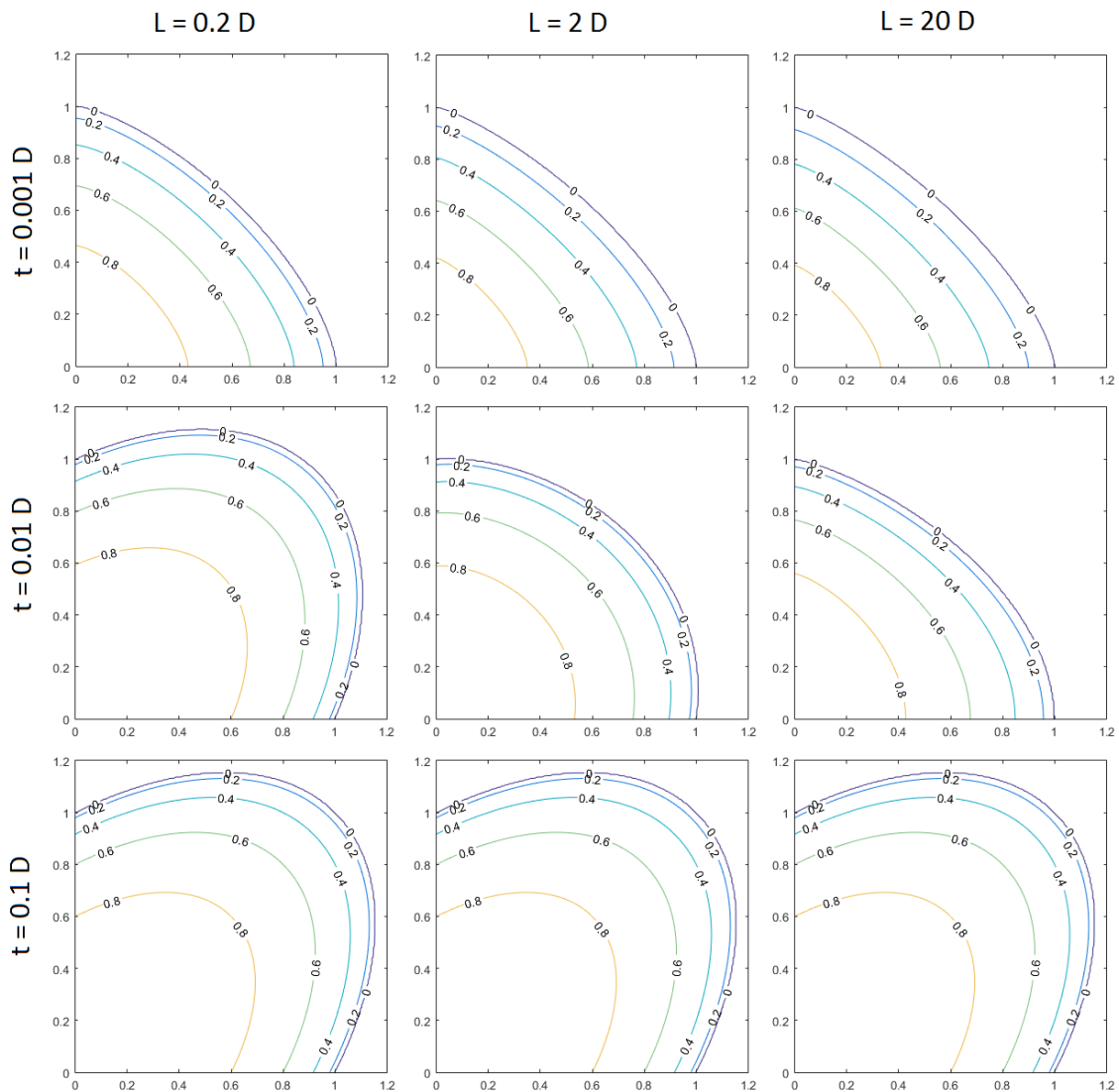


Figure 3.15: Contour plots of changed parameters.

From Figure 3.15 it is seen that for cylinders with a small or large thickness compared to the diameter the length only has a small influence on the stress that can be applied compared to the critical buckling stress. But for cylinders with a medium thickness compared to the diameter the length has a large influence on the amount of stress that can be applied compared to the critical buckling stress. For short cylinders a higher stress compared to the diameter can be applied before buckling happens.

Now that the critical buckling stress is obtained analytically by the use of EN-3 [2004] the same models are created by the use of the finite element method.

3.7 Numerical Results

All the results for the different models are obtained for each load scenario by the use of the numerical software Abaqus. In order to obtain the buckling stress, the lowest eigenvalue for each of the load scenarios are required which is the eigenvalue at their first eigenmode. This is used because the first eigenmode is the most simple buckling mode the structure obtains and therefore the first buckling mode it undergoes.

3.7.1 Load scenarios

When the cylindrical shell is loaded with a meridional compression, a circumferential compression or a shear stress the deformation is as shown in Figure 3.16.

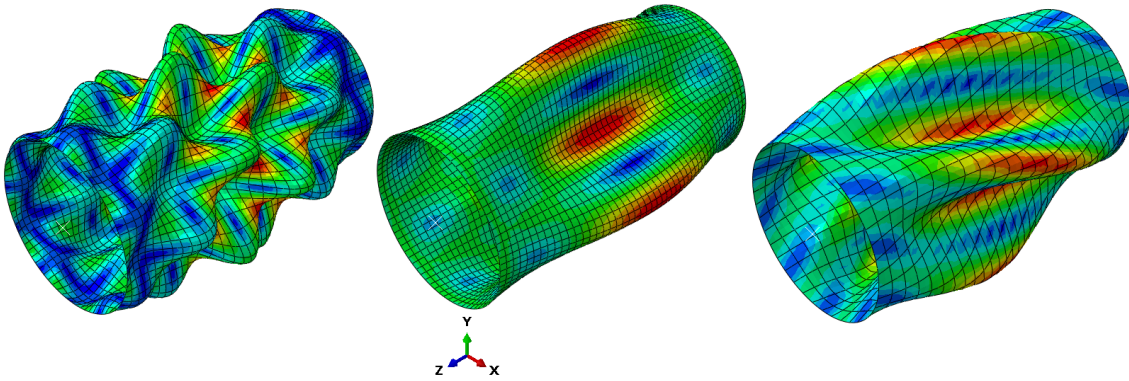


Figure 3.16: Deformation of shell structure with meridional compression, circumferential compression and shear stress, respectively.

Equations (2.14) - (2.16) are used in order to convert the results into buckling stresses:

$$\begin{aligned}\sigma_{z_{cr}} &= \frac{2466.5 \text{ N/mm}}{1 \text{ mm}} = 2466.5 \text{ MPa} \\ \sigma_{\theta_{cr}} &= 3.47 \text{ N/mm}^2 \cdot \frac{49.5 \text{ mm}}{1 \text{ mm}} = 171.9 \text{ MPa} \\ \tau_{\theta_{cr}} &= \frac{614.8 \text{ N/mm}}{1 \text{ mm}} = 614.8 \text{ MPa}\end{aligned}$$

The comparison of the critical buckling stresses is shown in Table 3.1. Furthermore, the deviation between the results from the analytical approach and the results obtained from the numerical approach are likewise shown. It is seen that the model with circumferential compression has the smallest deviation and that the shear stress has the highest deviation. Furthermore, only the model with a meridional compression gives a numerical result lower than the analytical results.

Table 3.1: Comparison of results from analytical and numerical approach.

Load scenario	Analytical	Numerical	Deviation
Meridional compression	2518.7 MPa	2466.5 MPa	-2.1%
Circumferential compression	170.8 MPa	171.9 MPa	0.6%
Shear stress	592.3 MPa	614.8 MPa	3.8%

3.8 Combination of Loads

Now all the loads are analysed when they act simultaneously on the cylinder. Some certain points on Figure 3.6 and 3.7 are chosen in order to make the comparison between the results. To do so the cylindrical shell is exposed by the different load scenarios separately and the eigenvalue obtained in each of these models are used to define the loads at buckling. These loads are then multiplied with the corresponding factors from Table 3.2 to create the combination of loads. The coordinates for the chosen points are listed in Table 3.2 and shown in Figures 3.17 and 3.18. The chosen points are all lying on the failure surface i.e. their factorized critical buckling stress are 1. The points which are chosen are all lying on a curve which begins at a factorized shear stress of 1 and goes towards 0 with an angle of 45° and the points where only one load is acting with each a factorized load of 1 are also chosen.

Table 3.2: Coordinates of chosen points.

Chosen points	x-coordinate (Meridional)	y-coordinate (Circumferential)	z-coordinate (Shear)
1	0	1	0.0
2	1	0	0.0
3	0.7275	0.7275	0.0
4	0.7074	0.7075	0.2
5	0.6545	0.6545	0.4
6	0.5595	0.5595	0.6
7	0.4020	0.4020	0.8
8	0	0	1.0

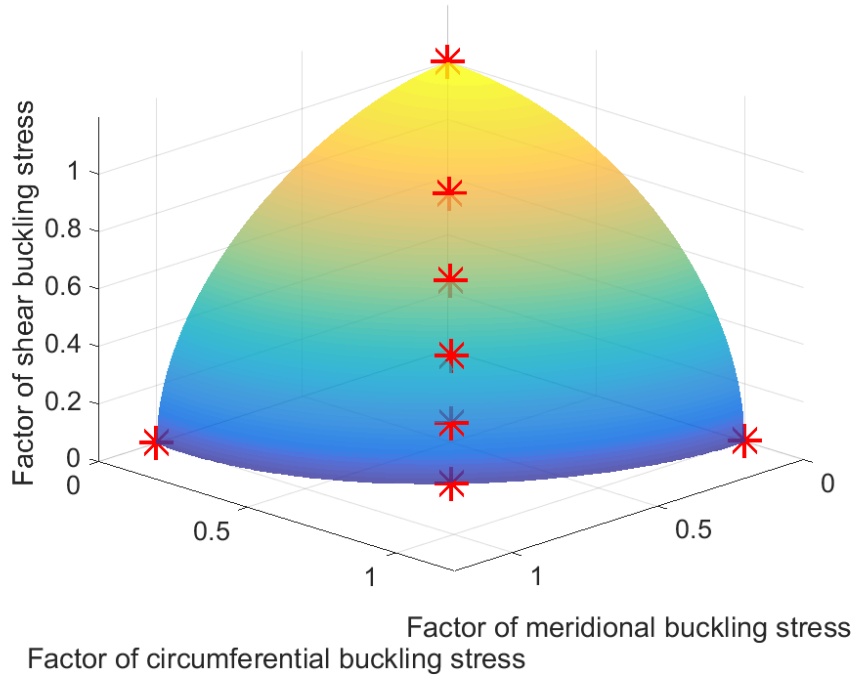


Figure 3.17: Factorized buckling criterion for load combination with chosen points.

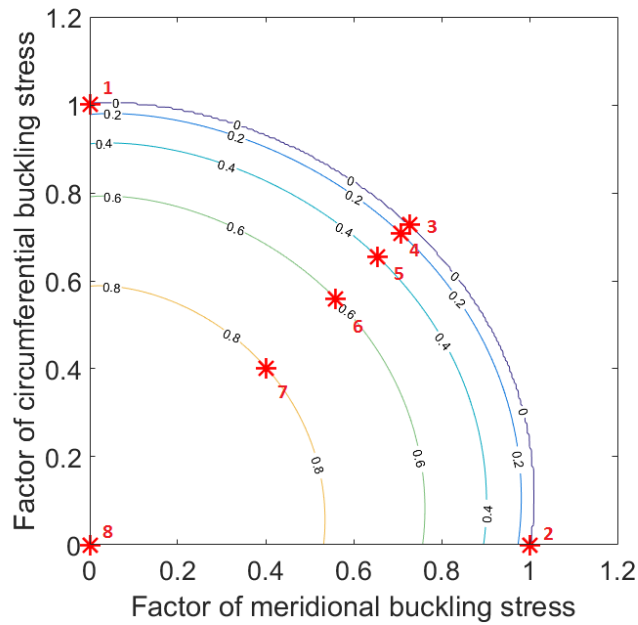


Figure 3.18: Factorized buckling criterion for load combination with chosen points.

The coordinates represents the factorized critical buckling stress for each of the loads, thus these factors are multiplied by the eigenvalues used in order to create the models exposed

to a combination of the loads. The eigenvalues of these models should be as close to 1 as possible because that signifies that the points calculated in Abaqus are lying on the failure surface.

The factorized critical buckling stress which are represented by the coordinates of each point is used in Abaqus for the load combination to calculate the deviation between the numerical results and the analytical results. It is expected that the points obtained through Abaqus is deviating from the results obtained from the analytical approach due to the deviation that is seen in Table 3.1. The results from each of these points are listed in Table 3.3. It is seen that all the points have a lower buckling stress than the analytical approach except when only a meridional compression is acting on the cylinder.

Table 3.3: Results of all of the chosen points.

Chosen points	Eigenvalue	Deviation
1	-	0.60%
2	-	-2.10%
3	0.9505	4.95%
4	0.9450	5.50%
5	0.9698	3.02%
6	0.9974	0.26%
7	0.9424	5.76%
8	-	3.80%

Another approach to compare the numerical results with the analytical results is to obtain the exact points where buckling occurs in Abaqus. For this approach one load is locked, e.g. the shear stress is locked at a factor 0.8 of the critical buckling stress. Then first a linear static analysis is performed which creates some stresses in the cylinder. Afterwards, the two remaining loads are added in a buckling analysis and increased until buckling occurs. This is done for two points and for these two points the shear stress has been locked at a factor of 0.2 and 0.8 of the critical buckling stress. These two new points are marked with blue and are illustrated in Figure 3.19. From Table 3.3 it is seen that all the points are deviating from the analytical results thus it is expected the points 4b and 7b are also deviating from 4a and 7a, respectively. It is also noticed that 4b is deviating less from 4a than 7b is from 7a.

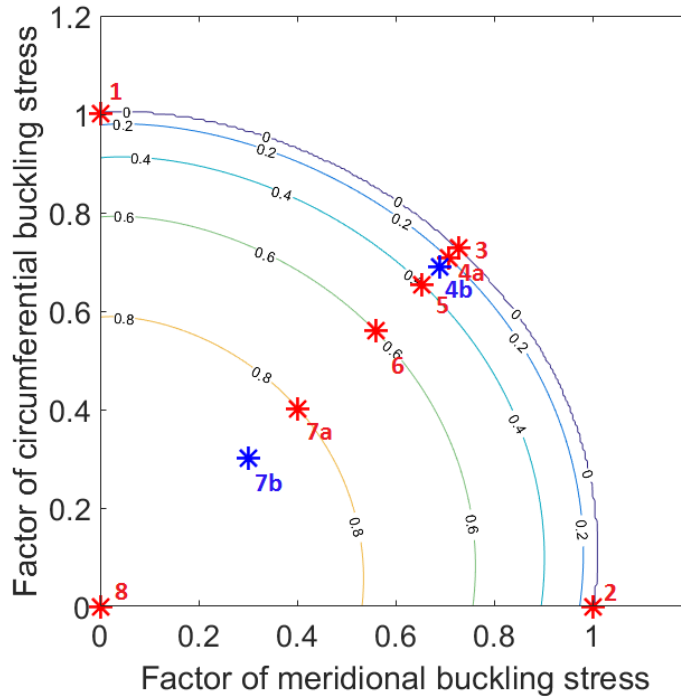


Figure 3.19: Factorized buckling criterion for load combination. Blue marks represents where buckling occurs in the Abaqus model.

Now a perfect circular cylinder is examined analytically and numerically when exposed to three different load scenarios and a combination of these loads. All these different load scenarios are examples given by EN-3 [2004] but imperfections in the shell is not accounted for. Therefore, the following chapter introduces imperfections in the geometry and what affect these imperfections have on the models.

Imperfection in Cylindrical Shells

This chapter describes the effect that non-linearity methods and imperfections in the structure have on the critical buckling stress.

Dependent on if it is materially- or geometrically non-linear elastic analysis that is used or both of them, and whether the imperfections are included or not, many different methods can be investigated. Therefore only a few of these methods are chosen. These are the linear elastic bifurcation analysis (LBA), geometrically non-linear analysis (GNA) and geometrically non-linear analysis with imperfections included (GNIA). These methods are investigated for the different load scenarios which are meridional compression, circumferential compression and shear stress.

4.1 LBA

First a linear elastic bifurcation analysis (LBA) is performed. This method is for the perfect structure, which means there is no change of geometry, no change in the direction of the loads and the material properties are constant. It obtains the results of the highest eigenvalue at which the shell buckles compared to any other methods where non-linearity and imperfections are included. This analysis provides the basis of the critical buckling stress which the cylinder can resist and is thus used for comparison with the methods involving imperfections and non-linearity. For each load scenario the model runs for 30 eigenmodes and by analysing these eigenmodes it is noticed that they are coming in pairs for load scenarios with meridional compression and circumferential compression. This indicates that the buckling behaviour is almost identical which is due to the chosen S8R elements. If the model is created with S4R elements this phenomenon do not occur.

This is illustrated on Figure 4.1 where the buckling behaviour is illustrated for the 11th and 12th eigenmode exposed to meridional compression. For the load scenarios with shear stress an additionally two almost identical buckling behaviours are generated and these are generated because the shear can either act in a positive or a negative direction but the eigenvalue remains the same. An example of these four almost identical buckling behaviours are illustrated in Figure 4.2. The four eigenvalues, λ_{13} , λ_{14} , λ_{15} and λ_{16} are 773.92, -773.92, 773.92 and -773.92, respectively. If more decimals are obtained in the results it is expected that the numbers vary slightly from each other. This is also expected

for the two eigenvalues obtained from the two eigenmodes in Figure 4.1.

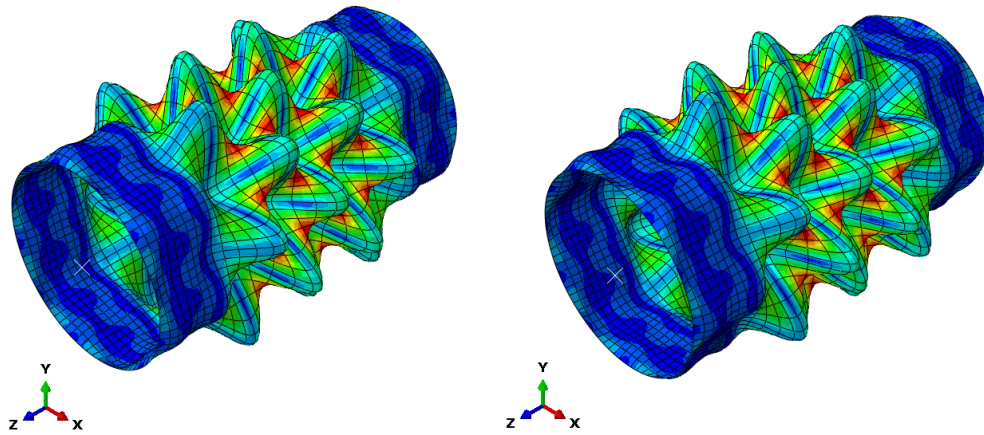


Figure 4.1: LBA for meridional compression for eigenmode 11 with $\lambda_{11} = 2507.7$ and eigenmode 12 with $\lambda_{12} = 2507.7$.

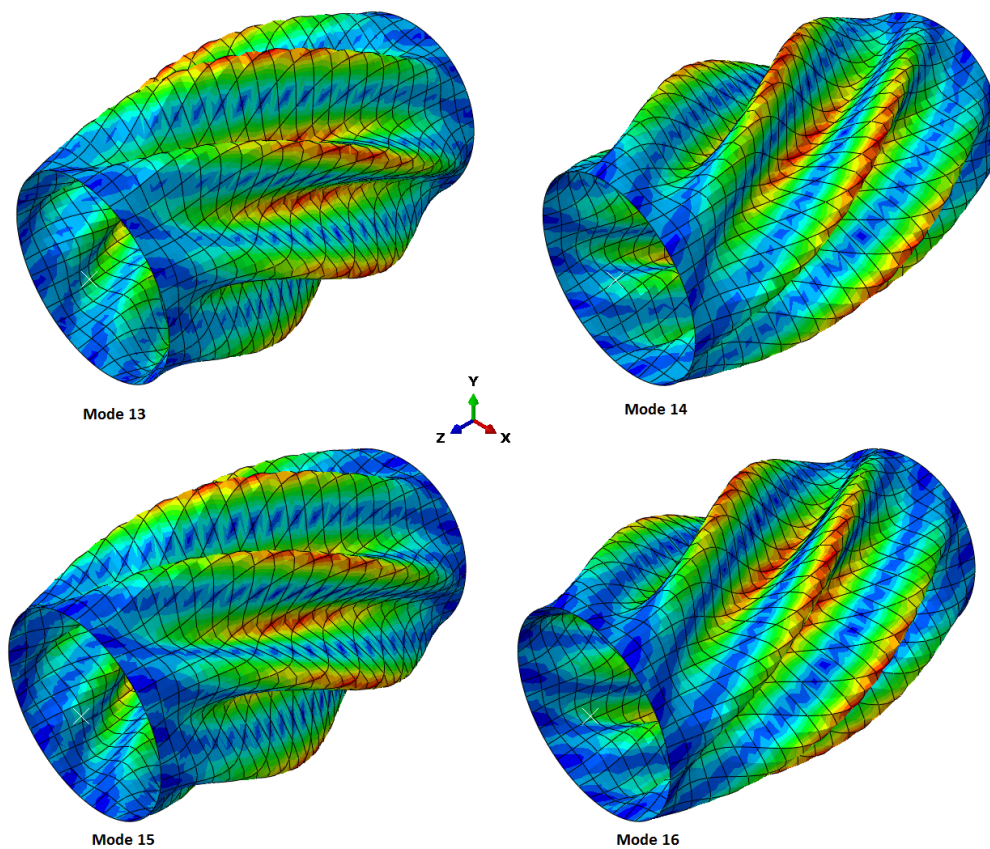


Figure 4.2: Four different eigenmodes illustrating the same buckling behaviour for shear stress.

Another thing that is noticed is the the eigenvalues from the 1st to the 30th eigenmode do not vary much in the case with the meridional compression. With the meridional compression from the 1st eigenmode to the 30th eigenmode the change of the eigenvalue goes from 2466.5 to 2534.6. This is a difference of 2.68%. For the two other load scenarios the difference are 68.1% and 39.8% for the circumferential compression and shear stress, respectively.

By applying the non-linearity and imperfection the difference between the eigenmodes could be different and therefore five different eigenmodes which do not have the same buckling behaviour are chosen for further analysis. The eigenmodes that are chosen are Eigenmode 1, 5, 13, 25 and 29. These eigenmodes are the same that are analysed in all of the three load scenarios and all of the eigenmodes are shown in Appendix D.

4.2 GNA and GNIA

The result of a geometrically non-linear analysis (GNA) gives the elastic buckling load of the perfect structure including geometrically nonlinearity [EN-3, 2004].

The GNA analysis in each load scenario is expected to reach the critical buckling load at the calculated critical buckling stress obtained from the LBA. i.e. the load proportionality factor (LPF) is going towards 1 which signifies no imperfections are included. The LPF is a factor of the critical buckling stress the structure can tolerate before buckling occurs. When imperfections are applied it is expected that the LPF varies from 0-1. If a test is conducted on a shell structure in an experiment and the structure is assumed to be almost perfect, the result would be closest to the GNA results compared to an GNIA analysis where imperfections are included. Both the GNA and GNIA have been constructed using the modified Riks method to solve the non-linear equations since it has been proven to be the most successful method [Simulia, 2010]. The Riks method is a linearised version of the arc-length method and is illustrated in Figure 4.3. Instead of using a constraint arc surface the iterative change is made orthogonal to the predictor solution shown by the normal plane, n_1 with reference to the tangent, t_i . The method obtains a solution in a space defined by the displacement, p , and a load state, λ_q , where λ is the LPF. Riks method solves the loads and displacements simultaneously which makes it possible to pass any limit load which is the point where the structure experiences snap-through. The iteration stops when the out of balance force vector g_i , becomes sufficiently small. g_i is obtained by the scalar product of the two vectors n_i and t_i found on the stiffness matrix where K_T is the tangential stiffness matrix. Initially, an arc length is defined and thereby, the initial load proportionality factor λ . In Abaqus, the increment size is automatically selected by an incrementation algorithm.

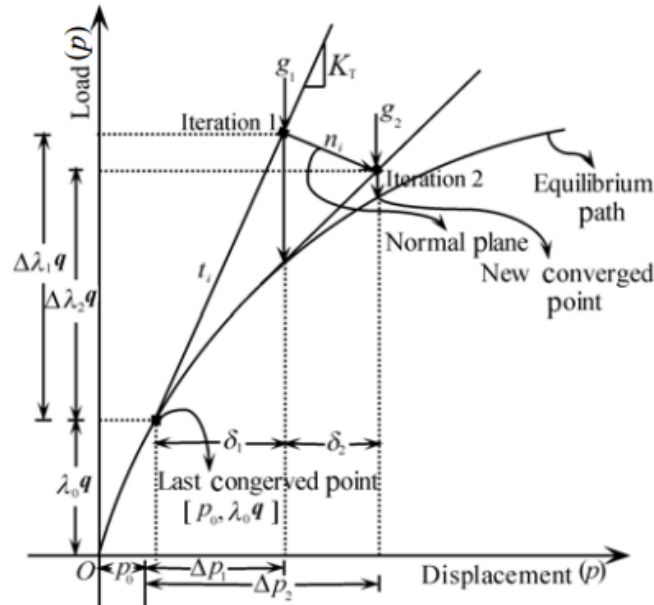


Figure 4.3: Riks iteration scheme [Bashir-Ahmed, 2003].

GNIA are similar to the GNA but with imperfections included. The scale factor is used to implement the degree of the imperfection. The scaling factor is scaled relative to the thickness of the model, which is 1 mm, for the cylindrical shell structure. E.g. if the scaling factor is set to 10, the scaling is 10 times the thickness. The degree of the imperfection is of great importance and therefore a plot is made for each of the load scenarios with different degree of imperfection which is created by varying the scaling factor. When the stress is plotted as a function of the displacement the point at which buckling occurs is observed. Buckling occurs at the point where the curve make a notable deviation in the path. The buckling stress is plotted as a function of the axial displacement since in all of the load scenarios an axial displacement is occurring. In order to implement the imperfection into the models using Abaqus each model has to run two separate steps where the first step is the previously used linear perturbation buckling step with the purpose of creating the buckling from an initial perfect state. The first buckling mode of the model is implemented and the next step is the imperfection step where it uses Riks method to start from the already deformed state. In order to verify that the step begins from the already deformed model the initial state of Riks method step shows that the model is already deformed which is illustrated in Figure 4.4. The model is expected to be very sensitive to the imperfection and thus these initial states are scaled down where the scaling factor is, as earlier mentioned, a scaling factor relative to the thickness.

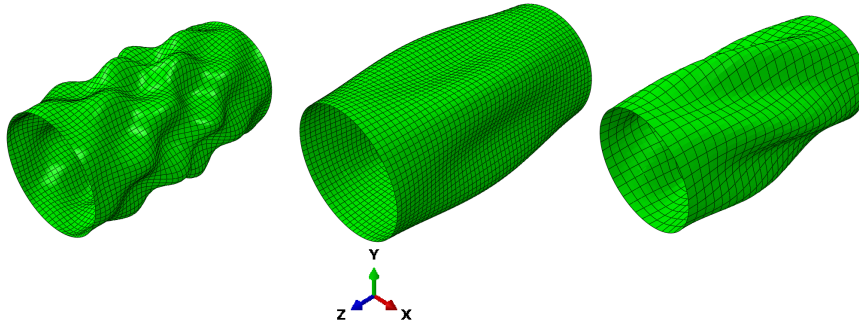


Figure 4.4: Initial state of Riks Method step, from left to right it shows the structure exposed by meridional compression, circumferential compression and shear stress.

The plots for the different load scenarios with varying scaling factors relative to the thickness of the imperfection are illustrated in Figures 4.5 - 4.7. For all the plots a LPF is obtained which are multiplied with the critical buckling stress that is obtained in the LBA. This stress is plotted as a function of the axial displacement in all of the plots. A specific node is followed from the initial state to the final state where the model has buckled and thus the axial displacement is obtained. For a meridional compression the axial displacement is expected to be the largest displacement in any of the directions since the loads are acting in the same direction. The models exposed by circumferential compression and shear stress also experiences some axial compression but because the loads are not acting in the axial direction they wont experience the largest displacement in this direction. The purpose of these plots is to see at what stress these imperfect models buckles which they do when the stress drops significantly. There is a dashed black horizontal line in every plot which represents the critical buckling stress for each load scenario with no imperfections which is obtained from the LBA. Thus, it is expected that the results of the GNA in all of the plots should buckle at that limit since the GNA is made for a perfect model. All results are enclosed on Appendix CD *Circular Cylinder/Imperfections*.

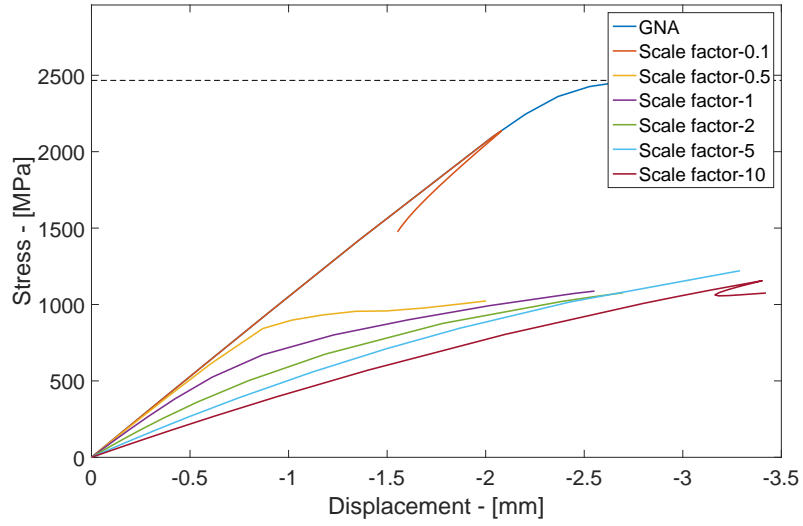


Figure 4.5: GNA and GNIA analysis of critical buckling stress of meridional compression as a function of the axial displacement.

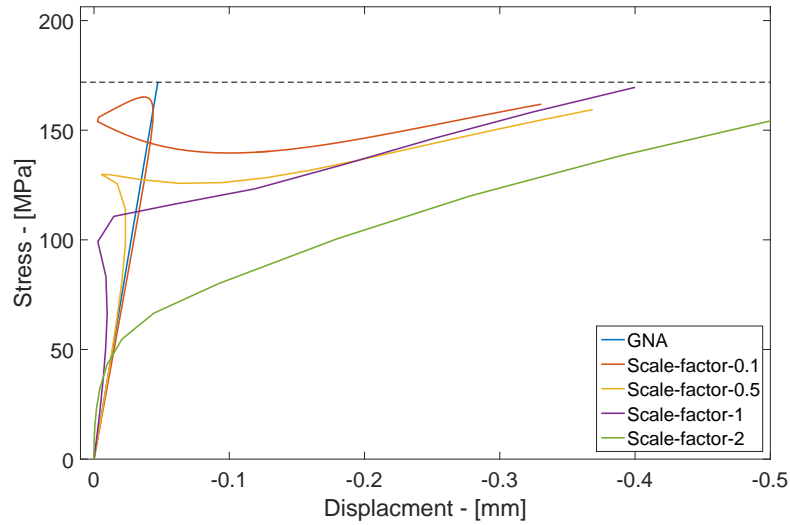


Figure 4.6: GNA and GNIA analysis of critical buckling stress of circumferential compression as a function of the axial displacement.

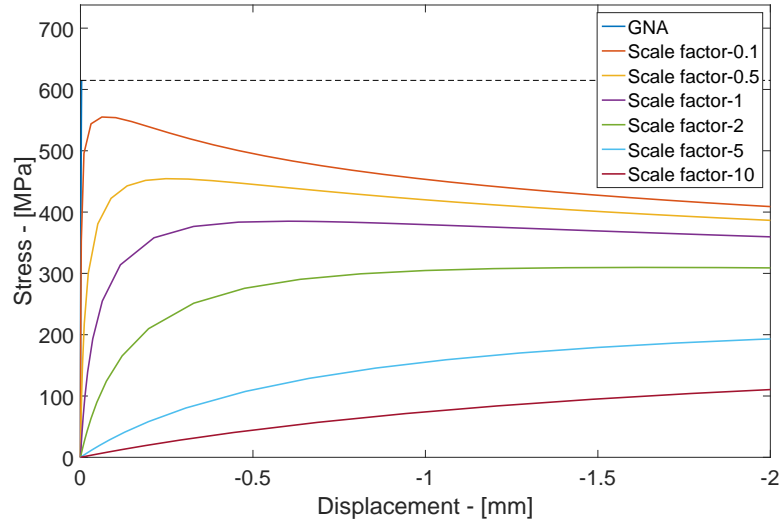


Figure 4.7: GNA and GNIA analysis of critical buckling stress of shear stress as a function of the axial displacement.

How the shell structure behaves in the different load scenarios is clearly different. Independent on how the structure is exposed to a load the structure is very sensitive for imperfections. The structure behaves different dependent on which type of loading it is exposed to. The same scaling factors are used to analyse the sensitivity for each different load scenario. The scaling factor higher than 2 for the circumferential compression could not be done which suggest that the imperfection scaling factor is too high, and by looking at Figures 4.5 and 4.7 the scaling factor of 5 and 10 results in very low stresses before buckling occurs and may be the reason why the model could not be performed for the circumferential compression for a scaling factor of 5 and 10. In all the plots it is seen that with an increasing imperfection buckling occurs at lower stresses. For the lower scaling factors the transition from pre-buckling to post-buckling is very dramatic i.e it is dropping rapidly in buckling stress, and as the scaling factor is increased the transition is less dramatic i.e it does not drop as rapidly. In Figure 4.6 it is observed that when the model begins to buckle it drops significant in the critical buckling stress, but at a certain point it surpasses the critical buckling stress at the point when buckling occurred.

The next step is to analyse what effect the scaling factors has on the different eigenmodes and as mentioned previously the chosen eigenmodes are 1, 5, 13, 25 and 29. The scaling factor that is used to model the different eigenmodes is different from one load scenario to another due to the different sensitivity of the imperfection. For all of the models the scaling factor of 1 relative to the thickness is used. For all of these models the stress at which buckling occurs is used to analyse if there is a tendency from a low eigenmode to a high eigenmode. A bar plot is made for each of the load scenarios where the LPF

for each case is multiplied to the critical buckling stress obtained from the perfect mode which are $\sigma_{z_{cr}} = 2466.5 \text{ MPa}$, $\sigma_{\theta_{cr}} = 171.9 \text{ MPa}$ and $\tau_{\theta_{cr}} = 614.8 \text{ MPa}$ for meridional compression, circumferential compression and shear stress, respectively. The bar plots are illustrated in Figures 4.8 - 4.10. All results are enclosed on Appendix CD *Circular Cylinder/Imperfections*.

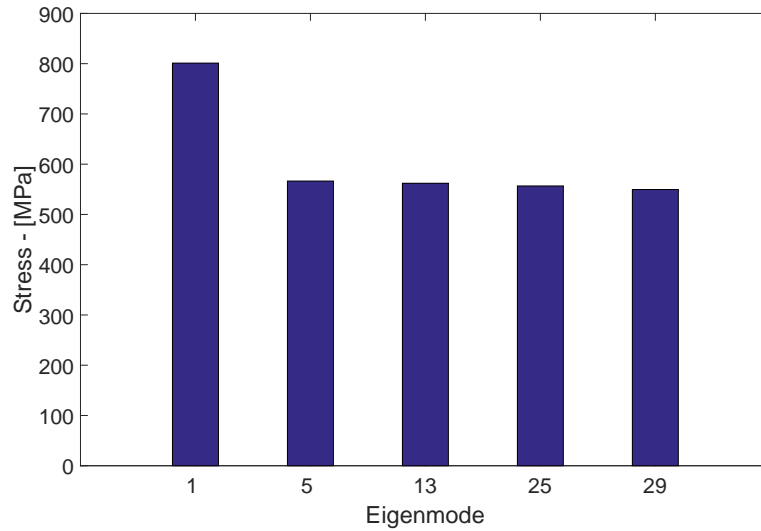


Figure 4.8: Critical buckling stress for different eigenmodes for meridional compression.

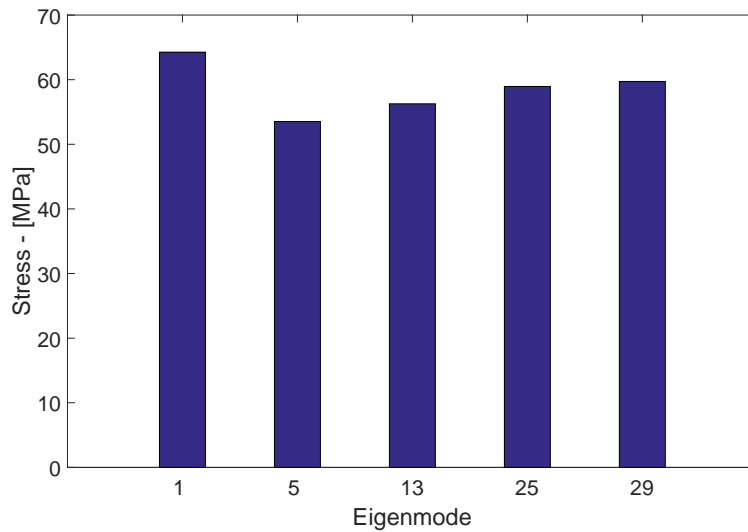


Figure 4.9: Critical buckling stress for different eigenmodes for circumferential compression.

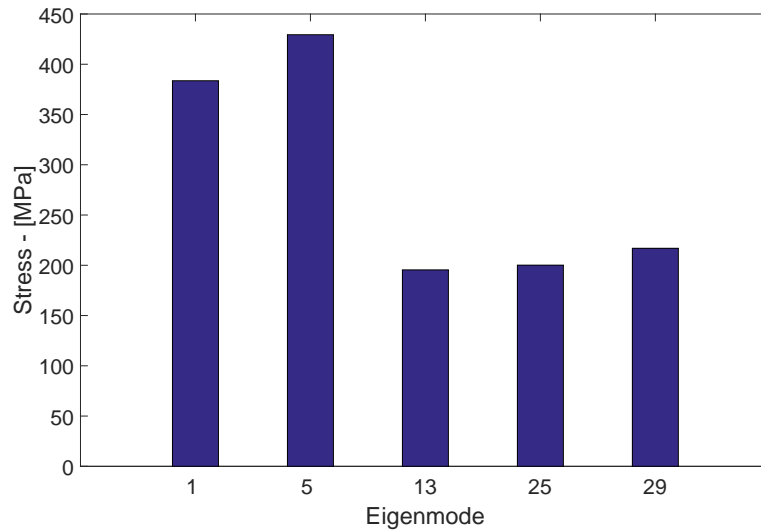


Figure 4.10: Critical buckling stress for different eigenmodes for shear stress.

From the figures it is seen that there is a tendency in all of the bar plots which shows that for a higher eigenmode the structure is more sensitive to imperfection since the buckling occurs at a lower stress i.e. as the eigenmodes increases the buckling occurs at a much lower stress as is expected. In Figures 4.8 and 4.10 the tendency is that after the first buckling mode the critical buckling stress is dropping rapidly with an increasing buckling mode i.e. a higher imperfection. In Figure 4.9 it is observed that after the 1st buckling mode the critical buckling is dropping but afterwards it is increasing for every higher buckling mode, which also is observed with the different scaling factors in Figure 4.6 which confirms that if the imperfection is very high it can eventually surpass the critical buckling stress at the point when buckling occurred.

Now different loads on a cylindrical shell is analysed and different buckling modes are used as initial shape in order to see how the models are affected. Still, the analysis is only for circular cylindrical shells. Therefore, different cross sectional geometries for arch structures are examined in the following chapter in order to see how these different cross sections differs from each other.

Arch Structure

In previous chapters cylindrical shells from EN-3 [2004] with different load scenarios are calculated to see what the buckling stress is for those load scenarios. For all the different load scenarios for the circular cylinder the applied load only gave membrane forces in the cylinder. For an arch it is difficult to apply a load that only causes membrane stresses. The combination of the geometry, the load and support type are of importance when designing an arch. Therefore, different geometries are analysed in order to conclude which geometry is optimal dependent on the support type and the applied load.

Even though a geometry is optimal regarding a linear elastic calculation when considering section forces it might not be the optimal geometry when considering buckling. In a linear static analysis a circular geometry is optimal when exposed to inside suction and a catenary geometry is optimal when exposed to self weight. Even though it is expected that these geometries perform well in a linear static analysis it might not be the same case when considering instability and therefore the results for a buckling analysis might be different. Furthermore, since the loads acts differently on the structure the supports have an influence on the result as well. This indicates that different boundary conditions are optimal for the different geometries.

After examining the difference in the geometry for different loads the influence of imperfections in the geometry and load are analysed. First, imperfections in the applied load are analysed. Afterwards, imperfections consisting of dimples and perturbation loads are analysed to see what influence these have on the results.

5.1 Models

The geometries for the cross section of the shell structure that are examined are a circular, parabolic and catenary as seen in Figure 5.1. Different load scenarios are applied to each cross section in order to see which cross section is best at absorbing the different loads. The loads are self weight, inside suction and a single point load on top of the cross section as seen in Figures 5.2 and 5.3. Furthermore, all geometries are applied different load combinations to see how they absorb the loads when they are applied simultaneously.

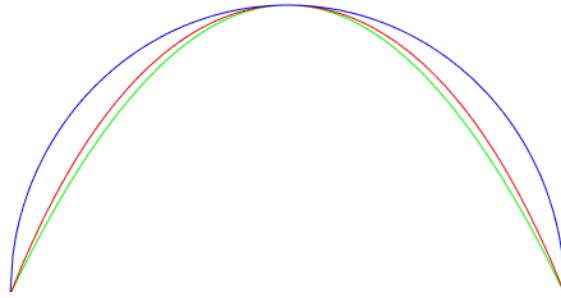


Figure 5.1: Different cross section for the shell. Blue: circular, red: catenary, green: parabolic.

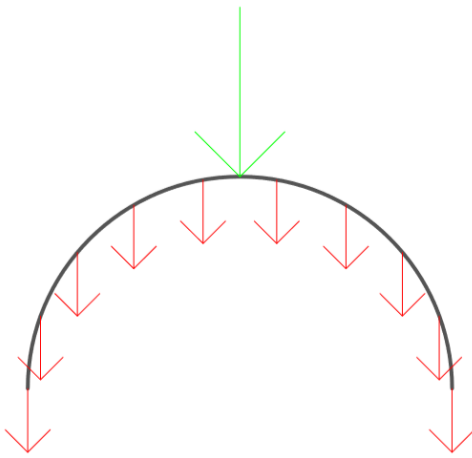


Figure 5.2: Arch with self weight (red) and line load (green).

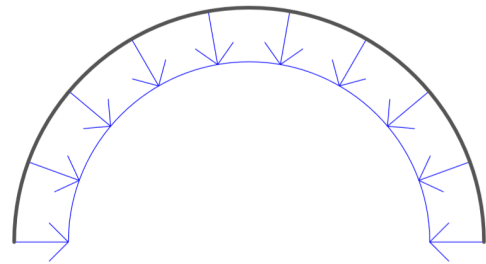


Figure 5.3: Arch with inside suction (blue).

To ensure that the different shapes are comparable there are three common points for the circle, parabolic and catenary as seen in Figure 5.1. In order to obtain these three common points the following equations for the three shapes are used:

$$y_{\text{circular}} = \sqrt{R^2 - x^2} \quad (5.1)$$

$$y_{\text{parabolic}} = \frac{R^2 - x^2}{R} \quad (5.2)$$

$$y_{\text{catenary}} = a - a \cosh\left(\frac{x}{a}\right) + R \quad (5.3)$$

These equations are used to create the points that make the characteristic arc for each shape that is imported to Abaqus. The three arcs are determined so they fit a semicircle with the radius $R = 5$. The constant, a , in Equation (5.3) is 3.09379614 and is determined by iteration and ensures that the catenary is crossing the same points as the circle and the parabolic with a precision of nine decimals. The results are enclosed on Appendix CD *Arch/Points for arc*.

All the models in this chapter are calculated with the finite element software Abaqus and all models are simple supported as shown in Figure 5.4 unless anything else is specified.

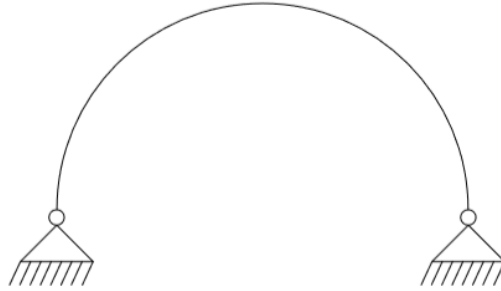


Figure 5.4: Support of the models.

The relations between the dimensions for the arches are the same as those given in Chapter 3, which means that the length is twice the diameter and the thickness is 1% of the diameter. The only difference is that the diameter is changed to 10 m. This does not change the results as long as the ratios between the length, thickness and diameter are the same as confirmed in that chapter.

5.2 Finite Element Model

The procedure for making the finite element model in Abaqus is the same as described in Section 2.2 and therefore only the things different from that procedure are described.

First, the circular geometry is analysed. In Abaqus a circular geometry can be made directly in the software but since the parabolic and catenary shape can not be made explicit these geometries are created from a set of linear lines. Since the results may vary from a perfect cross sectional geometry and the geometry created from a set of straight lines the circular arch is also created from a set of straight lines. This is done in order to make sure that the results between the three cross sectional geometries are due to the shape and not due to the fact that the circular geometry is perfect when the parabolic and catenary are created from a set of straight lines. In order to implement the circular, parabolic and catenary shape to Abaqus a set of coordinates are created using Equations (5.1) - (5.3). Furthermore, a study of the difference in using a constant arc length and a constant straight line is performed in order to see how this influence the results. The coordinates are enclosed on Appendix CD *Arch/Points for arc*. From this study, the x-coordinates are calculated and a straight line between the coordinates are imported into Abaqus and then extruded to create the 3-dimensional models as seen in Figures 5.5 - 5.7. Each model is created with a cross section consisting of 200 straight lines in order to ensure that the difference between the different arches are due to the shape and not to errors due to a low number of elements.

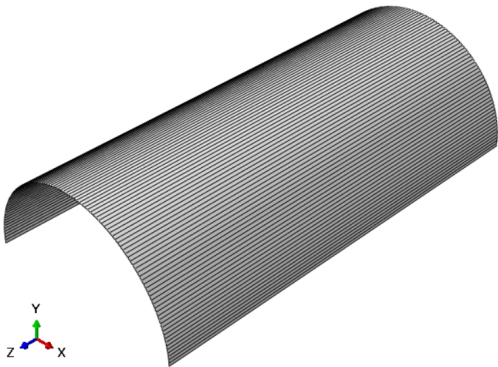


Figure 5.5: Circular shell in Abaqus.

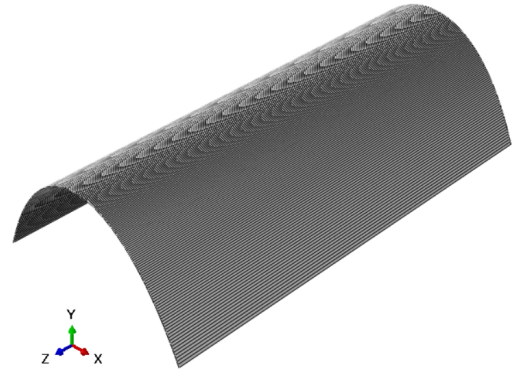


Figure 5.6: Catenary shell in Abaqus.

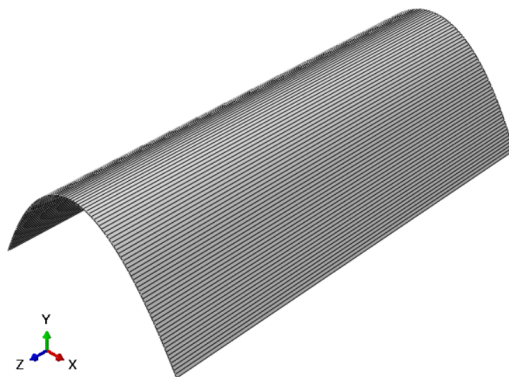


Figure 5.7: Parabolic shell in Abaqus.

5.2.1 Assembly

Each element of the shell is defined individually and in order for them to work as one unit the interaction between each element is set to frictionless. An interaction between two elements are marked in Figure 5.8.

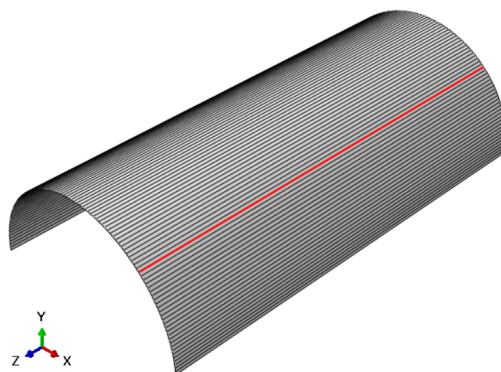


Figure 5.8: Interaction of two elements.

5.2.2 Loads

The loads applied in the different models in Abaqus are shown in Figures 5.9 - 5.11. The inside suction is applied as a pressure load acting on the inside area of the shell and the self weight is applied as a body force on each element of the shell. The load on top of the arch is applied by creating a stringer between the two top elements cf. Figure 5.12 that is working as a beam. Then, a line load is applied on the stringer working upon the length of the shell.

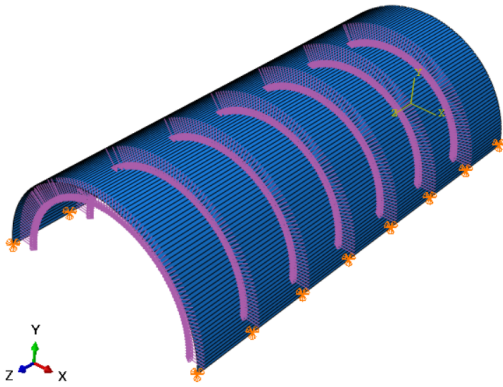


Figure 5.9: Suction inside the arc.

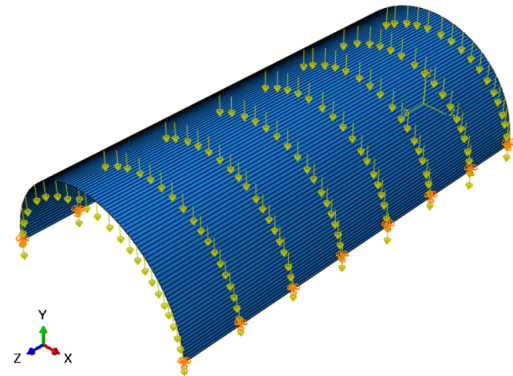


Figure 5.10: Self weight of the arc.

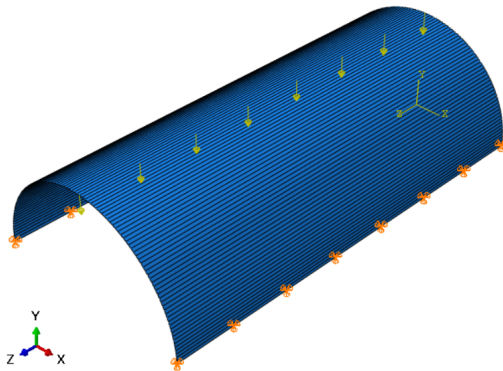


Figure 5.11: Line load acting on top of the arc.

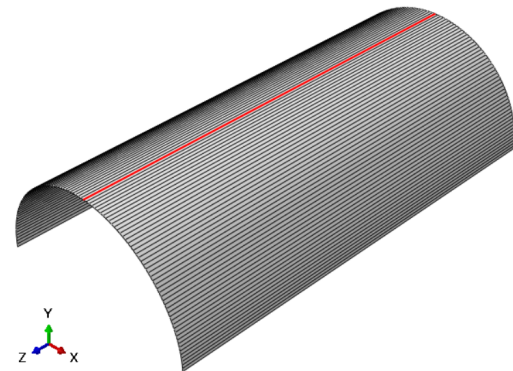


Figure 5.12: Stringer between two elements.

The load inputs for the different load scenarios are shown in Table 5.1. Here L_{Arc} is the length of the cross section of the circular arc, L_{Cylinder} is the length of the cylinder and t is the thickness of the shell. By having these load inputs the total sum of each load is 1.

Table 5.1: Load inputs in Abaqus.

Load	Input
Inside suction	$1 \text{ N}/(L_{\text{Arc}} \cdot L_{\text{Cylinder}})$
Self weight	$1 \text{ N}/(L_{\text{Arc}} \cdot L_{\text{Cylinder}} \cdot t)$
Line load	$1 \text{ N}/L_{\text{Cylinder}}$

5.2.3 Mesh

Since there are three different cross sectional geometries which each has three different load scenarios and a combination of those a lot of models are created. In order to minimize the amount of computational time that is required when making a convergence analysis, only a convergence analysis is done for the circular cross section, and all the remaining models are created with the same mesh. From Appendix E.1 it is seen that a mesh with 38 550 d.o.f. and 804 elements are chosen for the buckling analysis. For a linear static analysis a mesh with 724 806 d.o.f is chosen cf. Appendix E.2.

5.2.4 Inputs in the Model

All the input parameters are shown in Table 5.2. The elasticity of the stringer is chosen to be a factor 10^9 lower than the elasticity of the shell in order to make sure the stiffness of the stringer does not affect the results. Furthermore, the cross sectional dimensions of the stringer are chosen to be small as well.

Table 5.2: Input parameters in Abaqus.

Shell properties	Symbol	Value
Model type	Shell, homogeneous	
Elasticity modulus	E	210 000 MPa
D.o.f., Buckling		38 550
Elements, Buckling		804
D.o.f., Linear static analysis		724 806
Elements, Linear static analysis		40 200
Shell thickness	t	0.1 m
Length	L	20 m
Poisson's ratio	ν	0.3
Stringer properties	Symbol	Value
Stringer type	Beam	
Dimensions, Stringer	$a \times b \times L$	0.01 m \times 0.01 m \times 20 m
Elasticity modulus, Stringer	E	0.000 21 MPa
Shear modulus, Stringer	G	0.000 08 MPa

5.3 Results for Linear Static Analysis

As mentioned earlier the different loads and support types are important for choosing the optimal geometry. Furthermore, the optimal geometry in a linear static analysis depends on the applied load. Therefore, a static analysis is performed in order to see how this is seen in the section moment in the arch.

With the boundary conditions mentioned earlier with two simple supports the advantage of the circular shell with inside suction is not utilised to its full potential since it is not able to compress as shown in Figure 5.13. This is the advantage of the circular shell since it is symmetrical with the same tangential inclination everywhere on the circle. Therefore, a model with the supports as shown in Figure 5.14 is analysed as well to see how it affects the results.

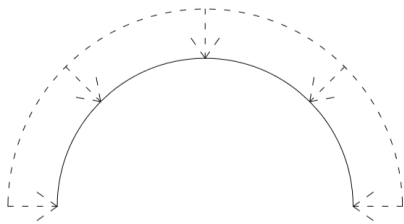


Figure 5.13: Compressed circular shell.

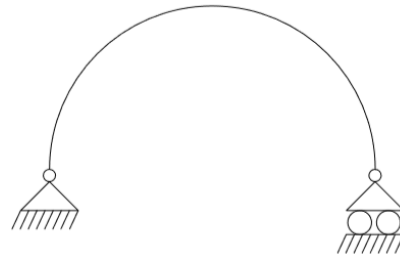


Figure 5.14: Model with a roller support.

All the results for the section moment are shown in Table 5.3 and the orientation of the local coordinate system is shown in Figure 5.15. This means that the local second axis is parallel to the global z-axis and the local first axis is orthogonal to this and follows the arc of the figure.

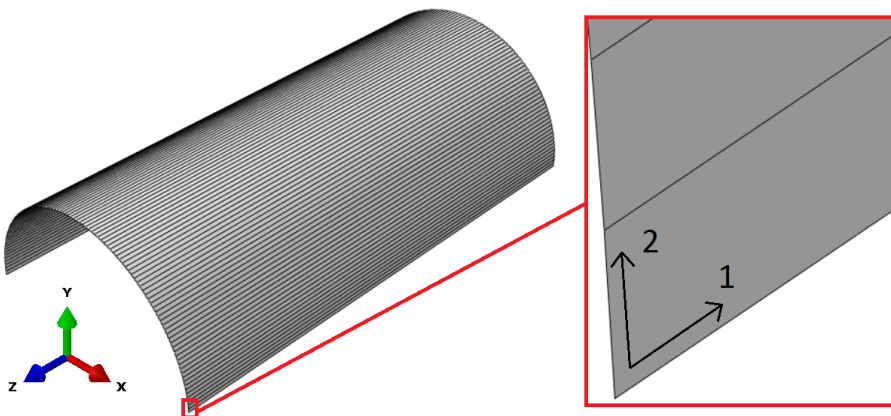


Figure 5.15: Global and local coordinate system orientation for the individual elements.

Table 5.3: Section moments for the three different cross sectional geometries and three different loads. All units in Nm.

	Section moment			
	M_1		M_2	
Circular	Max	Min	Max	Min
- Suction	$1.0 \cdot 10^{-4}$	$-3.6 \cdot 10^{-5}$	$2.5 \cdot 10^{-5}$	$-1.2 \cdot 10^{-5}$
- Self weight	$7.4 \cdot 10^{-2}$	$-5.7 \cdot 10^{-2}$	$2.3 \cdot 10^{-2}$	$-1.8 \cdot 10^{-2}$
- Line load	$2.3 \cdot 10^{-2}$	$-4.6 \cdot 10^{-2}$	$7.2 \cdot 10^{-3}$	$-1.4 \cdot 10^{-2}$
Circular - Roller support	Max	Min	Max	Min
- Suction	$1.0 \cdot 10^{-4}$	$-6.5 \cdot 10^{-5}$	$2.5 \cdot 10^{-5}$	$-1.3 \cdot 10^{-5}$
- Self weight	$3.2 \cdot 10^{-5}$	$-4.6 \cdot 10^{-2}$	$1.5 \cdot 10^{-4}$	$-1.4 \cdot 10^{-2}$
- Line load	$1.0 \cdot 10^{-5}$	$-1.3 \cdot 10^{-1}$	$1.1 \cdot 10^{-3}$	$-3.9 \cdot 10^{-2}$
Parabolic	Max	Min	Max	Min
- Suction	$6.8 \cdot 10^{-3}$	$-7.0 \cdot 10^{-3}$	$2.0 \cdot 10^{-3}$	$-2.2 \cdot 10^{-3}$
- Self weight	$1.6 \cdot 10^{-2}$	$-1.7 \cdot 10^{-2}$	$4.7 \cdot 10^{-3}$	$-5.3 \cdot 10^{-3}$
- Line load	$3.0 \cdot 10^{-2}$	$-1.1 \cdot 10^{-2}$	$9.2 \cdot 10^{-3}$	$-3.4 \cdot 10^{-3}$
Parabolic - Roller support	Max	Min	Max	Min
- Suction	$1.0 \cdot 10^{-2}$	$-1.3 \cdot 10^{-4}$	$3.1 \cdot 10^{-3}$	$-3.6 \cdot 10^{-4}$
- Self weight	$5.1 \cdot 10^{-2}$	$-4.4 \cdot 10^{-5}$	$1.6 \cdot 10^{-2}$	$-6.6 \cdot 10^{-4}$
- Line load	$1.3 \cdot 10^{-1}$	$-4.9 \cdot 10^{-5}$	$3.9 \cdot 10^{-2}$	$-1.2 \cdot 10^{-3}$
Catenary	Max	Min	Max	Min
- Suction	$5.6 \cdot 10^{-3}$	$-5.3 \cdot 10^{-3}$	$1.7 \cdot 10^{-3}$	$-1.6 \cdot 10^{-3}$
- Self weight	$2.6 \cdot 10^{-4}$	$-5.9 \cdot 10^{-4}$	$8.9 \cdot 10^{-5}$	$-1.8 \cdot 10^{-4}$
- Line load	$3.4 \cdot 10^{-2}$	$-1.4 \cdot 10^{-2}$	$1.0 \cdot 10^{-2}$	$-4.2 \cdot 10^{-3}$
Catenary - Roller support	Max	Min	Max	Min
- Suction	$8.1 \cdot 10^{-3}$	$-7.4 \cdot 10^{-5}$	$2.5 \cdot 10^{-3}$	$-3.3 \cdot 10^{-4}$
- Self weight	$5.0 \cdot 10^{-2}$	$-3.5 \cdot 10^{-5}$	$1.6 \cdot 10^{-2}$	$-6.2 \cdot 10^{-4}$
- Line load	$1.3 \cdot 10^{-1}$	$-3.9 \cdot 10^{-5}$	$3.9 \cdot 10^{-2}$	$-1.2 \cdot 10^{-3}$

From Table 5.3 it is seen that the moments around the second local axis is approximately one third to one fourth of the moments around the first local axis. In Figures 5.16 and 5.17 the moment distributions for M_1 and M_2 are shown for a circular geometry with a roller support in one end and a line load acting on the top. From Figure 5.16 it is seen that the moment is 0 at the supports and increase continuous up along the arch and is maximum at the top of the arch. From Figure 5.17 the same is observed but the moment on the free edge is 0 as well since the moment, M_2 , is in the cross sectional plane. The same principle applies for the other geometries with other loads acting on the structure.

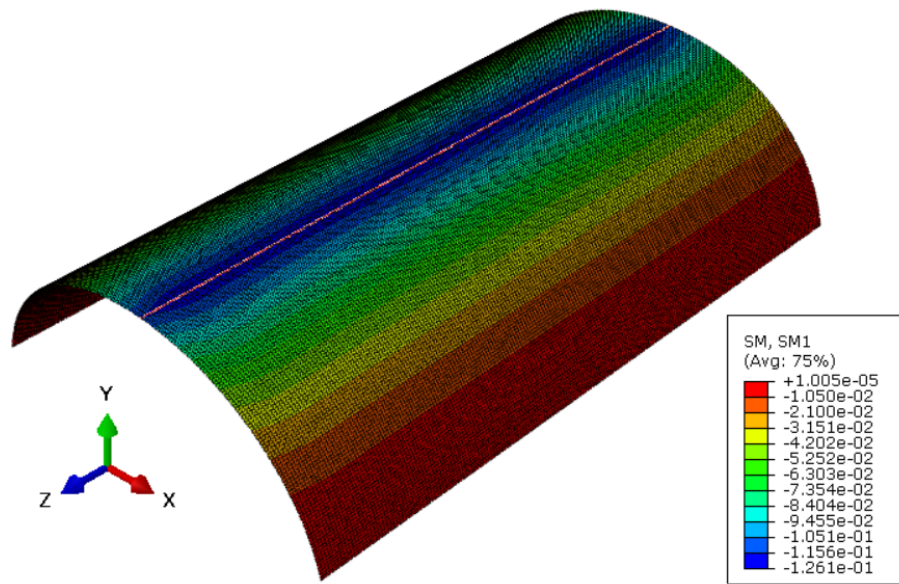


Figure 5.16: Moment distribution of M_1 for circular geometry with a roller support and a line load on top.

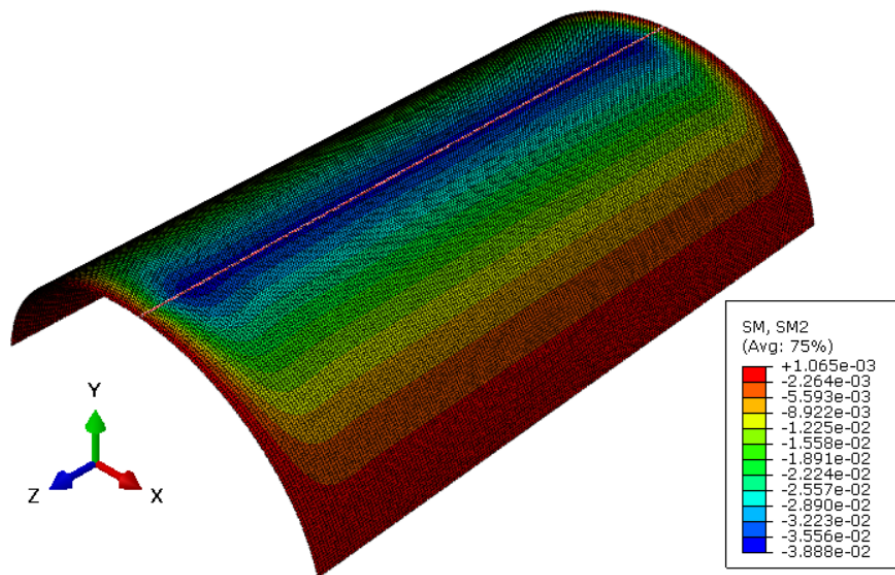


Figure 5.17: Moment distribution of M_2 for circular geometry with a roller support and a line load on top.

The moment distribution for M_1 for a circular geometry with a line load on top and without a roller support is shown in Figure 5.18. Here it is seen that the deformation of the arch is different from the model with a roller support in one end since it is not able to move in one end. Similar observations are done for the other geometries and load scenarios cf. Appendix F.

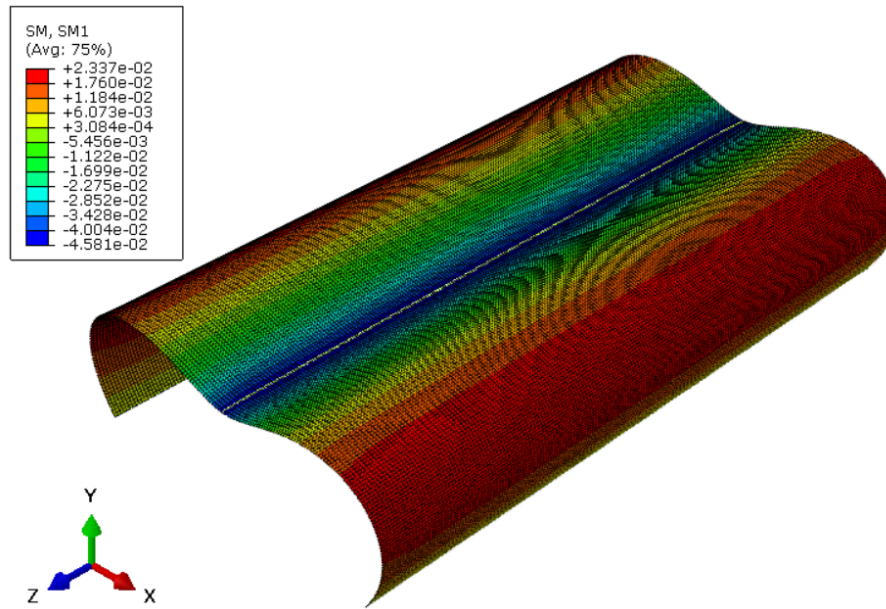


Figure 5.18: Moment distribution of M1 for circular geometry without a roller support and a line load on top.

For suction inside the shell with and without a roller support in one end of the shell, the moments in the shell are lower for the circular geometry than for the catenary and the parabolic. This indicates that the circular geometry is more effectively designed for a suction inside the shell since the moments created in the shell are less than for the other two geometries. Furthermore, since the moment created by inside suction in the catenary geometry is lower than for the parabolic geometry it is concluded that for a shorter cross sectional arch, a higher moment acts in the shell. Therefore, the circular geometry is the optimal geometry if the shell is exposed to an inside suction when considering the moment in the arch. This observation is as expected since the circular geometry with inside suction should transform the load into membrane forces better than the two other geometries.

For the self weight of the arch it is seen that without the roller support that the moment in the catenary geometry is lower than the moment in the circular and the parabolic geometry. This indicates that for self weight of the arch the catenary geometry is a better design than the circular and the parabolic geometry. This is as expected as well since the catenary geometry should transform the loads into membrane forces better than the circular and parabolic geometries. Though, it is not the case for the self weight with roller support since the order of magnitude for the moments are the same for all three geometries. Therefore, the catenary geometry is only good when it cannot move in any of the supports.

Regarding the line load on top of the arch the absolute moment is in the same order of magnitude for all three geometries for each support type. This means that none of the geometries performs considerably better than the others. This is as expected since none of

the geometries are the perfect geometry for this load type as discussed earlier.

It is also noticed that the moment for the circular geometry with a roller support in one end and exposed to inside suction is approximately a factor 100 less than the parabolic and catenary geometry. This value is close to 0, which is as expected since the optimal geometry for a structure exposed to inside suction is a sphere. Since the structure is not a sphere but a circular geometry that is extracted it is expected that the moments should be close to 0 but not exactly 0. Likewise, the moment for the catenary exposed to self weight without any roller support is approximately a factor 100 less than for the circular and parabolic geometry. The perfect geometry for a structure exposed to only its self weight is a dome created from a catenary that is rotated around an axis of symmetry. The order of magnitude of the moment for the line load on top of the arch is the same for the different geometries independent of the support. It is also noticed that the order of magnitude is not as close to 0 as the catenary geometry with self weight or the circular geometry with inside suction. This is as expected since none of the geometries is the optimal for this load type as discussed earlier. The optimal design is two straight lines which is free to rotate in the join. For a single point load the optimal structure would be a cone.

From this analysis it is concluded that the support has a significant influence on the results when considering the linear static analysis. Overall, the linear static analysis is used to calculate the section moments assuming they lead to higher stresses in the outermost fibres. When considering material yielding, this is a natural approach. The results corresponds with the expectations for the different loads and geometries for the linear static analysis and in the following section it is analysed if the buckling analysis gives the same observations. In case of instability, the applied load might not lead to instability due to moments but due to membrane forces. This means that smaller membrane forces in the structure lead to smaller risk of instability.

5.4 Results for Buckling Analysis

The optimal geometry for the different load scenarios when considering instability might differ from the optimal geometry when considering a linear static analysis. Therefore, all the results from a buckling analysis are shown in this section and compared with the obtained results from the linear static analysis.

5.4.1 Circular Arch

The results for the circular cross section are shown in this section. For a circular geometry it does not matter whether the same arc length is chosen to determine the coordinates or the same straight line is chosen since a circle has the same tangential slope everywhere on the arc. Therefore, only one model with straight lines is analysed. Even though, the

circle is created with a set of straight lines in order to compare it with the parabolic and catenary shape a model created with a semicircle in Abaqus is also analysed in order to compare the results and see if there is a difference between the two models.

The first buckling mode is shown in Figure 5.19 for the shell created in Abaqus with a circular cross section and with inside suction. From this analysis the eigenvalue and the first buckling mode is obtained.

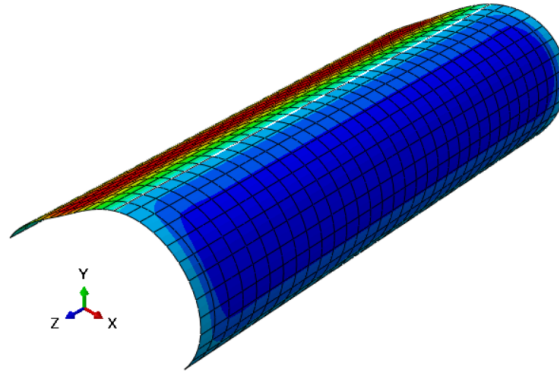


Figure 5.19: Buckling mode 1 of model with circular geometry created in Abaqus with inside suction.

All the results for the circle made in Abaqus as well as the circle created from a set of straight lines are shown in Table 5.4.

Table 5.4: Abaqus results for a perfect circle in Abaqus and a circle created by a set of straight lines.

	Eigenvalue (buckle)
Circular (Made in Abaqus)	
- Suction	144.20
- Self weight	129.08
- Lineload	100.16
Circular	
- Suction	144.21
- Self weight	129.09
- Line load	100.14

From Table 5.4 it is seen that the results are almost the same which indicates that the error in using a set of straight lines instead of a perfect geometry is neglectable. It is also noticed that the circular geometry has a higher eigenvalue for inside suction.

5.4.2 Parabolic Arch

The results for the parabolic cross section are shown in this section. For the parabolic cross section a study of the points for using the same arc length and the same length of the straight lines are performed. The analytical expressions to calculate the arc length and straight line length are given in Appendix G. The deviation between the coordinates for the same straight line and the same arc length as a function of the number of elements is shown in Figure 5.20.

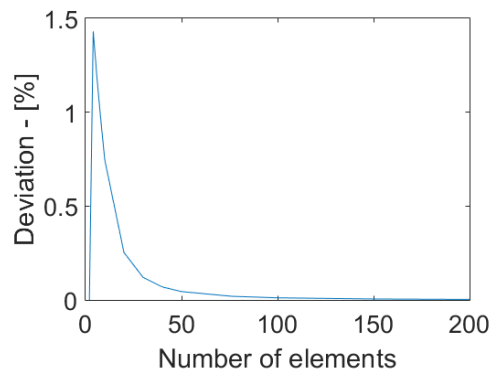


Figure 5.20: Deviation between the coordinates for the chosen methods to create the points as a function of the number of elements.

From Figure 5.20 it is seen that for an increasing number of elements in the cross section the deviation between the two methods to determine the coordinates which defines the straight lines are decreasing. It is also noticed that for only two elements the deviation is 0% since it creates the same two straight lines. The largest deviation between the coordinates for the chosen number of elements of 200 is 0.003% and all the calculations are enclosed on Appendix CD *Arch/Points for arcs*. Since the deviation between the results of the coordinates is small it is concluded that for a large number of elements the influence of choosing the same arc length or the same length of the straight lines is neglectable. Therefore, it is not necessary to determine the more complicated expression for the same arc length analytically if the number of elements is high. The results for the parabolic cross section with the same straight lines are shown in Table 5.5. It is seen that the eigenvalue for the catenary is higher for inside suction as it was seen for the circular geometry.

Table 5.5: Abaqus results for the parabolic cross section.

Load scenario	Eigenvalue (buckle)
Suction	191.36
Self weight	168.73
Line load	106.00

5.4.3 Catenary Arch

The results for the catenary cross section are shown in this section. The analysis with the parabolic cross section showed that the results with the same straight line are accurate since the number of elements is high. Therefore, only a model with coordinates found by the same straight line is created. The results for the catenary cross section are shown in Table 5.6. It is also seen that for the catenary geometry the eigenvalue for inside suction is higher than for the two other load scenarios.

Table 5.6: Abaqus results for the catenary cross section.

Load scenario	Eigenvalue (buckle)
Suction	177.98
Self weight	159.07
Line load	104.52

5.4.4 Comparison of Results

All the results for all the load scenarios acting on the three different cross sectional geometries are shown in Table 5.7.

Table 5.7: Abaqus results for the three different cross sectional geometries.

Load scenario	Eigenvalue (buckle)		
	Circular	Parabolic	Catenary
Suction	144.21	191.36	177.98
Self weight	129.09	168.73	159.07
Line load	100.14	106.00	104.52

From Table 5.7 it is seen that for suction inside the shell the eigenvalue is lower for the circular geometry than for the catenary and highest for the parabolic. This indicates that the circular geometry buckles at a lower load than the two other geometries. This is different from the results obtained in the linear static analysis.

For the self weight of the shell it is seen that the eigenvalue for the parabolic is higher than the catenary and the circle. The results for the parabolic and catenary is closer to each other compared to the result for the circle which is as expected since the shape of the catenary and parabolic is more similar than the shape of the circle cf. Figure 5.1. Though, this is different from the static analysis as well where the catenary performed better when exposed to self weight.

When a load is acting on top of the shell along the length the eigenvalue in the shell is highest for a parabolic which indicates that this geometry is optimal for this load type when considering buckling. It is also seen that the eigenvalue decreases when the arc expands towards the circular geometry since the eigenvalue in the catenary is higher than the parabolic and even higher for the circular geometry.

Overall, the parabolic geometry performs best independent on the applied load in a buckling analysis when it is simple supported. As it is seen from the linear static analysis the support types are of great importance for the model. Therefore, a buckling analysis for different support types are performed in order to see how the support affect the buckling analysis.

5.4.5 Analysis of Different Support Types

The four support types that are analysed are shown in Figure 5.21. These are simple supports with and without a roller and fixed supports with and without a roller. This way the influences of the rollers and the rotation in the support are analysed.

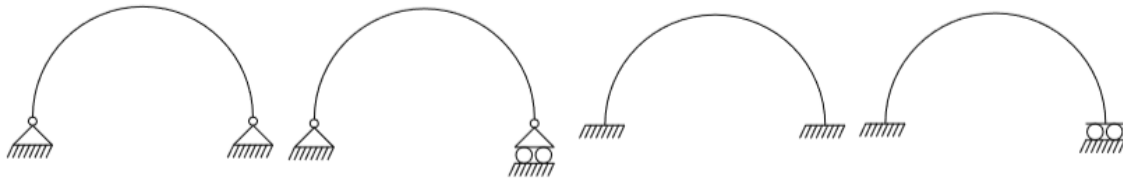
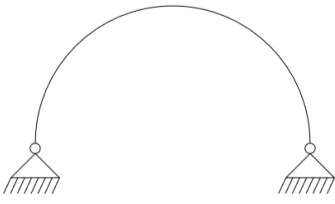
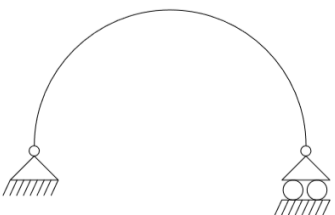
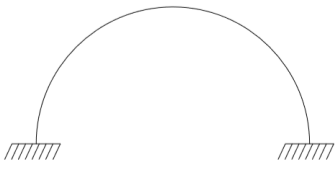
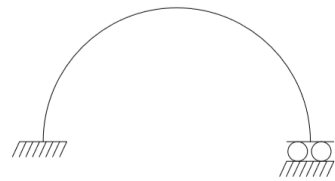


Figure 5.21: Different support types that are analysed.

In order to compare the results two different analysis are performed. First a buckling analysis is performed in order to see which geometry and support that are optimal for the three different load scenarios when considering buckling. Afterwards, a linear static analysis is performed in order to calculate the stresses at the corresponding buckling load. This way it is concluded whether the model buckles or yields first for the different supports and loads. At last, a static analysis with plastic material is performed in order to allow the arch to yield until it collapse. This way the load at buckling is comparable with the load at yielding and the plastic collapse load in order to see whether the shell buckles or yields first for the different support types, geometries and load scenarios. All the results for the buckling analysis are shown in Table 5.8.

From the data given in Table 5.8 it is seen that for the simple supports with and without rollers the parabolic geometry has the highest eigenvalue and the circular geometry has the lowest eigenvalue independent of the load that is applied.

Table 5.8: Eigenvalues from a buckling analysis for the different supports, geometries and loads.

Support	Load	Geometry	Eigenvalue
	Suction	Circular	144.21
		Parabolic	191.36
		Catenary	177.98
	Self weight	Circular	129.09
		Parabolic	168.73
		Catenary	159.07
	Line load	Circular	100.14
		Parabolic	106.00
		Catenary	104.52
	Suction	Circular	38.42
		Parabolic	39.86
		Catenary	39.19
	Self weight	Circular	41.65
		Parabolic	50.38
		Catenary	49.98
	Line load	Circular	30.55
		Parabolic	36.27
		Catenary	34.43
	Suction	Circular	384.50
		Parabolic	491.51
		Catenary	461.84
	Self weight	Circular	412.82
		Parabolic	466.75
		Catenary	476.13
	Line load	Circular	225.47
		Parabolic	237.27
		Catenary	236.41
	Suction	Circular	144.27
		Parabolic	162.73
		Catenary	159.00
	Self weight	Circular	312.15
		Parabolic	318.22
		Catenary	326.65
	Line load	Circular	191.11
		Parabolic	176.32
		Catenary	176.15

For two fixed supports the same is observed for suction and the line load. But for the self weight the catenary geometry has the highest eigenvalue, then the parabolic and finally the circular geometry. For a fixed support with a roller the circular geometry has the lowest eigenvalue and the parabolic geometry has the highest when considering suction. For self weight of the structure, the catenary geometry has the highest eigenvalue, and for a line load on top, the circular geometry has the highest eigenvalue.

This does not coincide with the results from the linear static analysis. Furthermore, it is concluded that the parabolic geometry performs well in a buckling analysis compared to the circular and catenary geometry, even though none of the loads are considered optimal for a parabolic shape.

From Table 5.8 it is also noticed that the magnitude of the eigenvalue differs with a factor 10 dependent on the support type. Furthermore, the eigenvalues are lower for the simple support with a roller in one side for all the load scenarios, which indicates that this support type is worse than the other support types when considering buckling alone. The highest eigenvalues are obtained when both boundaries are fixed which means that a higher load can be applied before buckling occurs.

From the results it is seen that the supports have a significant influence on the results regarding buckling and should therefore be considered carefully when constructing a similar shell structure. Earlier it was concluded that the section moments give another picture of the optimal geometry and therefore the stresses are calculated as well. In Table 5.9 the von Mises stress at buckling is shown as well as the chosen yield stress, which is 275 MPa. From Table 5.9 it is seen whether the shell structure has a buckling stress higher or lower than the yielding stress which indicates whether the structure buckles or yields first. From the table it is seen that in most cases the yielding is critical. For the following cases yielding occurs before buckling for all geometries:

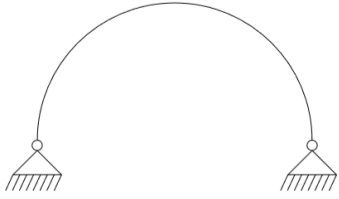
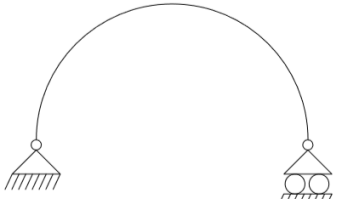
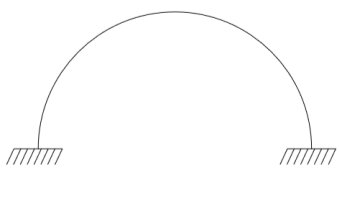
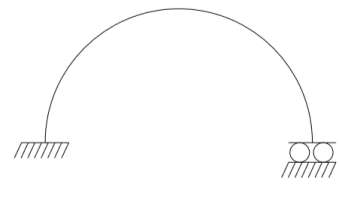
- Simple supports with and without a roller and line load
- Simple supports with a roller and self weight
- Fixed supports with and without a roller and self weight
- Fixed supports with and without a roller and line load

For the following case buckling occurs before yielding for all geometries:

- Simple supports with rollers and inside suction

For all other cases some geometries buckles before yielding and vice versa. It is also noticed that the stresses at which the arch buckles for inside suction is lower for the circular geometry independent of the support type.

Table 5.9: Comparison of stresses at buckling and yielding for the different supports, geometries and loads. All units in MPa.

Support	Load	Geometry	Stress	
			Buckling	Yielding
	Suction	Circular	44.71	275
		Parabolic	873.90	275
		Catenary	677.80	275
	Self weight	Circular	545.30	275
		Parabolic	199.70	275
		Catenary	107.30	275
	Line load	Circular	2718.00	275
		Parabolic	2492.00	275
		Catenary	2336.00	275
	Suction	Circular	11.93	275
		Parabolic	268.70	275
		Catenary	213.80	275
	Self weight	Circular	1050.00	275
		Parabolic	1569.00	275
		Catenary	1582.00	275
	Line load	Circular	2115.00	275
		Parabolic	2970.00	275
		Catenary	2786.00	275
	Suction	Circular	77.88	275
		Parabolic	2194.00	275
		Catenary	1583.00	275
	Self weight	Circular	2027.00	275
		Parabolic	373.90	275
		Catenary	332.30	275
	Line load	Circular	5328.00	275
		Parabolic	5038.00	275
		Catenary	4597.00	275
	Suction	Circular	44.29	275
		Parabolic	574.10	275
		Catenary	446.80	275
	Self weight	Circular	4597.00	275
		Parabolic	5707.00	275
		Catenary	5329.00	275
	Line load	Circular	8403.00	275
		Parabolic	8631.00	275
		Catenary	8396.00	275

In Table 5.10 the loads at which the structure buckles, yields and has a plastic collapse are shown. The plastic collapse load is determined by implementing a plastic material in the models, which allows the material to yield until a total collapse occurs. The optimal geometry for each support and each load scenario is marked in the table with green text. The optimal geometry is given by the geometry which has the highest load before it either yields or buckles.

From this observation it is seen that the circular cross section is the optimal for all support types when exposed to an inside suction except the model with a simple support and a roller support. Though, in this case the applicable load for each geometry is almost the same and the difference is in the third decimal number.

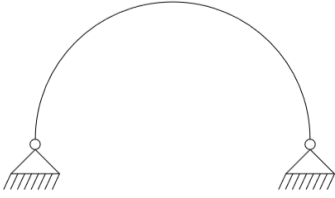
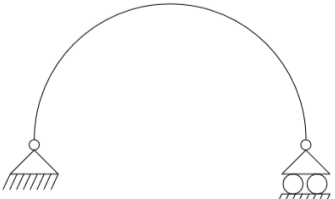
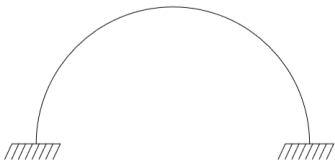
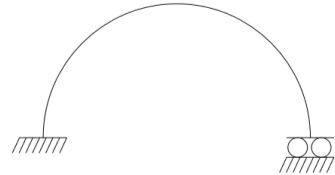
The catenary is the optimal geometry when exposed to a self weight only when the model is fixed supported without a roller. When the system has two simple supports without a roller the parabolic geometry is the optimal. When a roller support is present the circular geometry can resist a higher load before failure occurs.

When a line load is acting on top of the arch the circular geometry is optimal when there is a roller support and the catenary geometry is optimal when there is no roller support.

When considering the buckling and yielding load for the optimal geometry then buckling is critical for all the different supports for inside suction. For a line load on top yielding is critical for all support types. For a self weight yielding is critical for all support types as well except when the model is simple supported without a roller. From this it is concluded that even though failure for shells often are due to buckling a static analysis must be performed as well in order to determine how and whether the arch fails.

It is noticed that in many of the cases the optimal geometry is the geometry with the highest load for plastic collapse. Furthermore, the plastic collapse load is higher for the circular geometry for all the support types when exposed to inside suction. It is also seen that the collapse load is higher for the circular geometry when there is a roller support for all the different loads. For the support types without a roller, the collapse load is higher for the circular geometry when exposed to an inside suction, higher for the catenary geometry when exposed to self weight and higher for the parabolic geometry when exposed to a line load.

Table 5.10: Comparison of loads at buckling, yielding and plastic collapse for the different supports, geometries and loads. Units: suction $[N/m^2]$, self weight $[N/m^3]$, line load $[N/m]$.

Support	Load	Geometry	Load		
			Buckling	Yielding	Plastic collapse
	Suction	Circular	0.459	2.823	5.417
		Parabolic	0.609	0.192	0.370
		Catenary	0.567	0.230	0.458
	Self weight	Circular	4.109	2.072	3.645
		Parabolic	5.371	7.396	14.663
		Catenary	5.063	12.976	39.090
	Line load	Circular	5.007	0.507	1.267
		Parabolic	5.300	0.585	2.178
		Catenary	5.226	0.615	1.876
	Suction	Circular	1.222	28.168	5.491
		Parabolic	1.127	1.153	0.253
		Catenary	1.125	1.447	0.307
	Self weight	Circular	1.326	0.347	0.554
		Parabolic	1.604	0.281	0.504
		Catenary	1.591	0.277	0.501
	Line load	Circular	1.528	0.199	0.318
		Parabolic	1.815	0.168	0.317
		Catenary	1.722	0.170	0.312
	Suction	Circular	1.224	4.322	5.495
		Parabolic	1.565	0.196	0.510
		Catenary	1.470	0.255	0.626
	Self weight	Circular	13.141	1.783	5.138
		Parabolic	14.857	10.927	18.274
		Catenary	15.156	12.543	37.435
	Line load	Circular	11.274	0.582	1.545
		Parabolic	11.864	0.648	2.563
		Catenary	11.821	0.707	2.128
	Suction	Circular	0.459	2.850	5.511
		Parabolic	0.518	0.248	0.508
		Catenary	0.506	0.311	0.577
	Self weight	Circular	9.936	0.594	1.103
		Parabolic	10.129	0.488	1.003
		Catenary	10.398	0.537	0.863
	Line load	Circular	9.556	0.313	0.631
		Parabolic	8.816	0.281	0.626
		Catenary	8.808	0.288	0.511

5.4.6 Arch with Combined Loads

As it is done in Chapter 3 for the circular cylinder a factorized buckling criterion is performed in this section. It is seen for the circular cylinder that the factorized load can exceed 1.0 when some of the loads are acting on the cylinder at the same time. Therefore, the same principle is analysed for the arch structure in order to see if some of the loads acts in favour of each other. In order to determine the buckling surface several points are required to create a surface which represents the critical buckling stress for the model. To create these points one or two load cases are locked at a certain factor from 0-1 and the remaining load cases are increased until buckling occurs. In total there are created 25 points to get an indication of how the buckling surface looks with a combination of the different load scenarios. The factor of self weight goes from 0 with a step of 0.25 until it reaches 1.0. For each of those steps there are five points where the factors of the line load and suction varies. These points are illustrated for the model with a circular cross section in Figure 5.22. The figure shows the plane of the inside suction and line load, and the contours indicates the self weight. From the figure it is seen, that the buckling surface is a plane surface that changes linearly in all three dimensions. All results are enclosed on Appendix CD *Arch/Failure surface*.

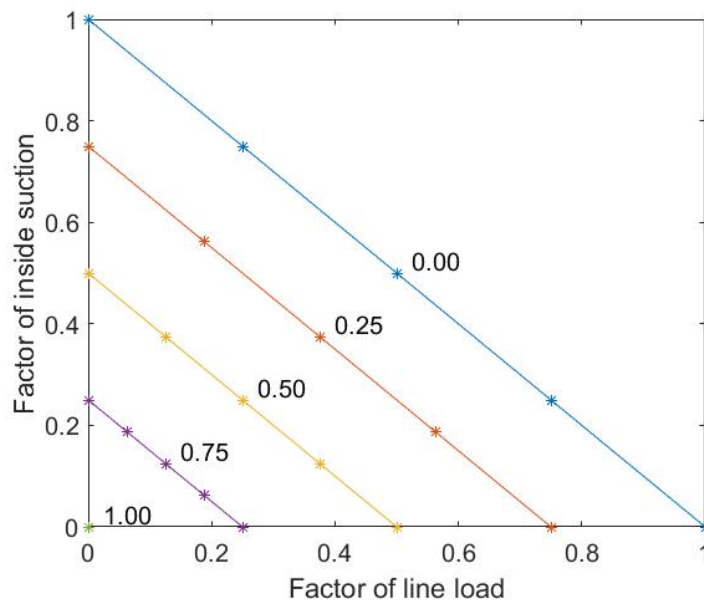


Figure 5.22: Buckling surface for arch with circular cross section.

The points are likewise created for the models with the parabolic and catenary cross section and for all of these models the plot of the factorized loads are identical. This indicates that none of the loads works in favour of each other. As soon as the sum of the factorized loads reach 1.0 the model buckles, which is the case for every point in every model. The

explanation of this is due to the first buckling mode which is illustrated in Figure 5.23 for the different load cases for the model with a circular cross section. The first buckling mode for every geometry with the three different load cases buckles in every case the same way. This explains why none of the loads are working in favour of each other which is the case with the circular cylinder because every load is acting in a different direction.

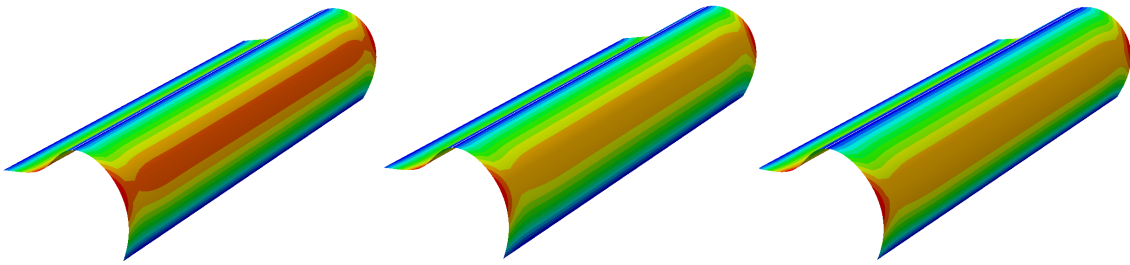


Figure 5.23: First buckling mode for the model with a circular cross section exposed by line load, self weight and suction, respectively.

Since the different load scenarios are not working in favour of each other even though the geometries and load scenarios are different from one another, it is in the following chapter analysed if different types of imperfection works in favour of one of the specific geometries with a specific load scenario. Since there is three different geometries and three different load cases only a few different types of imperfection are analysed.

Imperfections in the Arch

In this section different imperfections are analysed in order to see how they affect the results.

6.1 Imperfections in the Loads

First a study of the line load on top of the arch is analysed in order to see what influence the load orientation has. As seen in Figure 6.1 the load is acting with an angle, α , compared to vertical. The results are shown in Figure 6.2 and it is seen that when the angle is approximately 30° then the circular arch starts to have an advantage since it buckles at a higher load than the catenary and parabolic arc. All results are enclosed on Appendix CD *Arch/Imperfect load*.

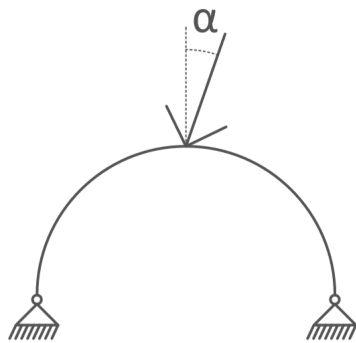


Figure 6.1: Imperfect load orientation for line load.

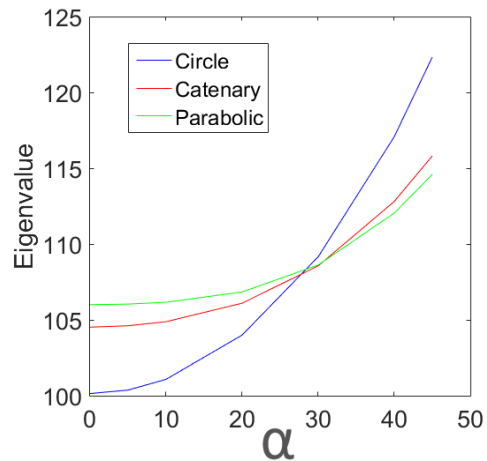


Figure 6.2: Eigenvalue as a function of α .

The same analysis is performed for an imperfection in the self weight as seen in Figure 6.3 and the results are shown in Figure 6.4. Here it is seen, that even with an imperfection of 45° the parabolic is still better than the catenary and circular arch.

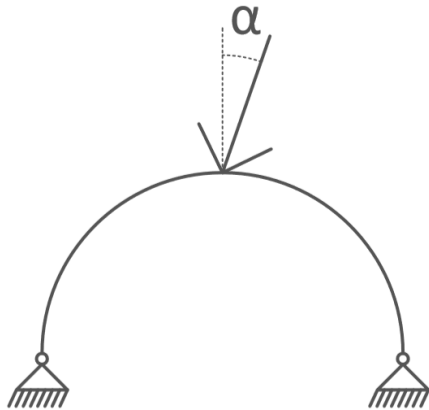


Figure 6.3: Imperfect load orientation for self weight.

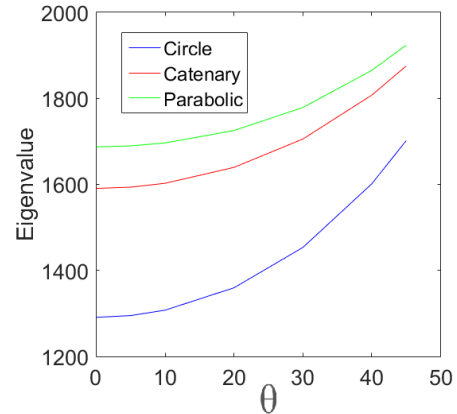


Figure 6.4: Eigenvalue as a function of θ .

If the vertical load remains the same but a horizontal load is applied at the same location as seen in Figure 6.5 then the results are as shown in Figure 6.6 and all results are enclosed on Appendix CD *Arch/Imperfect load*. It is noticed that the eigenvalues are decreasing which is as expected since an additional load is applied. Furthermore, when the horizontal load is slightly less than half of the vertical load then the circular geometry starts to buckle at a higher load than the catenary and parabolic.

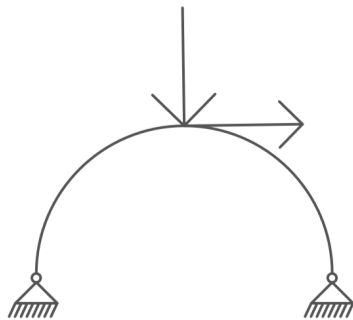


Figure 6.5: Imperfect load orientation for line load.

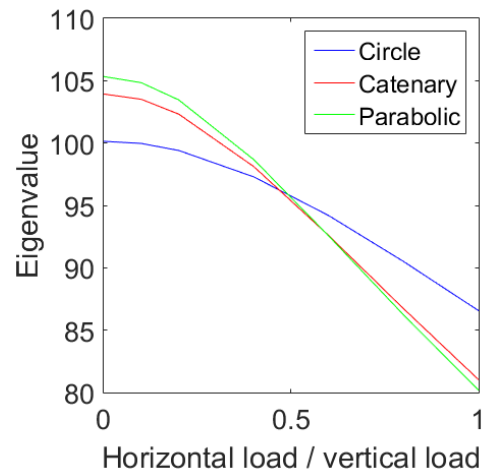


Figure 6.6: Eigenvalue as a function of the horizontal load divided by the vertical load for line load.

If the self weight as well is exposed to a horizontal load as well as seen in Figure 6.7 then the eigenvalue is as seen in Figure 6.8. From the figure it is seen that the eigenvalues decrease for an increasing horizontal load as expected since the total load is higher. Furthermore, it is noticed that the decrease in the eigenvalue for the parabolic and catenary is larger than

for the circular geometry, but in general the parabolic still has the highest eigenvalue.

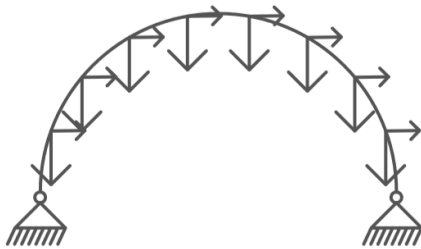


Figure 6.7: Imperfect load orientation for self weight.

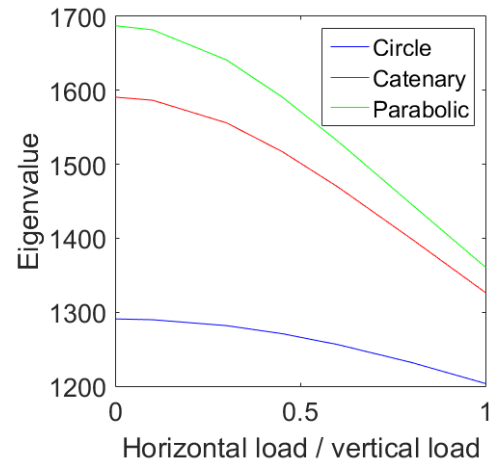


Figure 6.8: Eigenvalue as a function of the horizontal load divided by the vertical load for self weight.

6.2 Changed Thickness

If the thickness of the shell is different from the assumed one then the results are as seen in Figures 6.9 - 6.11. The results are for a simple support in both ends. From the figures it is seen that the required buckling stress increases with increasing thickness which is as expected. Furthermore, the thickness of the shell does not affect the results regarding which cross sectional geometry that buckles first. All results are enclosed on Appendix CD *Arch/Changed thickness*.

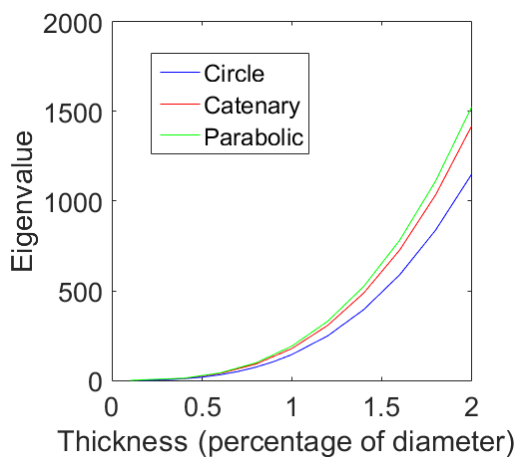


Figure 6.9: Eigenvalue as a function of the thickness for inside suction.

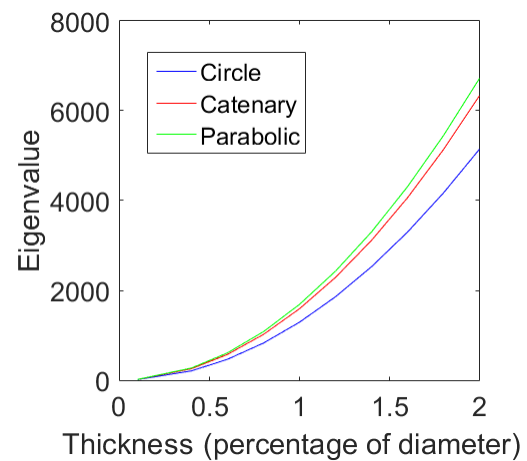


Figure 6.10: Eigenvalue as a function of the thickness for self weight.

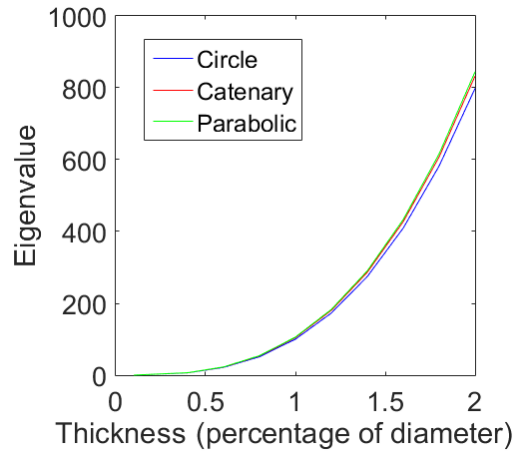


Figure 6.11: Eigenvalue as a function of the thickness for line load.

6.3 Dimple and Perturbation Loads

Another way of implementing imperfections is to investigate the effect from a dimple on the shell structure or multiple perturbation loads (MPLI). This is done in order to get another picture of how some imperfections affect the shell structure.

In order to implement dimples on the shell structure a random area on the surface of the models is chosen and the circumference of that area is constrained and thus when a load is applied in the center of the area it will cause a dimple in the structure. This is illustrated in Figure 6.12 for the model with a catenary cross section. The same is done for the models with a parabolic and circular cross section and the location is for all of the models approximately the same. Due to the different geometries it is not the exact same location.

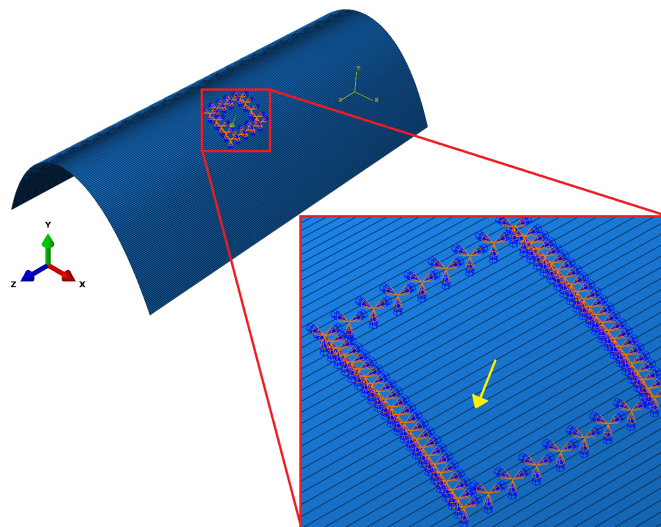


Figure 6.12: Constrained circumference of the area with applied load.

By using the first eigenmode of this model a dimple is obtained as the buckling mode and whether the scaling factor is a positive or negative number the dimple is either an inward or outward dimple. It is expected that an inward dimple and an outward dimple have a different effect on the model thus these are analysed. The location of the dimple is expected to have an effect especially when the model is exposed by a line load since it is expected that when the dimple is on the top of the arch where the line load is acting it influences the results more. Multiple dimples for each model in each load case are analysed and they are numbered 1, 2 and 3 to distinguish them from each other. A scaling factor of ± 0.2 is chosen to implement the dimple which means that the magnitude of the deformation of the dimple is 0.02 m since the thickness is 0.1 m. The initial state for the models with dimples on a catenary cross section are illustrated in Figures 6.13 - 6.16.

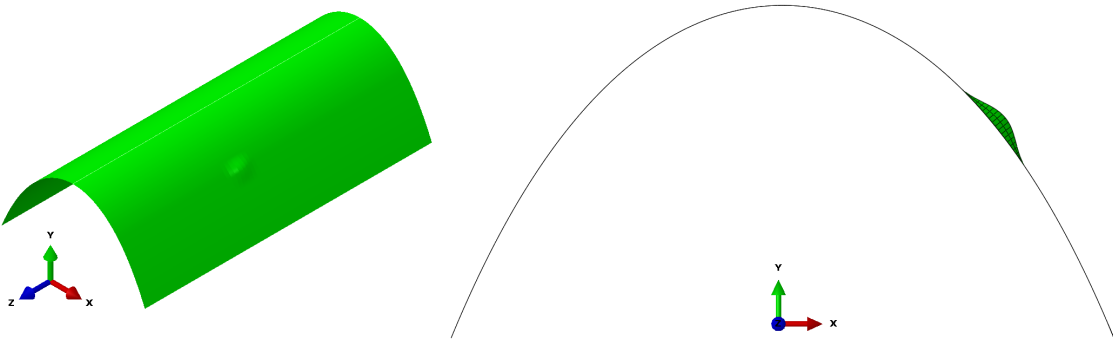


Figure 6.13: Catenary cross section with outward dimple.

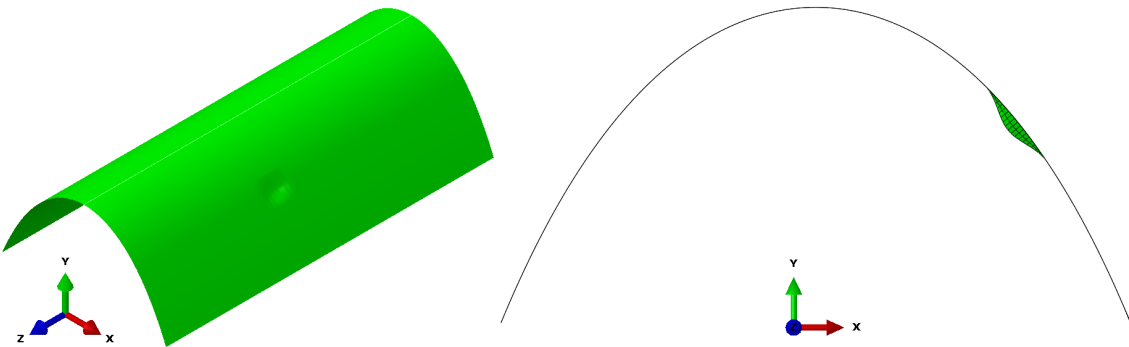


Figure 6.14: Catenary cross section with inward dimple 1.

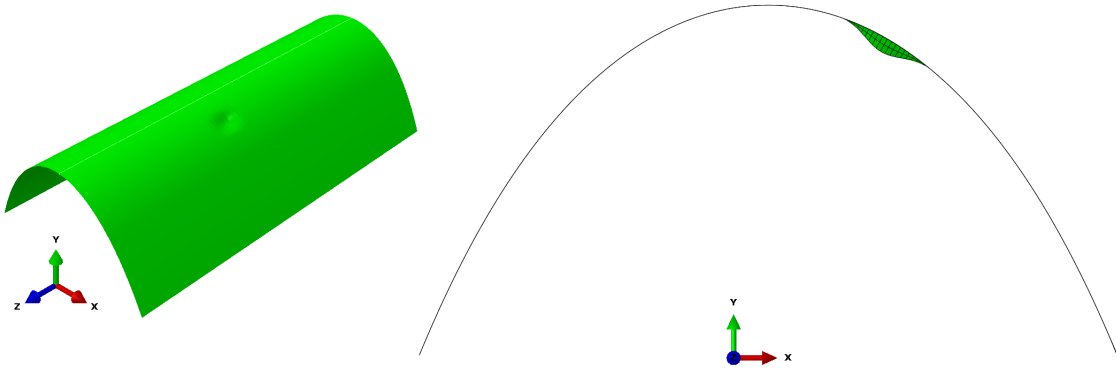


Figure 6.15: Catenary cross section with inward dimple 2.

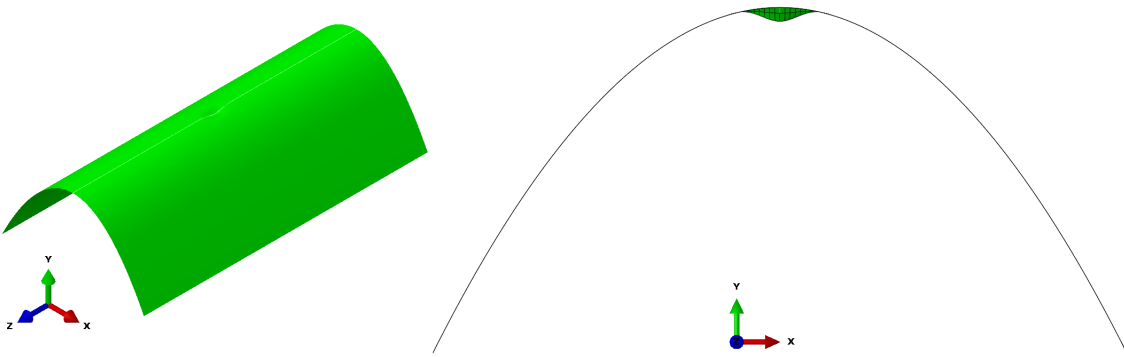


Figure 6.16: Catenary cross section with inward dimple 3.

The imperfection with a dimple is analysed for the different load scenarios i.e. a line load, inside suction and self weight for every model with the different cross sections. For the perturbation loads the imperfection pattern varies dependent on where the perturbation loads are applied and the magnitude of the perturbation loads compared to the different load scenarios. It is chosen to use two perturbation loads which has the same magnitude. The sum of the two loads is equal to the force which is applied to create the dimple and therefore the scaling factor is 0.2 as well. The locations of the perturbation loads are illustrated in Figure 6.17 and the location of the perturbation loads is approximately the same for all of the models.

A specific eigenmode generated from the models with the two perturbation loads is used as the initial state. The chosen eigenmode is the one which represent the most likely deformation caused by the two perturbation loads. For instance, if only one dimple is shown from an eigenmode or if both an inward and outward dimple is shown from an eigenmode these eigenmodes would not be ideal to use as the initial state. The chosen eigenmode to represent the initial state for the model with a catenary cross section is illustrated in Figure 6.18. The initial state for the two other geometries are similar to the

catenary.

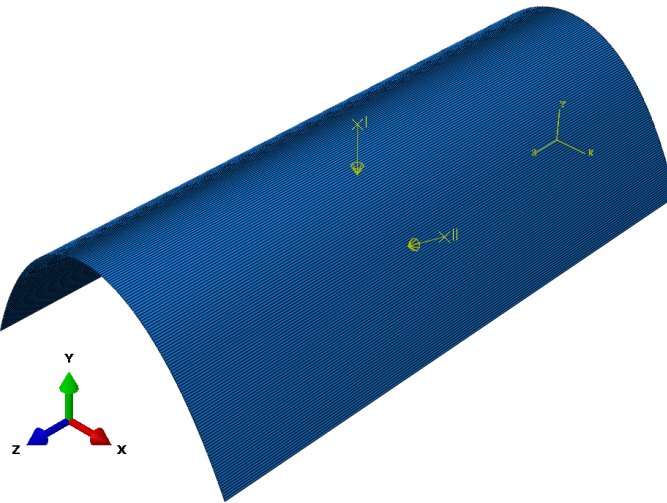


Figure 6.17: Location of the perturbation loads on the catenary cross section.

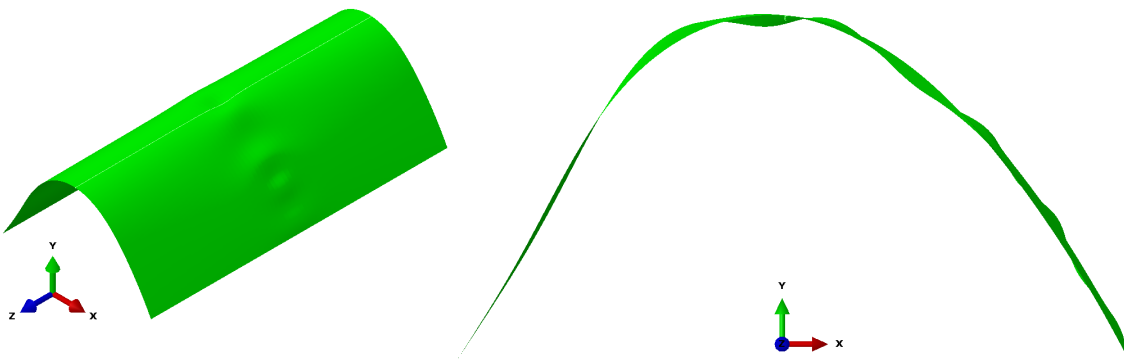


Figure 6.18: MPLI on the surface for the model with a catenary cross section.

The results of the load proportionality factors (LPF) of the critical buckling stress varies from every model with a different cross section, and it varies with every different load scenario. To determine the LPF a plot of the LPF as a function of the displacement at the location of the dimple is made. An example is shown in Figure 6.19 for a circular cross section with inward dimple 2 exposed by self weight. The model buckles when it reaches the peak of the plot and afterwards the LPF drops and the displacement is increasing significantly. The dashed lines represent the point at which buckling occurs and the LPF factor is determined to be 0.966.

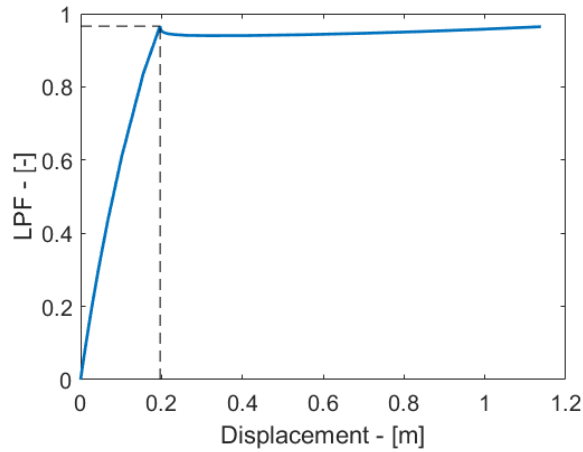


Figure 6.19: Circular cross section with inward dimple 2 exposed by self weight.

The LPF for every model with the different implemented imperfection i.e. inward dimple, outward dimple and MPLI are shown in Table 6.1.

Table 6.1: LPF for the arch with various imperfection types.

Cross section	Load scenarios		
	Suction	Self weight	Line load
Outward dimple			
Circular	0.810	0.921	0.759
Parabolic	1.060	0.999	0.887
Catenary	1.026	0.866	0.785
Inward dimple 1			
Circular	0.755	0.922	0.850
Parabolic	1.000	1.012	0.888
Catenary	1.030	0.904	0.881
Inward dimple 2			
Circular	0.787	0.966	0.860
Parabolic	1.005	1.008	0.787
Catenary	1.020	0.854	0.885
Inward dimple 3			
Circular	0.755	0.839	0.763
Parabolic	1.007	1.020	0.790
Catenary	0.991	1.013	0.584
MPLI			
Circular	0.716	0.605	0.680
Parabolic	0.884	0.843	0.719
Catenary	0.964	0.894	0.691

For the inward and outward dimple the LPF is lower for the model with a circular cross section when exposed to suction which means it buckles before the parabolic and catenary cross section. For the self weight the catenary cross section has the highest LPF when the dimple is on top if the arch, but the lowest in the other scenarios. For a line load on top of the arch the parabolic cross section has the highest LPF compared to the two other geometries when the dimple is on the side. When the dimple gets close to the top, the LPF decreases.

In some cases the value of the LPF exceeds 1.0 which indicates that these specific imperfections are favourable for those cases. This means that a higher load can be applied before buckling occurs. It is seen that when comparing the results for the different location of the inward dimple, the LPF does not change much considering the load cases with self weight and inside suction but when the model is exposed by a line load it has a larger influence which was also expected. The closer the dimple is to the top where the line load is acting the LPF decreases more and more.

By comparing the dimples with the MPLI it is observed that in almost every single case the MPLI is resulting in the lowest LPF. This is because unlike the models with dimples, the MPLI is causing a change of geometry in the entire model and thus the imperfections from the MPLI has a larger area of effect on the model which leads to a lower LPF.

Conclusion

Now the different analysis are performed and all the conclusions are recapitulated in this chapter.

For the circular cylinder it is concluded that different loads acting simultaneously are in some combinations in favour of the buckling stress since it buckles at a higher applied load. Furthermore, some parameters are not important for the study of cylindrical shells. Hereamong, Young's modulus which is just a multiplier on the critical buckling stress. The dimensions are not that important, but the ratio between the dimensions are of great importance. It is also concluded that the equations in EN-3 [2004] take into account global buckling of meridional compression and that the thickness is of great importance for the buckling stress. The results from the numerical software Abaqus is in correlation with the results obtained from the analytical analysis. For the cylindrical shell only forces leading to membrane stresses in the structure are analysed and therefore instability is only due to these membrane forces.

When implementing an imperfection in the geometry for the circular cylinder, the scaling factor relative to the thickness of the imperfection is of great importance. For an increasing scaling factor the buckling stress decreases compared to a perfect geometry. The influence of the imperfections for the different load scenarios varies. When different eigenmodes are used as initial geometry, the critical buckling stress for the different load scenarios varies. For meridional compression the buckling stress decreases when the eigenmode increases which is not the case for the two other load scenarios.

For the shell in shape of an arch it is concluded that the geometry and support types are of great importance for the buckling stress for the different load scenarios. When only considering buckling the optimal geometry does not correspond with the results from a linear static analysis. But when also considering yielding the overall conclusion corresponds well with the expectations, i.e. that the circular geometry is optimal when exposed to inside suction, the catenary geometry is optimal when exposed to self weight when it is fixed supported and the parabolic geometry is optimal when exposed to a line load. In most cases yielding is critical for the arch and therefore yielding as well as buckling should be considered when designing an arch. From the results it is also concluded that in most scenarios the optimal geometry is the one which has the highest collapse load.

If an imperfection is implemented in the load orientation in the self weight and line load, the eigenvalue increases. For an arch with a line load on top the optimal geometry changes when the load orientation is approximately 30° compared to vertical. But for an imperfection in the load orientation less than this the optimal geometry when considering buckling only is not changing. This might be explained by the fact that even though large section moments in the structure are expected to give high stresses in the outermost fibres then when the load orientation is high enough it creates membrane forces which is more critical for buckling for the circular geometry than the parabolic geometry. If a dimple is present in the structure the critical buckling stress decreases in most cases but in some cases the dimple is in favour of the instability. Furthermore, the location of the dimple has a great influence on the results. It is also concluded that when multiple perturbation loads are applied the buckling stress is lower than when a single dimple is present.

Discussion

In this chapter different approaches for the thesis are discussed. These approaches might have influenced the results that are obtained.

For the cylindrical shell different load scenarios could have been examined, e.g. loads that do not give only membrane forces. For imperfections in the cylindrical shell only a geometric non-linear imperfection analysis is performed whereas different kind of imperfections could have been examined as well, such as an imperfection in the load, thickness, Young's modulus etc. As seen for the shell in shape of an arch, the support type is of importance and therefore different supports could be analysed as well to see how those might influence the results. All the results could be verified by experimental data if an experiment was performed.

For the shell in shape of an arch different approaches and analysis could have been done as well. Here among different load cases, different kind of imperfection, other support types and combinations as well as experiments are just a few examples. Furthermore, a study of different geometries could have been performed in order to find the optimal geometry and not only the optimal between the three analysed geometries.

For the numerical analysis a different element type or a finer mesh could have been used. The number of elements in the cross section could also have been increased to make the geometry closer to a perfect circular, parabolic or catenary geometry. Furthermore, a different FEM software than Abaqus could have been used. An analysis of a changed thickness for the different eigenmodes could have been made in order to determine whether the thickness has an influence on the eigenmodes. Furthermore, the eigenmodes from the new models where an eigenmode is implemented as initial geometry could have been analysed in order to see if they gave the same modes as the perfect geometry or if they gave different modes.

Bibliography

S. X.-z. Bashir-Ahmed (2003). *Arc-length technique for nonlinear finite element analysis*. Handbook. Journal of Zhejiang University SCIENCE.

Beverage (2016). *Health and Wellness*. URL: <http://www.beveragedaily.com/>.
Downloadet: 25-05-2016.

B. Bonnerup, et al. (2009). *Stålkonstruktioner efter DS/EN 1993*. No. 1st edition in Handbook. Nyt Teknisk Forlag.

D. Bushnell (1981). *Buckling of shells - pitfall for designers*.

J. N. R. C. M. Wang, C. Y. Wang (2005). *Exact solutions for buckling of structural members*. No. ISBN: 0-8493-2222-7 in Handbook. CRC Press LLC.

M. A. A. R. K. Castro, Rolf Zimmermann (2013). *Thin-Walled Structures*. Handbook. Elsevier Ltd.

Digipraim (2015). *Digipraim*. URL:
<http://digipraim.com/658785-sydney-opera-house-in-sydney-city.html>.
Downloadet: 23-02-2016.

Efunda (2016). *Hollow Circle*. URL:
<http://www.efunda.com/math/areas/CircleHollow.cfm>. Downloadet: 30-03-2016.

EN-2 (2004). *Eurocode 2: Design of concrete structures*. Handbook. European Standards.

EN-3 (2004). *Eurocode 3: Design of steel structures*. Handbook. European Standards.

Frederiksen Scientific (2016). *Trykflaske kulsyre*. URL:
<http://www.frederiksen.eu/shop/product/trykflaske-kulsyre-med-stigroer>.
Downloadet: 25-05-2016.

J. Holst (2005). *Shell buckling*. Handbook. Columbia University.

Hyperphysics (2016). *Moment of Inertia*. URL:
<http://hyperphysics.phy-astr.gsu.edu/hbase/icyl.html>. Downloadet:
30-03-2016.

Jaime Alonso (2014). *Cathedral of Florence*. URL:
<https://jamesjbsociales.wordpress.com/2015/04/19/arte-del-renacimiento/1-1-brunelleschi-cathedral-of-florence/>. Downloadet: 29-02-2016.

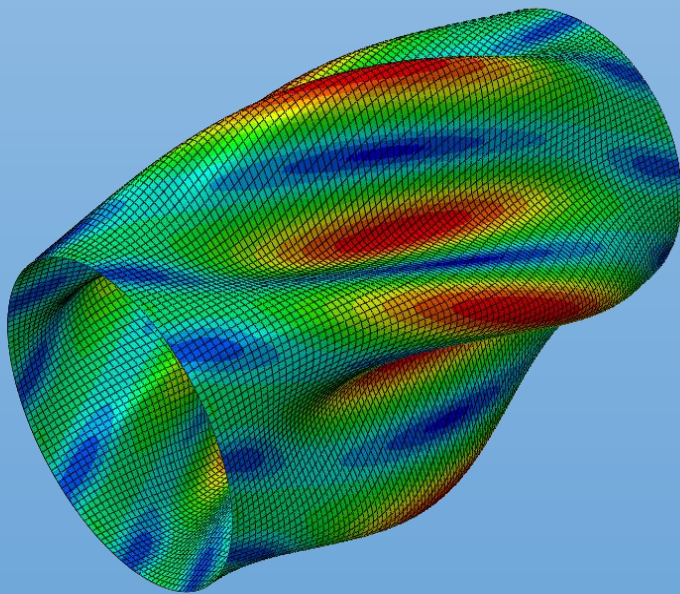
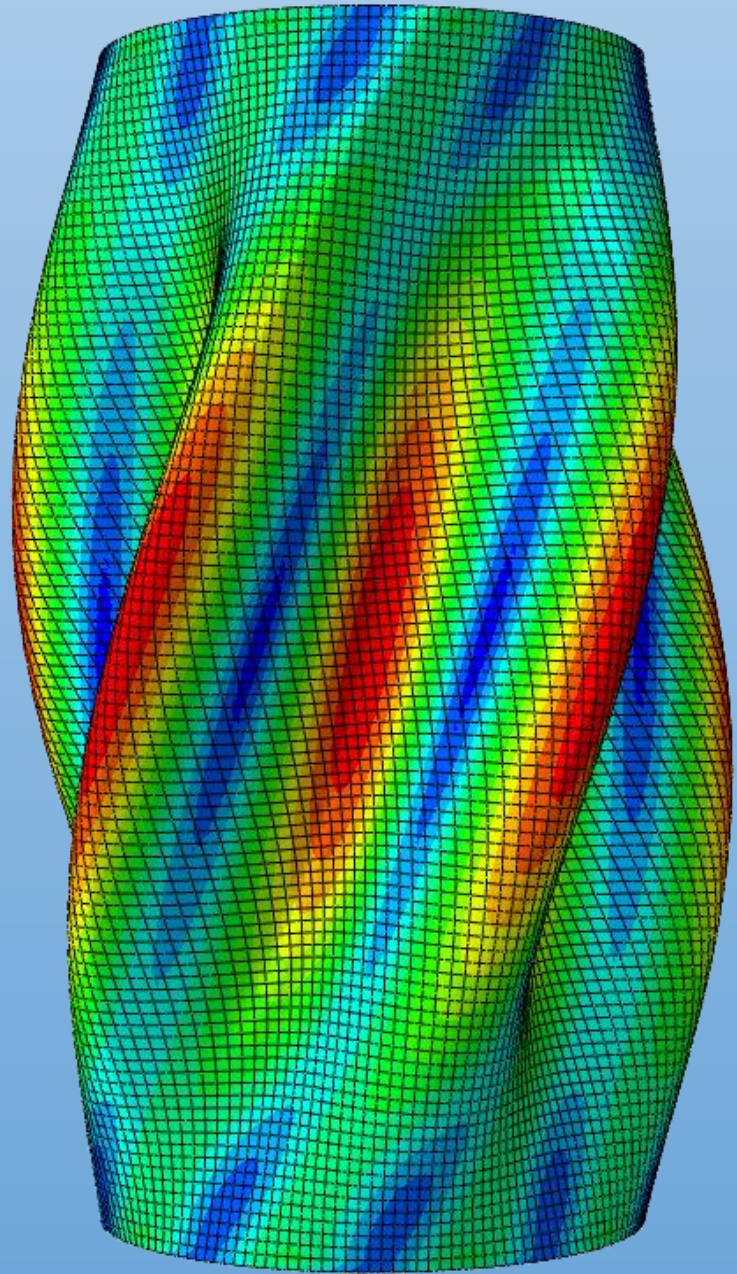
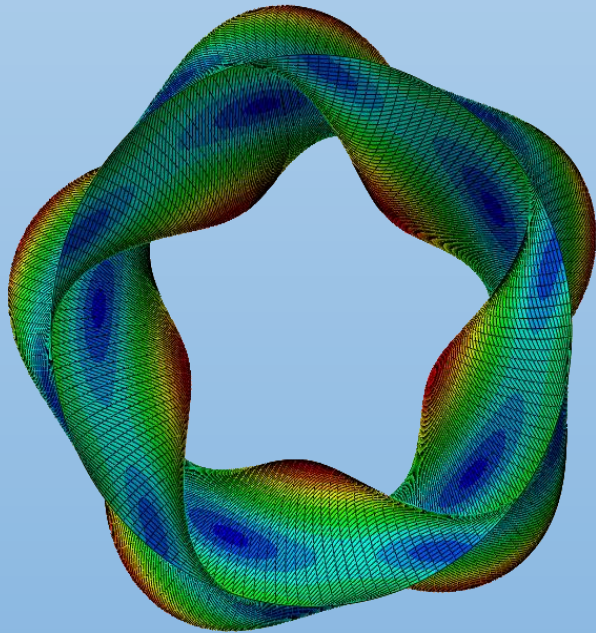
K. A. Seffen (2010). *Surface Texturing Through Cylinder Buckling*. URL:
<http://appliedmechanics.asmedigitalcollection.asme.org/mobile/article.aspx?articleid=1868743>. Downloadet: 14-02-2016.

- Positronic (2016). *WIND ENERGY CONNECTORS AND WIND TURBINES*. URL:
<http://www.connectpositronic.com/wind-energy-connectors/>. Downloadet:
25-05-2016.
- M. E. P. R. J. W. Robert D. Cook, David S. Malkus (2002). *Concepts and applications of finite element analysis*. No. ISBN: 978-0-471-35605-9 in Handbook. John Wiley and Sons Inc.
- Schillerinstitute (2003). *The Long Life of the Catenary*. URL:
http://www.schillerinstitute.org/fid_02-06/031_long_life_catenary.html.
Downloadet: 29-02-2016.
- Schillerinstitute (2013). *The Secret of the Florentine Dome*. URL:
<http://schillerinstitute.org/educ/pedagogy/2013/vereycken-dome-1.html>.
Downloadet: 29-02-2016.
- Simulia (2010). *The solution of nonlinear problems*. URL:
<https://www.sharcnet.ca/Software/Abaqus610/Documentation/docs/v6.10/books/gsk/default.htm?startat=ch08s02.html>. Downloadet: 14-03-2016.
- SteelConstruction (2010). *Steel Construction*. URL:
http://www.steelconstruction.info/Design_of_beams_in_composite_bridges.
Downloadet: 14-02-2016.
- Thebimhub (2016). *Thebimhub*. URL: <https://thebimhub.com/2013/12/30/when-silos-come-tumbling-down/#.VswtppzhChc>.
Downloadet: 23-02-2016.
- UCC (2010). *Buckling of thin walled cylinders*. URL:
<http://publish.ucc.ie/boolean/2010/00/dePaor/11/en>. Downloadet: 14-02-2016.

Buckling of Steel Shell Structures

Master Thesis

Appendix



4th Semester M.Sc. - Structural and Civil Engineering

Kasper Knudsen & Mads Thorup

Aalborg University

08/06-2016

Appendix Overview

Appendix Report

Appendix A - Appendix Overview

Appendix B - Circular Cylinder

Appendix C - Euler Load

Appendix D - Buckling Modes for LBA

Appendix E - Shell in Shape of Arch

Appendix F - Moment Distribution for all Geometries and Loads

Appendix G - Arc Length of Parabolic

Appendix CD

Master Thesis

Circular Cylinder

- Buckling stress
- Changed DL ratio
- Changed DL ratio contour
- Changed E
- Changed E contour
- Changed thickness
- Convergence analysis
- Imperfections

Arch

- Changed thickness
- Convergence analysis
- Failure surface
- Imperfect load
- Points for arc

Appendix **B**

Circular Cylinder

The different boundary conditions for shells are shown in Table B.1.

Table B.1: Boundary conditions for shells [EN-3, 2004].

Boundary condition code	Simple term	Description	Normal displacements	Vertical displacements	Meridional rotation
BC1r	Clamped	radially restrained meridionally restrained rotation restrained	$w = 0$	$u = 0$	$\beta_\phi = 0$
BC1f		radially restrained meridionally restrained rotation free	$w = 0$	$u = 0$	$\beta_\phi \neq 0$
BC2r		radially restrained meridionally free rotation restrained	$w = 0$	$u \neq 0$	$\beta_\phi = 0$
BC2f	Pinned	radially restrained meridionally free rotation free	$w = 0$	$u \neq 0$	$\beta_\phi \neq 0$
BC3	Free edge	radially free meridionally free rotation free	$w \neq 0$	$u \neq 0$	$\beta_\phi \neq 0$

NOTE: The circumferential displacement v is closely linked to the displacement w normal to the surface so separate boundary conditions are not identified in paragraph (3) for these two parameters.

B.1 Circular Cylinder with Meridional Compression

In this section the buckling stress for a circular cylinder exposed to a meridional compression as shown in Figure 3.2 is calculated. The design buckling stress is given by: [EN-3, 2004]

$$\sigma_{x,Rd} = \sigma_{x,Rk} / \gamma_{M1} \quad (B.1)$$

$\sigma_{x,Rd}$	Design buckling stress
$\sigma_{x,Rk}$	Characteristic buckling stress
γ_{M1}	Partial safety factor

The partial safety factor, γ_{M1} , is given as 1.1 cf. EN-3 [2004]. The characteristic buckling stress is given by: [EN-3, 2004]

$$\sigma_{x,Rk} = \chi_x f_{y,k} \quad (B.2)$$

χ_x	Buckling reduction factor
$f_{y,k}$	Characteristic yield stress

The buckling reduction factor is given by: [EN-3, 2004]

$$\chi = \begin{cases} 1 & \text{when } \bar{\lambda} \leq \bar{\lambda}_0 \\ 1 - \beta \left(\frac{\bar{\lambda} - \bar{\lambda}_0}{\bar{\lambda}_p - \bar{\lambda}_0} \right)^\eta & \text{when } \bar{\lambda}_0 < \bar{\lambda} < \bar{\lambda}_p \\ \frac{\alpha}{\bar{\lambda}^2} & \text{when } \bar{\lambda}_p \leq \bar{\lambda} \end{cases} \quad (B.3)$$

α	Elastic imperfection reduction factor
β	Plastic range factor
η	Interaction exponent
$\bar{\lambda}$	Relative slenderness
$\bar{\lambda}_0$	Squash limit relative slenderness
$\bar{\lambda}_p$	Plastic limit relative slenderness

The plastic limit relative slenderness is given by: [EN-3, 2004]

$$\bar{\lambda}_p = \sqrt{\frac{\alpha}{1 - \beta}} \quad (\text{B.4})$$

The values for the meridional squash limit slenderness, $\bar{\lambda}_0$, the plastic range factor, β , and the interaction exponent, η , should be taken as 0.20, 0.60 and 1.0, respectively [EN-3, 2004].

The elastic imperfection reduction factor is given by: [EN-3, 2004]

$$\alpha_x = \frac{0.62}{1 + 1.91(\Delta w_k/t)^{1.44}} \quad (\text{B.5})$$

Δw_k | Characteristic imperfection amplitude

The characteristic imperfection amplitude is given by:

$$\Delta w_k = \frac{1}{Q} \sqrt{\frac{r}{t}} \quad (\text{B.6})$$

Q | Meridional compression fabrication quality parameter

The meridional fabrication quality parameter is depending on the fabrication tolerance quality class and is given in Table B.2. The fabrication tolerance quality class describes the assumed fabrication tolerance requirements for the design and class A is assumed.

Table B.2: Values of fabrication quality parameter Q [EN-3, 2004].

Fabrication tolerance quality class	Description	Q
Class A	Excellent	40
Class B	High	25
Class C	Normal	16

The relative slenderness is given by: [EN-3, 2004]

$$\bar{\lambda} = \sqrt{f_{y,k}/\sigma_{X,Rcr}} \quad (\text{B.7})$$

$\sigma_{X,Rcr}$ | Critical meridional buckling stress

B.1. Circular Cylinder with Meridional Compression

For unstiffened cylindrical shells with a constant thickness the critical meridional buckling stress for boundary conditions BC1 and BC2 at the edges are given by: [EN-3, 2004]

$$\sigma_{X,Rcr} = 0.605EC_X \frac{t}{r} \quad (\text{B.8})$$

E	Young's modulus
C_X	Factor
t	Thickness
r	Radius of cylinder

The factor is depending on the length of the cylinder. The length of the cylinder is characterized by the dimensionless factor, ω , which is given by: [EN-3, 2004]

$$\omega = \frac{l}{t} \sqrt{\frac{r}{t}} = \frac{l}{\sqrt{rt}} \quad (\text{B.9})$$

ω	Dimensionless length factor
l	Length of cylinder

Short cylinders are defined as: [EN-3, 2004]

$$\omega \leq 1.7 \quad (\text{B.10})$$

$$C_X = 1.36 - \frac{1.83}{\omega} + \frac{2.07}{\omega^2} \quad (\text{B.11})$$

Medium-length cylinders are defined as: [EN-3, 2004]

$$1.7 \leq \omega \leq 0.5 \frac{r}{t} \quad (\text{B.12})$$

$$C_X = 1.0 \quad (\text{B.13})$$

Long cylinders are defined as: [EN-3, 2004]

$$\omega > 0.5 \frac{r}{t} \quad (\text{B.14})$$

$$C_X = C_{X,N} \quad (\text{B.15})$$

where

$$C_{X,N} = \max \begin{cases} 1 + \frac{0.2}{C_{Xb}} [1 - 2\omega \frac{t}{r}] \\ 0.6 \end{cases} \quad (\text{B.16})$$

C_{Xb} | Parameter depending on boundary conditions

The parameter, C_{Xb} , is depending on the boundary conditions and is given by Table B.3.

Table B.3: Parameter C_{Xb} for the effect of the boundary conditions on the critical meridional buckling stress in long cylinders [EN-3, 2004].

Case	Cylinder end	Boundary condition	C_{XB}
1	end 1	BC 1	6
	end 2	BC 1	
2	end 1	BC 1	3
	end 2	BC 2	
3	end 1	BC 2	1
	end 2	BC 2	

B.2 Circular Cylinder with Circumferential Compression

In this section the buckling stress for a circular cylinder loaded as shown in Figure 3.4 is calculated.

The design buckling stress, the characteristic buckling stress, the buckling reduction factors and the plastic limit relative slenderness are given by Equations (B.1) - (B.4). The values for the meridional squash limit slenderness, $\bar{\lambda}_0$, the plastic range factor, β , and the interaction exponent, η , should be taken as 0.40, 0.60 and 1.0, respectively [EN-3, 2004]. The elastic imperfection reduction factor, α_θ , is given by Table B.4.

Table B.4: Values of α_θ based on fabrication quality [EN-3, 2004].

Fabrication tolerance quality class	Description	α_θ
Class A	Excellent	0.75
Class B	High	0.65
Class C	Normal	0.50

The relative slenderness is given by: [EN-3, 2004]

$$\bar{\lambda} = \sqrt{f_{y,k}/\sigma_{\theta,Rcr}} \quad (B.17)$$

$\sigma_{\theta,Rcr}$ | Critical circumferential buckling stress

The critical circumferential buckling stress depends on whether the cylinder is short, medium-length or long. Short cylinders are defined as: [EN-3, 2004]

$$\frac{\omega}{C_{\theta}} < 20 \quad (B.18)$$

$$\sigma_{\theta,Rcr} = 0.92E \frac{C_{\theta s} t}{\omega r} \quad (B.19)$$

$C_{\theta s}$ | Factor for short cylinders

The factor, $C_{\theta s}$, depends on the boundary conditions and for the boundary conditions specified in Section 3.1 the factor is given by: [EN-3, 2004]

$$C_{\theta s} = 1.25 + \frac{8}{\omega^2} - \frac{4}{\omega^3} \quad (B.20)$$

Medium-length cylinders are defined as: [EN-3, 2004]

$$20 \leq \frac{\omega}{C_{\theta}} \leq 1.63 \frac{r}{t} \quad (B.21)$$

$$\sigma_{\theta,Rcr} = 0.92E \frac{C_{\theta} t}{\omega r} \quad (B.22)$$

C_{θ} | Factor for medium-length and long cylinders

The factor for medium-length cylinders depends on the boundary conditions and is for the boundaries specified in Section 3.1 equal to 1.25 cf. EN-3 [2004].

Long cylinders are defined as: [EN-3, 2004]

$$\frac{\omega}{C_{\theta}} > 1.63 \frac{r}{t} \quad (B.23)$$

$$\sigma_{\theta,Rcr} = E \left(\frac{t}{r} \right)^2 \left[0.275 + 2.03 \left(\frac{C_{\theta} r}{\omega t} \right)^4 \right] \quad (B.24)$$

B.3 Circular Cylinder with Shear Stress

In this section the buckling stress for a circular cylinder exposed to a load as shown in Figure 3.5 is calculated.

The design buckling stress, the characteristic buckling stress, the buckling reduction factors and the plastic limit relative slenderness for this load scenario are given by Equations (B.1) - (B.4).

The values for the meridional squash limit slenderness, $\bar{\lambda}_0$, the plastic range factor, β , and the interaction exponent, η , should be taken as 0.40, 0.60 and 1.0, respectively [EN-3, 2004]. The elastic imperfection reduction factor is given by Table B.4.

The relative slenderness is given by: [EN-3, 2004]

$$\bar{\lambda} = \sqrt{(f_{y,k}/\sqrt{3})/\tau_{x\theta,Rcr}} \quad (B.25)$$

$\tau_{x\theta,Rcr}$ | Critical shear buckling stress

The critical shear buckling stress is given by: [EN-3, 2004]

$$\tau_{x\theta,Rcr} = 0.75EC_\tau \sqrt{\frac{1}{\omega} \frac{t}{r}} \quad (B.26)$$

The factor for shear stress depends on whether the cylinder is short, medium length or long. For short cylinders it is defined as: [EN-3, 2004]

$$\omega < 10 \quad (B.27)$$

$$C_\tau = \sqrt{1 + \frac{42}{\omega^3}} \quad (B.28)$$

Medium-length cylinders are defined as: [EN-3, 2004]

$$10 \leq \omega \leq 8.7 \frac{r}{t} \quad (B.29)$$

$$C_\tau = 1.0 \quad (B.30)$$

Long cylinders are defined as: [EN-3, 2004]

$$\omega > 8.7 \frac{r}{t} \quad (B.31)$$

$$C_\tau = \frac{1}{3} \sqrt{\omega \frac{t}{r}} \quad (B.32)$$

B.4 Circular Cylinder with Combined Loads

In the case where more than one load are acting on the cylinder the stresses should satisfy the following stress criteria: [EN-3, 2004]

$$\left(\frac{\sigma_{x,Ed}}{\sigma_{x,Rd}}\right)^{k_x} + \left(\frac{\sigma_{\theta,Ed}}{\sigma_{\theta,Rd}}\right)^{k_\theta} - k_i \left(\frac{\sigma_{x,Ed}}{\sigma_{x,Rd}}\right) \left(\frac{\sigma_{\theta,Ed}}{\sigma_{\theta,Rd}}\right) + \left(\frac{\tau_{x\theta,Ed}}{\tau_{x\theta,Rd}}\right)^{k_\tau} \leq 1 \quad (\text{B.33})$$

$\sigma_{x,Ed}$	Significant value of meridional compressive membrane stress
$\sigma_{\theta,Ed}$	
$\tau_{x\theta,Ed}$	
$k_x, k_\theta, k_i, k_\tau$	
	Buckling interaction parameters

The buckling interaction parameters are given by: [EN-3, 2004]

$$k_x = 1.25 + 0.75\chi_x \quad (\text{B.34})$$

$$k_\theta = 1.25 + 0.75\chi_\theta \quad (\text{B.35})$$

$$k_\tau = 1.75 + 0.25\chi_\tau \quad (\text{B.36})$$

$$k_i = (\chi_\theta\chi_\tau)^2 \quad (\text{B.37})$$

Euler Load

In this chapter the appendices for the Euler load are shown.

C.1 Analytical

In this section the Euler load is calculated for a column with the same cross sections as the circular cylinder in Chapter 3. The column is simple supported in the top and fixed in the bottom as shown in Figure C.1 and the overall geometri is shown in Figure C.2.

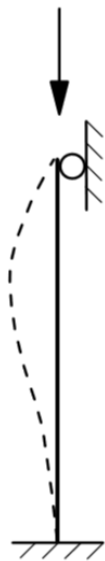


Figure C.1: Simple supported column. EN-2 [2004]

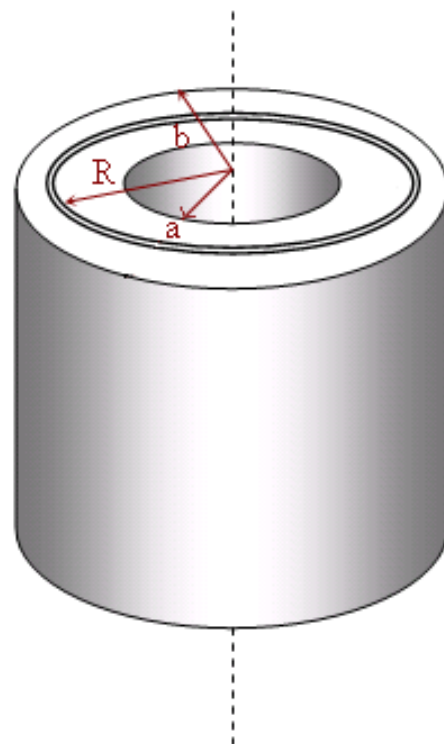


Figure C.2: Hollow cylinder. [Hyperphysics, 2016]

The Euler load is given by: [Bonnerup et al., 2009]

$$N_{cr} = \frac{\pi^2 EI}{l_s^2} \quad (C.1)$$

N_{cr}	Euler load
E	Elasticity modulus, 210 000 MPa
I	Moment of inertia
l_s	Theoretical column length

For a column that is supported as shown in Figure C.1 the theoretical column length is 0.7 times the physical column length. The length of the cylinder is taken as the length of the cylinder where the buckling stress becomes constant for increasing length. This happens at a length that is 12.18 times the diameter which corresponds to 1.218 m cf. Section 3.6.1. The moment of inertia for a hollow cylinder is given by: [Efunda, 2016]

$$I = \frac{\pi(b^4 - a^4)}{2} \quad (C.2)$$

I	Moment of inertia
b	Outer radius of cylinder, 0.0505 m
a	Inner radius of cylinder, 0.0495 m

Insertion of the outer and inner radius gives:

$$I = \frac{\pi \left((0.0505 \text{ m})^4 - (0.0495 \text{ m})^4 \right)}{2} = 7.85 \cdot 10^{-7} \text{ m}^4$$

$$N_{cr} = \frac{\pi^2 \cdot 2.1 \cdot 10^{11} \text{ N/m}^2 \cdot 7.85 \cdot 10^{-7} \text{ m}^4}{(0.7 \cdot 1.218 \text{ m})^2} = 712\,871.2 \text{ N}$$

To convert the load into a stress the load is divided by the end area of the cylinder. The end area of the cylinder is given by: [Efunda, 2016]

$$A = \pi(b^2 - a^2) = \pi \cdot \left((0.0505 \text{ m})^2 - (0.0495 \text{ m})^2 \right) = 3.14159 \cdot 10^{-4} \text{ m}^2 \quad (C.3)$$

which gives the following stress:

$$\sigma_{cr} = \frac{N_{cr}}{A} = \frac{712\,871.2 \text{ N}}{3.14159 \cdot 10^{-4} \text{ m}^2} = 2.27 \cdot 10^9 \text{ N/m}^2 = 2269.1 \text{ MPa} \quad (C.4)$$

From Chapter 3 the constant buckling stress is given by:

$$\frac{\sigma}{E} = 0.00726 \quad \Rightarrow \quad \sigma = 0.00726E \quad (\text{C.5})$$

Insertion of Young's modulus gives:

$$\sigma = 0.00726 \cdot 2.1 \cdot 10^{11} \text{ N/m}^2 = 1.5246 \cdot 10^9 \text{ N/m}^2 = 1524.6 \text{ MPa}$$

In order for the stresses from EN-3 [2004] and the Euler load to be the same the theoretical column length should correspond to 0.854 times the physical column length which corresponds to something in between a simple and a fixed support at the bottom.

C.2 Finite Element Method

In this section the results of a model in Abaqus is shown. In Figure C.3 the first eigenmode of a 1.8 m long cylinder is shown and in Figure C.4 the third eigenmode for a 1.6 m long cylinder is shown. From the figures it is seen that the buckling mode corresponds to the shown buckling of a column in Figure C.1 which is as expected.

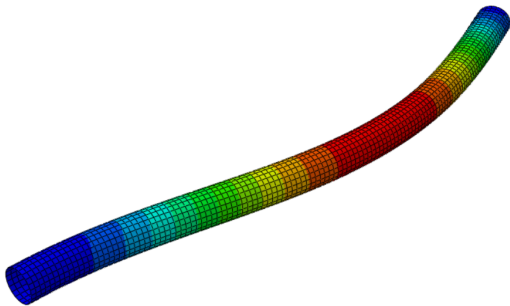


Figure C.3: First eigenmode of a 1.8 m long cylinder.

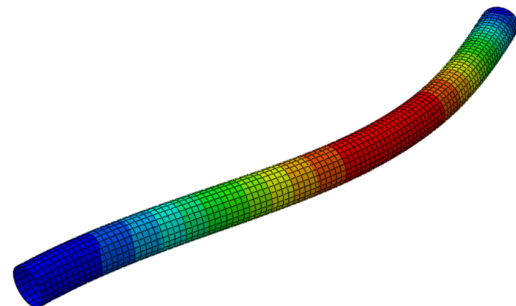


Figure C.4: Third eigenmode of a 1.6 m long cylinder.

From the results it is concluded that the longer the cylinder is the more likely it is to buckle due to global buckling corresponding to a Euler load on a column. Furthermore, the length of the cylinder does not correspond exactly to the calculated length in the analytical approach but is in the same order of magnitude. This is yet another way to see that EN-3 [2004] takes in some safety.

Buckling Modes for LBA

The dimensions of the cylindrical shell structure are given by:

- Length = 200 mm
- Radius = 50 mm
- Thickness = 1 mm

D.1 Buckling Modes for Meridional Compression.

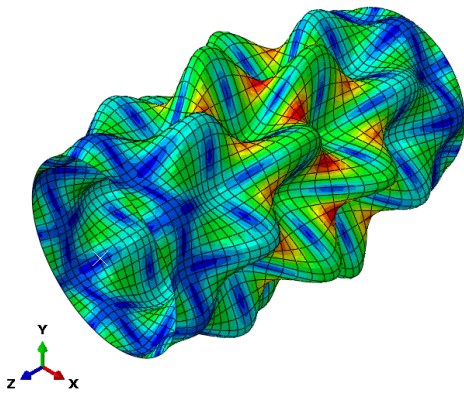


Figure D.1: Buckling mode 1 for meridional compression. $\lambda_1 = 2466.5$.

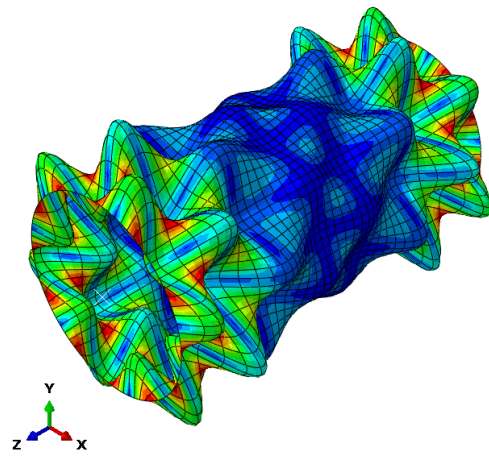


Figure D.2: Buckling mode 5 for meridional compression. $\lambda_5 = 2495.1$.

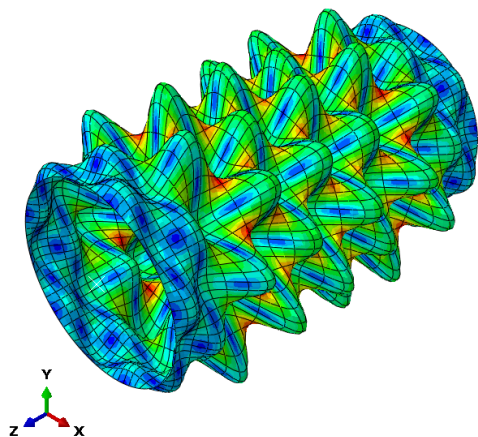


Figure D.3: Buckling mode 13 for meridional compression. $\lambda_{13} = 2514.1$.

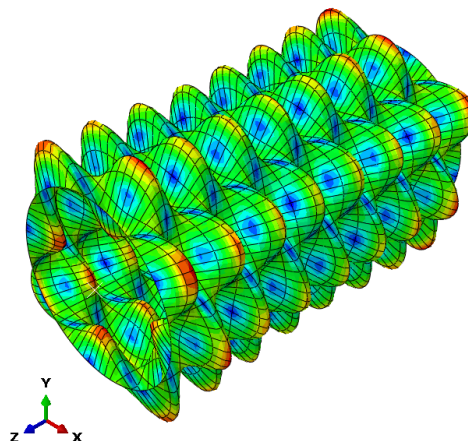


Figure D.4: Buckling mode 25 for meridional compression. $\lambda_{25} = 2530.8$.

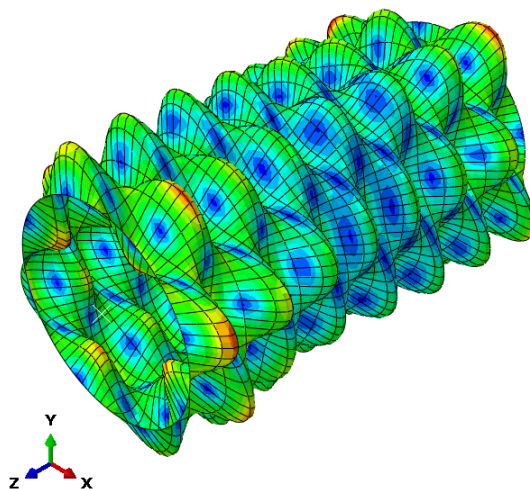


Figure D.5: Buckling mode 29 for meridional compression. $\lambda_{29} = 2534.6$.

D.2 Buckling Modes for Circumferential Compression.

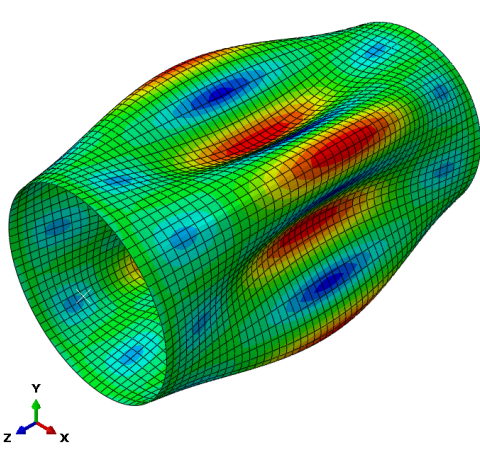


Figure D.6: Buckling mode 1 for circumferential compression. $\lambda_1 = 3.47$.

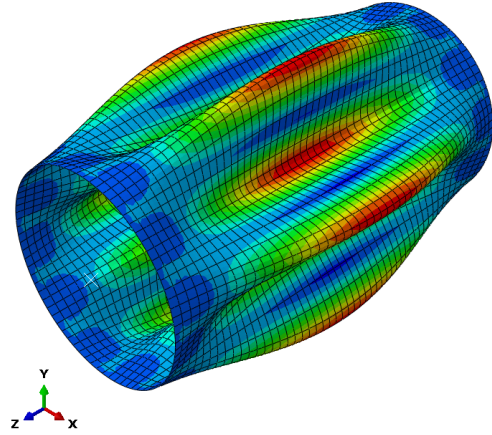


Figure D.7: Buckling mode 5 for circumferential compression. $\lambda_5 = 5.01$.

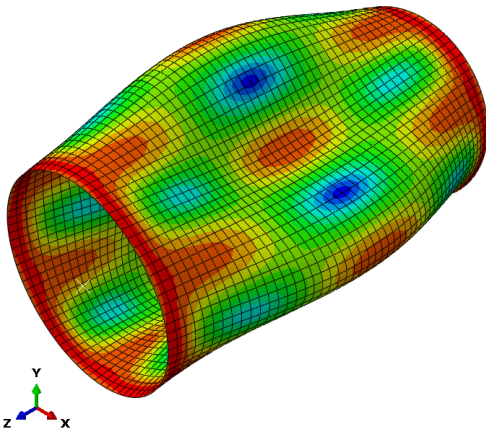


Figure D.8: Buckling mode 13 for circumferential compression. $\lambda_{13} = 7.23$

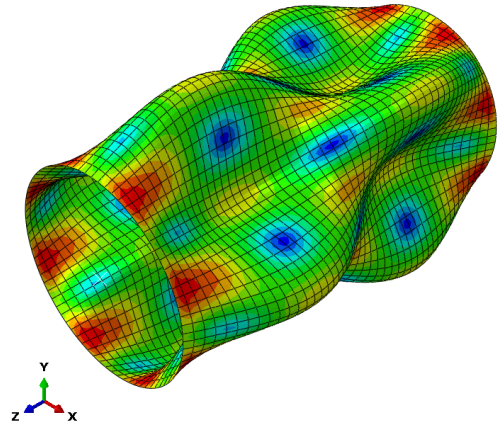


Figure D.9: Buckling mode 25 for circumferential compression. $\lambda_{25} = 9.74$.

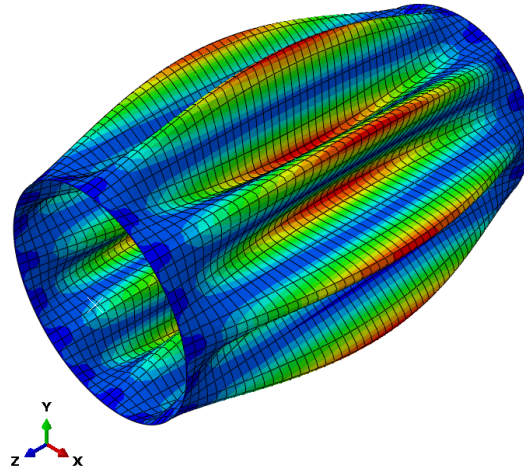


Figure D.10: Buckling mode 29 for circumferential compression. $\lambda_{29} = 10.88$.

D.3 Buckling Modes for Shear Stress.

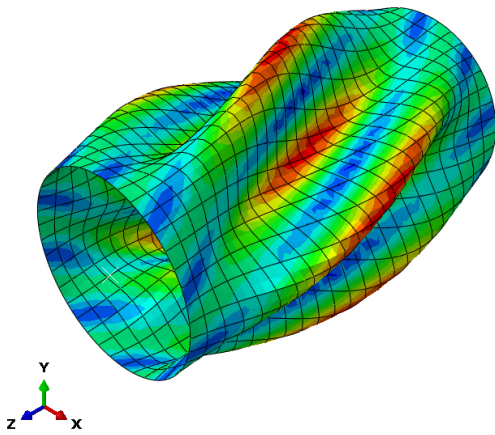


Figure D.11: Buckling mode 1 for shear stress. $\lambda_1 = 614.80$.

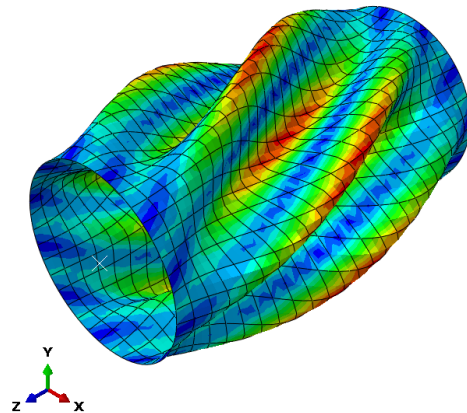


Figure D.12: Buckling mode 5 for shear stress. $\lambda_5 = -664.68$.

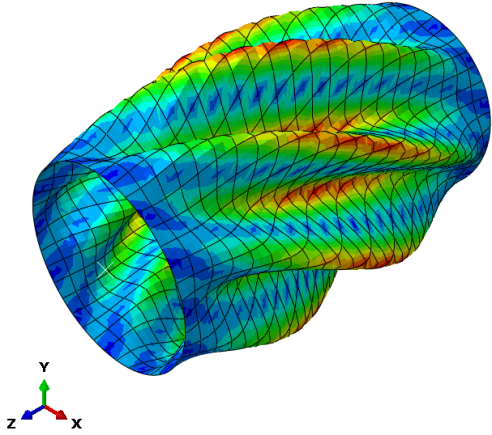


Figure D.13: Buckling mode 13 for shear stress. $\lambda_{13} = 773.92$

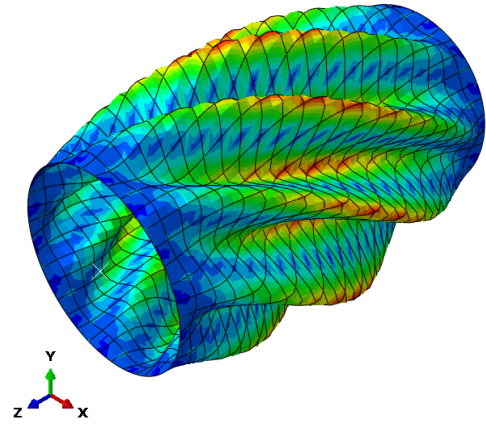


Figure D.14: Buckling mode 25 for shear stress. $\lambda_{25} = 921.79$.

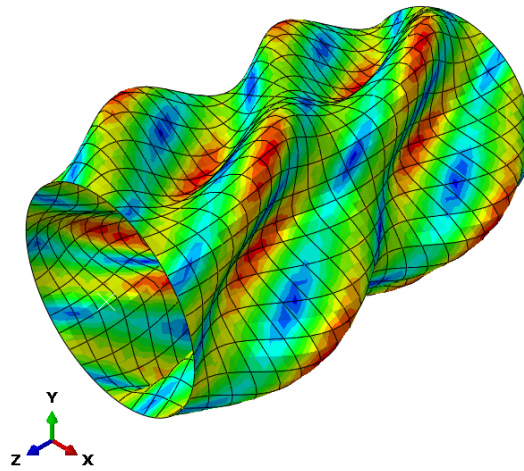


Figure D.15: Buckling mode 29 for shear stress. $\lambda_{29} = 1020.6$.

Arch Structure

E.1 Convergence Analysis - Buckling

A convergence analysis for the circular cross section with all the load scenarios is performed for the buckling analysis and the results are shown in Figures E.1 - E.4. All results are enclosed on Appendix CD *Arch/Convergence analysis*.

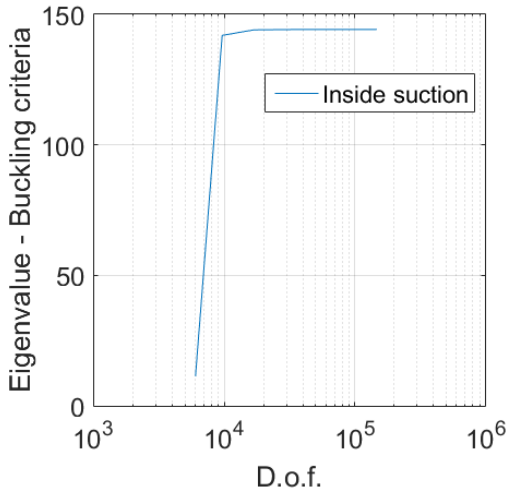


Figure E.1: Convergence analysis for circular cross section with inside pressure for buckling.

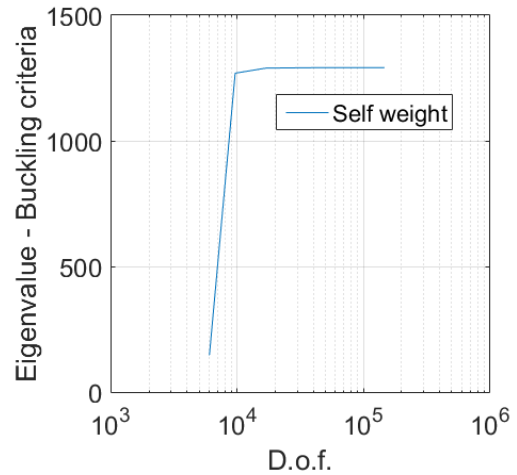


Figure E.2: Convergence analysis for circular cross section with self weight for buckling.

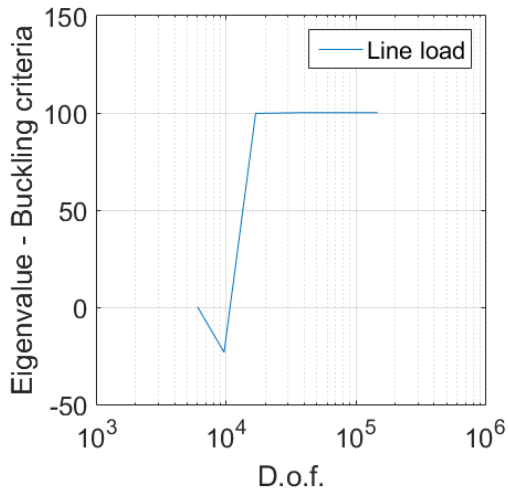


Figure E.3: Convergence analysis for circular cross section with load on top of the arch for buckling.

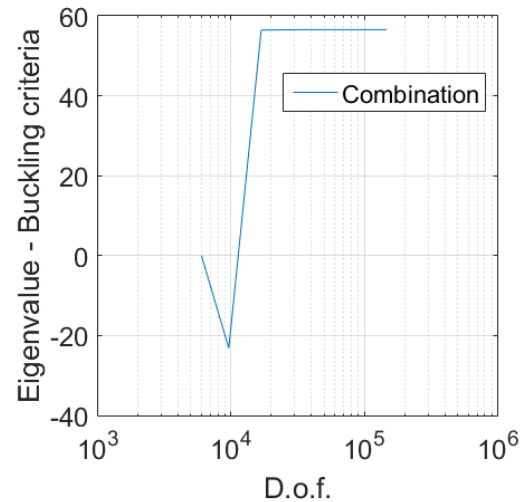


Figure E.4: Convergence analysis for circular cross section with a combination of all loads for buckling.

From the figures it is seen that all the diagrams converges with a number of d.o.f. of 16 854. In order to ensure that all other cross sections are fully converged a number of 38 550 d.o.f. for all the models are chosen. This gives a mesh created with 804 elements. This requires a more computational effort in the software but since the difference in the calculation time is minimal it is acceptable.

E.2 Convergence Analysis - Linear Static Analysis

A convergence analysis for the circular cross section with all the load scenarios is performed as a linear static analysis and the results are shown in Figures E.5 - E.8. All results are enclosed on Appendix CD *Arch/Convergence analysis*.

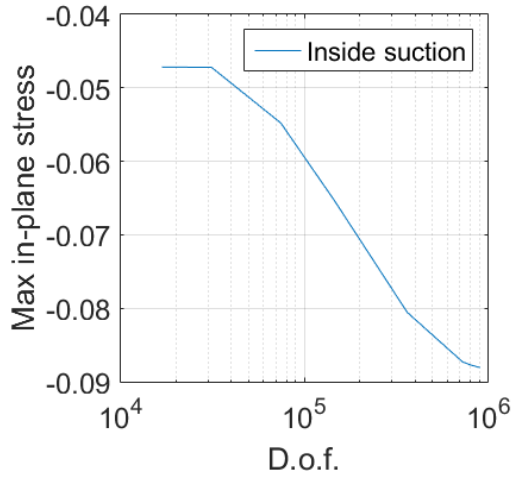


Figure E.5: Convergence analysis for circular cross section with inside pressure for a linear static analysis.

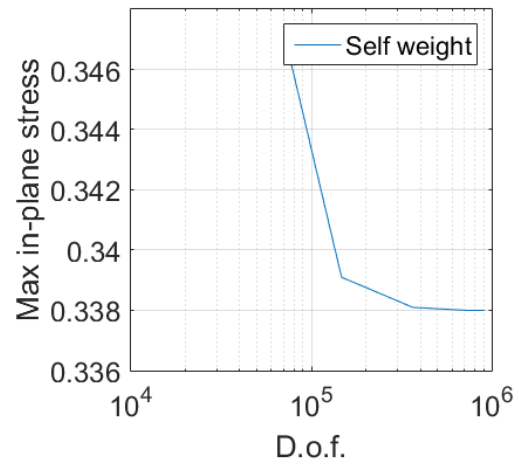


Figure E.6: Convergence analysis for circular cross section with self weight for a linear static analysis.

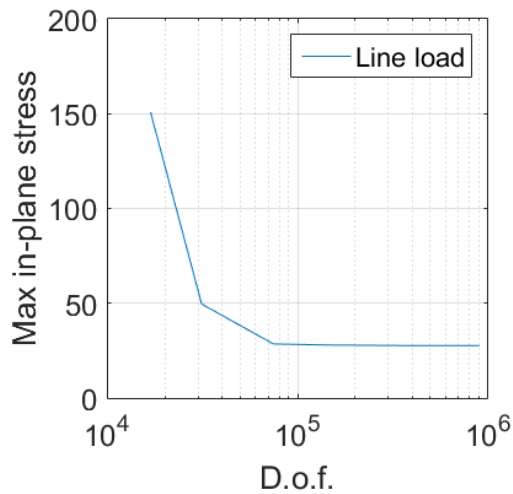


Figure E.7: Convergence analysis for circular cross section with load on top of the arch for a linear static analysis.

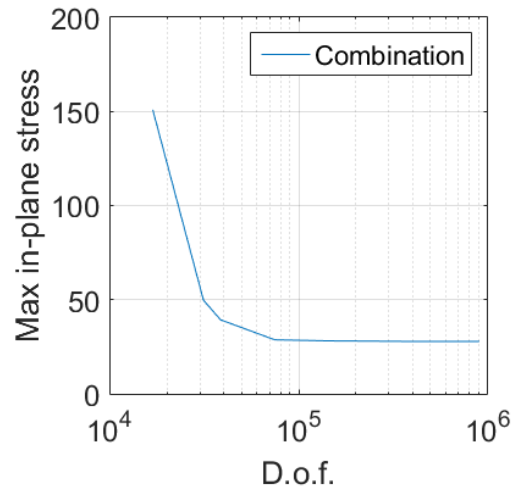


Figure E.8: Convergence analysis for circular cross section with a combination of all loads for a linear static analysis.

It is concluded that for the linear static analysis a higher number of d.o.f. is required before the results are converged. Some of the load scenarios converges at 74 646 d.o.f. while others converge at 724 806 d.o.f. In order to ensure that all the models and load scenarios are fully converged for the linear static analysis model, a d.o.f. of 724 806 is chosen for all the models.

Moment Distribution for all Geometries and Loads

All moment distributions for all three cross sectional geometries and all three different load cases are shown in Figure F.1. Below each distribution a text is written where the following is used:

- cir = circular cross section
- par = parabolic cross section
- cat = catenary cross section
- Pres = inside suction load
- LL = line load
- DL = self weight
- M1 = moment around 1st local axis
- M2 = moment around 2nd local axis
- rol = model with roller support in one end

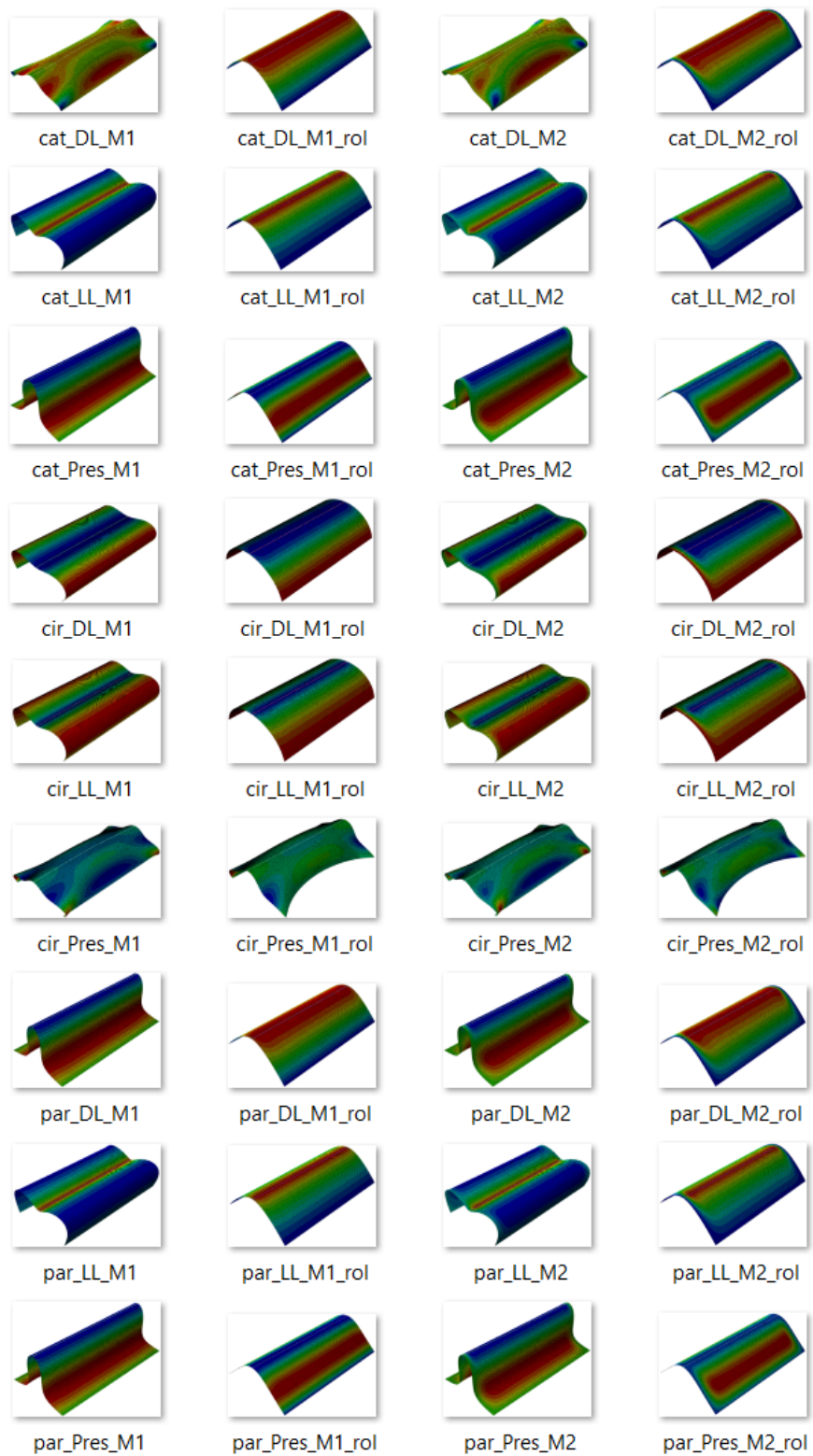


Figure F.1: Moment distribution for all geometries and loads.

Arc Length of Parabolic

In this chapter the formulas and method for analytically determining the same length of the arc for the parabolic is shown. The general equation for a parabolic is:

$$y = f(x) = ax^2 + bx + c \quad (\text{G.1})$$

If Equation (G.1) is differentiated it yields:

$$\frac{dy}{dx} = f'(x) = 2ax + b \quad (\text{G.2})$$

The incremental arc length is given by the use of Pythagoras:

$$ds = \sqrt{dx^2 + dy^2} = \sqrt{1 + (dy/dx)^2}dx \quad (\text{G.3})$$

Insertion of Equation (G.2) into Equation (G.3) yields:

$$ds = \sqrt{1 + (2ax + b)^2}dx = \sqrt{4a^2x^2 + 4abx + b^2 + 1}dx \quad (\text{G.4})$$

The arc length is then given by integration between the two points on the arc:

$$\Delta L = \int_{S_1}^{S_2} ds \quad (\text{G.5})$$

In the (x,y)-coordinate system it is written by:

$$\begin{aligned} \Delta L &= \int_{x_1}^{x_2} \sqrt{4a^2x^2 + 4abx + b^2 + 1}dx \\ &= \left[\frac{8a^2x + 4ab}{16a^2} \sqrt{4a^2x^2 + 4abx + b^2 + 1} \right]_{x_1}^{x_2} \\ &\quad + \left[\frac{16a^2(b^2 + 1)^2}{32a^2} \frac{1}{2a} \log \left(8a^2x + 4ab + 4a\sqrt{4a^2x^2 + 4abx + b^2 + 1} \right) \right]_{x_1}^{x_2} \end{aligned} \quad (\text{G.6})$$

From Equation (5.2) which describes the chosen parabolic it is noticed that:

$$\begin{aligned} a &= -1/5 \\ b &= 0 \\ c &= 5 \end{aligned} \tag{G.7}$$

The total arc length is given by insertion of the parameters into Equation (G.6):

$$\begin{aligned} L_{\text{Parabolic}} &= \left[\frac{8 \cdot (-1/5)^2 \cdot x}{16 \cdot (-1/5)^2} \sqrt{4 \cdot (-1/5)^2 \cdot x^2 + 1} \right]_{-5}^5 \\ &+ \left[\frac{16 \cdot (-1/5)^2 \cdot (1)^2}{32 \cdot (-1/5)^2} \frac{1}{2 \cdot (-1/5)} \log \left(8 \cdot (-1/5)^2 \cdot x + 4 \cdot (-1/5) \cdot \sqrt{4 \cdot (-1/5)^2 \cdot x^2 + 1} \right) \right]_{-5}^5 \\ &= \underline{14.79} \end{aligned} \tag{G.8}$$

In order to verify that the results are correct the length of a circle and a straight line are found as well. For a straight line the length is given by (c.f Figure G.1):

$$L_{\text{Line}} = 2 \left(\sqrt{x^2 + y^2} \right) = 2 \cdot \left(\sqrt{5^2 + 5^2} \right) = \underline{14.14} \tag{G.9}$$

For a circle the length is given by (c.f Figure G.1):

$$L_{\text{Circle}} = \frac{2r\pi}{2} = \frac{2 \cdot 5\pi}{2} = \underline{15.71} \tag{G.10}$$

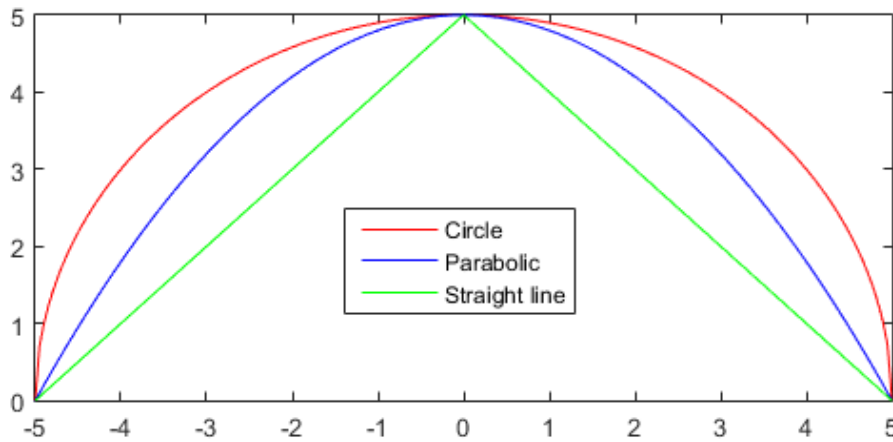


Figure G.1: Plot of circle, parabolic and straight line.

From Figure G.1 it is seen that the obtained results corresponds with what is expected since the length of a straight line should be less than the parabolic which should be less than the circle.